NOTICE

The quality of this microform is heavily dependent upon the quality of the original thesis submitted for microfilming. Every effort has been made to ensure the highest quality of reproduction possible

If pages are missing, contact the university which granted the degree.

Some pages may have indistinct print especially if the original pages were typed with a poor typewriter ribbon or if the university sent us an inferior photocopy.

Reproduction in full or in part of this microform is governed by the Canadian Copyright Act, R.S.C. 1970, c. C-30, and subsequent amendments.

AVIS

La qualité de cette microforme dépend grandement de la qualité de la thèse soumise au microfilmage Nous avons tout fait pour assurer une qualité supérieure de reproduction.

S'il manque des pages, veuillez communiquer avec l'université qui a conféré le grade

La qualité d'impression de certaines pages peut laisser à désirer, surtout si les pages originales ont été dactylographiées à l'aide d'un ruban usé ou si l'université nous a fait parvenir une photocopie de qualité inférieure

La reproduction, même partielle, de cette microforme est soumise à la Loi canadienne sur le droit d'auteur, SRC 1970, c. C-30, et ses amendements subséquents

Evaluation of a Class of Creeping Wave Formulations with Applications to Practical Modeling of Aircraft Antenna EMI Coupling Problems

Debobroto Chatterjee

A Thesis
in
The Department
of
Electrical and Computer Engineering

Presented in Partial Fulfilment of the Requirements
for the Degree of Master of Applied Science at
Concordia University
Montréal, Québec, Canada

March, 1992

ISBN 0-315-73637-2

ABSTRACT

Evaluation of a Class of Creeping Wave Formulations with Applications to Practical Modeling of Aircraft Antenna EMI Coupling Problems

Debobroto Chatterjee

Computation of coupling gain between antennas near a cylinder via the UTD *scattering* and *coupling* formulations have been performed for both on and off surface cases. The NECBSC2 code has been employed to replicate some of the previously published data of Harris by keeping the sources at h= 0.0375 m for a cylinder of radius 24". Additional comparisons between NECBSC2, AAPG codes, UTD coupling formulation, and available measured data, have shown that the previous conclusions of Harris - regarding the inadequacies of the AAPG code are incorrect. For on-surface locations, the present AAPG code predicts higher coupling levels when the Fock parameter $\xi > 15.0$. The present AAPG code has also been shown to predict more coupling whenever antennas are off the surface - compared to the NECBSC2 code. The NECBSC2 code, or the UTD scattering formulation, is inaccurate near the cylinder vicinity, and, hence cannot model on-surface coupling. The overlap height between the two UTD formulations has been determined in an empirical fashion for ka= 10 and 102. Similar empirical relations for other values of ka has also been found as a function of kh for $Z_{offset} = 0"$. These relations can be used as a 'rule-of-thumb' criterion in determining which formulation to use at a given height for practical modeling applications.

Contents

List of Figures

List of major symbols used in the thesis

k,λ: wavenumber and wavelength

a,ϕ: cylinder radius and azimuthal angle

Z_{offset}: axial separation along cylinder long axis

$\hat{\mathbf{n}}, \hat{\mathbf{b}}, \hat{\mathbf{t}}$: normal, binormal and tangent unit vectors

t: geodesic path length

ξ: Fock parameter evaluted over the geodesic path t.

$U_0(\xi)$: soft surface Fock function

$V_0(\xi)$: hard surface Fock function

θ_g: geodesic angle between Q_1 and Q_2 in Fig. 3.3

$y_{s,r}$: effective antenna heights for source and receiver above the cylinder.

m: transition quantity at a point Q on the geodesic path

$G_{t,r}$: transmit and receive antenna gains along the propagation path

C_{iso}: isotropic coupling gain

$F_h(\xi, y_s, y_r)$: Taylor series form of the hard Fock integral

Chapter 1

Introduction

Computation of coupling gain between sources on a cylinder serve as a good model in obtaining numerical estimates for fuselage-mounted antennas used in sophisticated avionic systems. This knowledge provides one with an understanding of the EMI (ElectroMagnetic Interference) level between such antennas and their associated r.f systems. The situation can be seen in Fig. 1.1. In that figure, the antennas S and R are located on the wing and are shadowed by the fuselage. In the same figure, the two positions S' and R', refer to those locations when the same antennas are mounted on the fuselage. In still another situation, (not shown in Fig. 1.1), one antenna is located on the fuselage, while, the other is mounted on the wing. In all the three categories, coupling between the antennas is determined by the location of the antennas with respect to the fuselage. The fuselage shape and structure plays a major role in determining coupling, as, the antennas are completely blocked by the fuselage. Moreover, the aircraft fuselage is made out of such material, that, it

is impenetrable to electromagnetic waves.

The above physical situation suggests that a possible mode of coupling between antennas at S,S′ and R,R′ is due to electromagnetic field that can 'go around' or 'creep around' the fuselage. This possible mode of coupling is known as '*creeping wave*' coupling and the magnitude depends strongly on the fuselage shape. The possible coupling paths are shown in Figs. 1.1 and 1.2. Fig. 1.2 is a cross-sectional view of the general problem shown in Fig. 1.1.

It is important for the designer of complex systems to have a quantitative idea of the EMI level before the actual design is implemented. Thus, it is necessary to have stored as much information about the several coupling paths that can occur between a pair of antenna locations in presence of a complex body like an aircraft. In the state-of-art EMI prediction techniques, computer aided analysis is extensively performed to obtain quantitative estimates in such situations. The computer codes, or, equivalently EMC analysis programs, are thus helpful tools for the designer in careful EMC planning of sophisticated avionic and other systems.

To obtain maximum accurate information about each possible coupling paths, the EMC analysis tools (computer programs) contain advanced theoretical formulations relevant to the calculation of the electromagnetic field in question. From a theoretical viewpoint, these are known as solution to boundary-value problems. At very high frequencies, and, for geometrically large structures the solutions to such problems can be cast into approximate forms. The approximate forms, that are valid under the above physical conditions, are sufficiently accurate in the prediction

of electromagnetic fields. On cargo aircrafts like C-141 or C-5A, the navigation equipment(s) operate around 1 GHz. For EMC analysis of such cases, these approximate forms are sufficiently accurate. At still higher frequencies the accuracy is expected to increase. In general, then, the EMC analysis codes used in predicting EMI for military and other aircrafts, contain approximate formulations for the creeping wave field. (Some practical EMC analysis programs that analyse EMI on aircrafts are described in the next section.)

Fig. 1.2 shows the effect of the fuselage more clearly. The two situations in Fig. 1.2 are: (i) S and R off, and, (ii) S' and R' on the cylinder. In both these cases the coupling is in the form of a creeping wave. Since the two situations refer to different physical locations, one can expect that a formulation which is specifically formulated to treat off-surface cases, will be invalid for the on-surface case. To be precise, the numerical comparison of the two creeping wave formulations in modeling off and on surface cases is the topic of investigation reported herein.

In the next section, some of the important work reflecting the state-of-art technical work on creeping wave theory and its applications is briefly reviewed here.

1.1 A survey of the relevant literature

High frequency formulation for creeping waves was first developed by Levy and Keller in [9] which is partly heuristic in nature. The authors made some simplifying assumptions which allowed them to extend the principles of optics at relatively low (radar) frequencies. The major criterion is that the object or scatterer dimensions

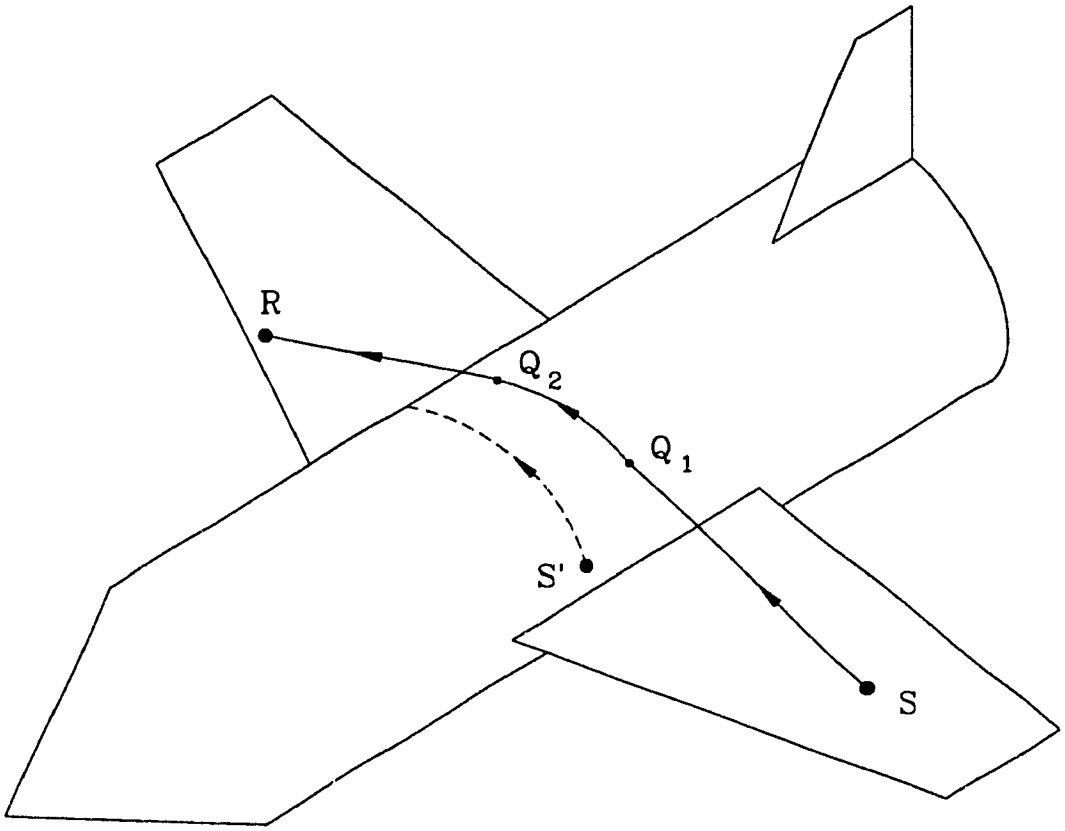

Fig. 1.1. Different coupling paths between antennas on an aircraft. The aircraft is modeled by a circular cylinder (fuselage), circular cone (nose-cone), and, thin plates (wings and vertical stabilizers). The surfaces are assumed to be perfectly conducting. The dotted and solid lines refer to on and off surface locations as shown in the figure.

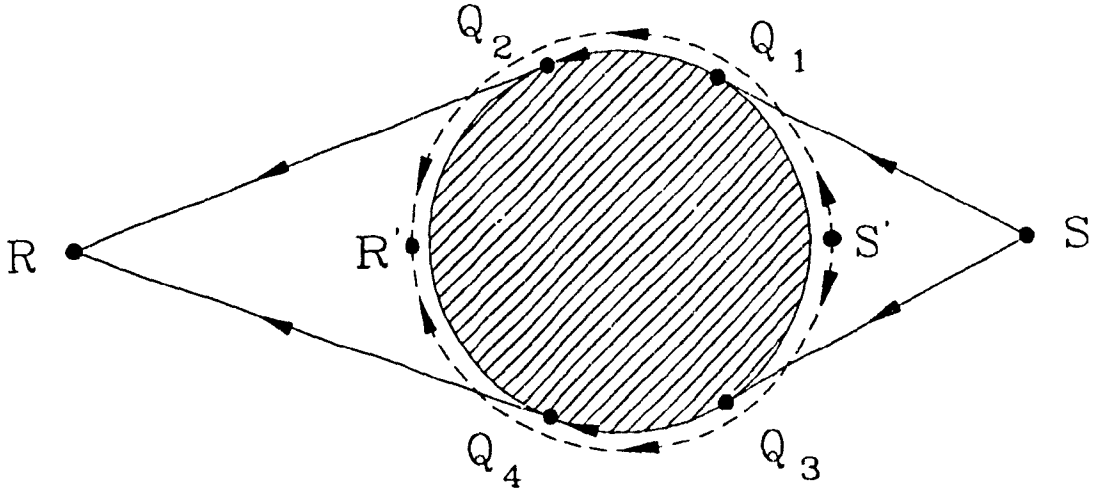

Fig. 1.2. Description of the *canonical* model. Here both paths from the source(s) S or S′ reaching the receiver(s) at R and R′ are shown. UTD scattering (p,q formulations) apply to locations S and R, and, UTD coupling (U, V formulations) apply to S′ and R′. In the above figure Q_3, Q_4 are attachment and launch points respectively for the second path. In both the UTD formulations, two creeping wave paths are used to compute the *total* field at R′ or R.

are very large compared to the wavelength, and, thus one can assume that scattering is a *local* phenomenon. That means one can treat a curved surface, in Levy and Keller's theory, to have properties similar to a circular cylinder at a local point on the generally curved surface. Therefore a curved surface propagation/ scattering problem can adequately be understood by considering the similar problem for a sphere and circular cylinder. This implies that one can analyse the actual problem by considering a simple canonical model.

Levy and Keller extended the laws of geometrical optics to account for fields at regions where a direct source ray cannot reach. The situation has already been shown with reference to Fig. 1.2. It was assumed by Levy and Keller that the Fermát's principle of least path (time) will be obeyed by such class of rays, and, consequently these paths of propagation were geodesics on smooth, convex surfaces. The field along the rays was postulated proportional to a coefficient - which was known as the curved surface diffraction coefficient. As the ray travelled along the geodesic, there was attenuation along the path, and, this attenuation caused the field to decay exponentially. Levy and Keller derived the coefficients for the ray fields by what is known as asymptotic approximation to the exact solution of the relevant boundary value problem. The mathematical details can be found in [9]. This class of curved surface rays that account for diffraction over the smooth convex surface were known as creeping rays. The theory is generally known as the Geometrical Theory of Diffraction (GTD). GTD has found wide application to various problems, and, it has been found that for problems that have no exact solution, or, for which

measured data is not readily available, approximate answers to the problem can be found by employing the GTD.

The above formulation of Levy and Keller considers sources off of the curved surface, *e.g.*, S and R in Figs. 1.1,1.2. For antenna locations at S′ and R′ in the figures, the application of the GTD fails, because the fields become infinite there. An alternative formulation was developed by Hasserjian and Ishimaru [4] who considered sources on a cylinder. The authors of [4] started with the exact solution of the radiated fields from magnetic current elements. The proceedure in obtaining the radiated fields have been developed in detail by Harrington [20, ch. 5, pp. 245-250]. Hasserjian and Ishimaru obatined asymptotic forms of the exact solution and found the surface electric current or equivalently the magnetic field. In [4] the solution was confined to treat large circular cylinders. Later, their work was extended to variable curvature periodic surfaces, by Shapira, Felsen and Hessel [18]. However, the mathematical forms in [18] were restricted to treat slowly varying curvarures, and, some kind of periodic behavior was assumed in theirs', *i.e.* [18], solution. Therefore the form was not general enough for applying to large aircrafts.

In the early 1980's Pathak and Wang of the Ohio State University and S.W.Lee at the University of Illinois, independently developed asymptotic solutions to the original problem of Hasserjian and Ishimaru. Both the groups extended the theory developed by Hasserjian and Ishimaru to include generally smooth convex surfaces which have continuous second derivatives. This means that the geodesics on such surfaces will obey second order differential equations which will have all continuous

solutions. The work of Pathak and Wang and Lee have been described in detail in [3] and [17] respectively. The formulation of Pathak and Wang has a more general relevance, because, the result is expressed in the GTD format. This formulation is well-known as Uniform Theory of Diffraction (UTD) formulation of the coupling problem. Both the results of Pathak and Wang and Lee are in excellent agreement with one another in the deep shadow regions for circular cylinder. In the paraxial zones, Pathak and Wang formulation fails, while, Lee's formulation remains valid there. Lee has not generalized his formulation to treat surfaces other than cylinders and cones. Pathak and Wang have heuristically modified their solution and were able to generalize to arbitrary smooth convex surfaces. Another distinction in the two solutions is that Lee's work does not consider radial monopoles on a cylinder. Thus, from all practical considerations, it appears that Pathak and Wang's formulation has a more broad applicability. Both the formulations [3] and [17], when specialized to the lowest order (dominant) term, yield identical form for a surface magnetic dipole (current element) on a circular cylinder, as, was obtained earlier by Hasserjian and Ishimaru [4]. In summary, the UTD coupling result applies to cases when antennas are at S' and R' as in Fig. 1.2.

The GTD theory of Levy and Keller [9] fails when the observer moves near the shadow boundary (SB) - around the cylinder in the azimuth angle ϕ. These regions in physical space were known as *transition regions*, and, it was apparent that Levy and Keller's work had to be extended for more broader applications. This work was accomplished by Pathak [8] - who began by examining the exact scattering

solution for plane waves by a circular cylinder. Pathak, Burnside and Marhefka [7] later extended the theory to treat scattered fields by actual sources in presence of smooth, convex bodies with perfect conductivity. The feature of their solution was to introduce the Fresnél integral that uniformizes the Levy-Keller solution across the transition region. This maintains the continuity of the solution, and, on both sides of the shadow boundary. The formulation reduces automatically to Levy and Keller's original solution [9] in the shadow region. This formulation is an extension of Levy and Keller's work, and, is known as UTD formulation of curved surface scattering. Computer programs have been developed based on the formulation of Pathak *et al*[7], and, has been incorporated into a user-oriented code known as NEC-Basic Scattering Code, version 2 (NECBSC'2) [5]. In the NECBSC'2 code, a host of UTD scattering formulations are found, and have been successfully been applied in predicting radiation patterns of antennas in presence of complex structures.

In the famous two-volume technical report of Logan [11, vols. 1 and 2], one can find a host of formulas with applications to curved surface scattering. However, in most cases one *does not* find theoretical details of the derivations of these approximate (high-frequency) forms of the formulas, and, hence it is difficult to understand the limitations of these results. Logan has shown that the two categories of problems, *i.e.*, the on and off surface cases shown in Fig. 1.2, are truly different approximations to the same problem. It must be possible in practice to measure the field as one moves in height from the curved surface of the cylinder. This suggests that there should exist a single formula that can predict the field anywhere near

the cylinder. Logan has classified the off surface (UTD scattering) as the optics problem, while, the on surface (UTD coupling) is defined as the radio problem. The optics case is an approximation for large heights, and, the radio case is valid for antennas that are extremely close to the cylinder surface. The two creeping wave formulations are therefore applicable to different physical situations, and, one is not a substitute for the other.

The work of Logan is actually an in-depth exposition of the original work of V.A.Fock and his co-workers. Fock's work can be found in his book [12]. All the work on curved surface diffraction theory is in some way connected to the work of Fock. Fock expressed scattering of plane waves by a cylinder [12, ch. 7, pp. 135 - 146] in terms of two universal integrals that are known as Fock integrals. The method of Fock is to convert the *exact* solution to the scattering problem to a contour integral by Watson transformation. (The Watson transform has been described by Fock and is omitted here.) Next, he (Fock) uses asymptotic approximations. The asymptotic approximations are possible as the quantity,*i.e*, wavenumber×dimension is extremely large for all practical cases. Fock then obtains suitable reductions to the universal integrals in different geomtrical regions. The reader is referred to [12] for details.

The application of Hasserjian-Ishimaru [4], or, Pathak and Wang [3] formulation in predicting EMI coupling between fuselage-mounted antennas has been described in detail by Kubina [11] and Widmer [6]. The formula has been implemented in the widely used Aircraft inter-Antenna Propagation with Graphics (AAPG) code [6].

(Version 7 of the AAPG code and the IEMCAP code used in the U.S.A.F contain identical creeping wave loss formulas. This aspect has been verified in an earlier report [22].) A recent version of the AAPG code, that models coupling on general cylinders, has been developed by Klocko *et al.* [19]. Some recent investigations with the AAPG version 7 and the NECBSC2 code are described below. These recent investigations form a basis of the work reported here in the later chapters.

Validation of the AAPG code was done by Davidson and Thiele [16] for a C-141 military cargo aircraft, where the operating frequency was 1 GHz. Davidson and Thiele found that for finite-length radial monopoles, $\frac{\lambda}{4}$ to $\frac{5\lambda}{8}$ long, the Pathak and Wang formulation and the AAPG code were in excellent agreement.

To extend the use of the AAPG code in the SHF/ EHF band, Genello and Pesta [13] evaluated the results from the code against measured data on a KC-135 aircraft. They found that AAPG code results did not agree with the measured data as the frequency was increased. The results also indicated that AAPG predicts EMI compatibility when incompatibility could be present. RADC then commissioned the Harris Corporation to evaluate the existing creeping wave formulations in the different codes - in search of a state-of-art technique that can be implemented in the existing AAPG code.

Following the recommendations of Genello and Pesta, T.E.Durham at the Harris Corporation performed an extensive set of code comparisons on cylinders with varying cross-sections. Durham had also provided a set of measured data on cylinders for evaluation of the code [10]. The results of both Genello and Pesta [13] and Durham

[10] showed that AAPG code predicted less coupling in the deep shadow regions with increase in frequency. Thus, this implied that the AAPG code could falsely predict EMI compatibility, when, there could be incompatibility between the antennas. The results of T.E.Durham will be referred to as 'Harris results' throughout the remainder of this thesis.

In the recent past, Hussar and Albus [21] had examined the UTD scattering formulation of Pathak *et al.* [7]. They have found, contrary to our present belief, that the UTD scattering formulation, does not reduce properly to the Levy-Keller's creeping wave expressions in the deep shadow for electrically large cylinders. Similar conclusions has independently been reached by examining the results in Chapter 6 of this thesis.

Following Genello and Pesta and Harris conclusions, serious investigations were underway at the EMC Lab in order to assess the accuracy in EMI coupling prediction at high frequencies from the AAPG code. That work has been described in detail in the previous technical reports [22] and [23]. In the next section an overview of the contents in different chapters is described.

1.2 A sketch of contents in this thesis

A description of the AAPG code is presented in Section 2.1 in Chapter 2. In Sec. 2.2 the description of the NECBSC2 code is provided. These descriptions are basically intended to present the reader with an overview of the input/ output modeling characteristics of the two codes. Section 2.3 reviews the results of Genello and

Pesta - which was the start of this investigation. In Section 2.4 the work of Harris is presented. The survey of the results in Sections 2.3 and 2.1 form the basis of the work reported in the later chapters.

Chapter 3 contains numerical results for isotropic coupling gain when antennas are on the cylinder. Section 3.1 presents, briefly, the Pathak and Wang formulation. In Sec. 3.2, the formula used to obtain numerical results for isotropic coupling is derived. Finally, in Sec. 3.3 the numerical results from Pathak and Wang formulation, and, the AAPG code data from Harris report, are shown.

In Chapter 4, Sec. 4.1 presents briefly the UTD scattering formulation for creeping waves. In Sec. 4.2, the method by which Harris NECBSC2 results were obtained, is discussed along with some selected results from an earlier report [22]. In Sec. 4.3, the off-surface data from the NECBSC2 code are compared with the Pathak and Wang, AAPG code and the experimental data. These results have been presented here selectively from [23]. Section 4.4 presents a critical review of Harris model comparisons.

Chapter 5 discusses the limitations of the present AAPG code. This deficiency is also present in the version 9 of the code, though, as shown in this chapter, the results were obtained by examining the circular cylinder case only. Section 5.1 outlines the method by which AAPG code computes coupling gain between antennas on a smooth circular cylinder taking into account the creeping wave attenuation effects. In Sec. 5.2, the validity of the attenuation function L_{cs} is shown for on surface cases. Sec. 5.3 examines the AAPG computation for off surface cases. It is shown that for the

off surface cases, AAPG code results are incorrect because it employs an incorrect mathematical formulation for the relevant physical problem. Finally, in Section 5.4 a review of the results in Secs. 5.2 and 5.3 is provided and their implications on the results in Chapters 3 and 4 are also discussed.

Chapter 6 investigates the problem of nonuniformity in the two formulations in the two codes in detail. It is shown that there exists a critical height, given the geometry and the frequency, below which the NECBSC2 code is expected to give inaccurate results. In Section 6.1, the numerical results showing the possibility of overlap between NECBSC2 code and UTD coupling results are shown. This is followed by the validation of NECBSC2 creeping wave formulations. In Sec. 6.2, the problem of overlap is studied in details for $ka = 10$ and 102. Empirically derived relationships for these two cases are obtained that are useful in applying the NECBSC2 code. Empirical relations in kh vs. ka have also been obtained for $Z_{offset} = 0''$. These relations are basically '*rule-of-thumb*' estimates and allow the designer to have an approximate quantitative estimate regarding the application of the NECBSC2 code in modeling coupling for arbitrary geometrical locations. Section 6.3 discusses the results obtained in Secs. 6.1,6.2 and points out the limitations. This investigation follows the results obtained in Chapters 3,4 and 5.

Chapter 7 presents an overall conclusion of the work in this thesis.

Appendices A.1,2 present two alternate forms for the hard Fock integral. The mathematical development presented here aids one in understanding the exclusive nature of the UTD scattering and coupling formulas. There are some remarks

regarding the material presented in Appendices A.1 and A.3. The form of the hard Fock integral verifies the result of Pathak and Wang [3, Eqn. (49)]. The result in Appendix A.2 is used to establish that NECBSC2 results are indeed invalid close to the cylinder. The results in these two appendices are useful in understanding the mutual exclusivity of the UTD coupling and scattering formulations. (It must be noted that *both* have been obtained from the same *viz.*, generalized hard Fock integral.) It must be mentioned that the final form, *i.e.*, (A3.13) in Appendix A.2, is similar to the one obtained by Pathak in [8]. However Pathak's approach is entirely different from the one followed here. Appendix A.3 presents some typical outputs from the AAPG code when antennas are off the cylinder surface.

Chapter 2

A class of EMI coupling models: present methods and problems

In this chapter, an overall description of the two computer codes that model antenna-to-antenna coupling in presence of cylinders, is presented. The details of the relevant formulations in question is left to the other chapters. The main input/ output issues of the two codes are described here. The discrepancies in model predictions from the earlier work of Genello and Pesta, and, Harris is also reviewed here. The analysis of their results, which is begun in this chapter, is continued in the chapters that follow.

2.1 Modeling of EMI margin using the AAPG codes.

As noted by Kubina in [11], for applications to EMC analysis of advanced weapon systems design, quantitative knowledge of EMI margin plays a decisive role in the evaluation of the safety-factor of such systems. He (Kubina) also shows that the degree of complexity and sophistication of any system, primarily intended for defense applications, requires accurate numerical modeling of several EMI coupling paths, and, corresponding to each of these paths, a '*transfer function*' T_{ij} is obtained. This transfer function is a measure of coupling between the i^{th} emittor and j^{th} receptor. Knowledge of the transfer function represents the intentional, or, un-intentional interaction(s) between a pair of radiators, and, is subsequently used as an entry to a matrix which is known as the Interference Interaction Sample Space. The objective of EMC analysis is to identify those elements of the matrix which can result in an incompatibility, rank them as to severity in preparation for consideration of corrective measures. The T_{ij} is also known as the 'narrowband EMI margin'. Stated in words, the EMI margin is defined as the ratio of undesired signal from an emittor to a receiver, to the threshold sensitivity of the receiver. This definition follows Kubina.

In the AAPG code, which is primarily meant to analyse aircraft mounted antennas and their avionic systems, several such coupling paths are considered. For high-frequency applications, the fields along the paths are replaced by their equiva-

lent 'loss-factors', *i.e.*, edge-shading or curved surface diffraction losses. This method makes the computations simpler.

The AAPG code has interactive graphics facility to enable the user to visually identify the coupling paths. (Some sample outputs from the AAPG code can be found in Appendix A.3 in this thesis.) The numerical values of the losses encountered along the coupling paths are also shown in these displays. The interactive nature of the AAPG code makes it an attractive candidate for fast acquisition, computation and display of data. The details have been provided in the technical report of Widmer.

The quantitative description of EMI margin, following Kubina or Widmer reads:

$$M = P_j + TFS + SF + G_t + G_r - CL_j - CL_i - SR_i \qquad (2.1)$$

In (2.1) the following terms are:

(a) M: EMI margin at receptor 'i' from an emittor 'j'.

(b) P_j: j^{th} emittor power level including applicable harmonic suppression, in dBm.

(c) TFS: free space propagation loss factor in dB.

(d) SF: shading loss factor due to edge diffraction or creeping wave geodesic path loss over the fuselage for the emittor/ receptor pair, in dB.

(e) $CL_{i,j}$: Emitter/ Receptor cable losses in dB.

(f) SR_i: receptor sensitivity threshold in dBm.

(g) $G_{t,r}$: transmitter/ receiver antenna gains in dB along the path.

The 'modified' Friis coupling formula is contained in (2.1). The modification

includes the loss factor SF to account for the structural effects on the propagation path. The form reads:

$$C_{AAPG} = TFS + SF + G_t + G_r \tag{2.2}$$

In (2.2) C_{AAPG} stands for the coupling gain as computed by the AAPG code.

Modeling of an aircraft (see Fig. 1.1) via the AAPG code uses canonical geometrical structures. In version 07 of the AAPG code, the fuselage is modeled by a circular cylinder, the nose-cone by a circular cone, the wings and stabilizers by flat-plates. All the surfaces are assumed to be perfectly conducting. The antennas are defined by directive path gains. Thus, the user of the AAPG code (version 07), defines cylinder geometry, the nose cone, wings and vertical stabilizers in a typical input datafile. The gains have also to be supplied by the user. The code will compute the TFS and SF terms in (2.2).

The antennas can be located arbitrarily in the AAPG code. Ray tracing algorithms, as discussed in detail by Widmer in, are employed to find out the additional ray paths that may be introduced in the coupling mechanism. Thus, AAPG can compute coupling between antennas either *on*, or, *off* the cylinder's curved surface. This specific issue is the central theme of this thesis, and, is reported in detail in the later chapters.

2.2 Modeling of EMI coupling via NECBSC2 code

The NECBSC2 code is a general purpose computer code that can be used to model scattering characteristics of structures illuminated by a source. In this section, the description is confined to antenna-to-antenna coupling in presence of cylinders. (More specific details on the relevant formulations are left for the following chapters.) A detailed description has been provided by Marhefka and Burnside in the User's Manual of the code.

To execute the code, the user has to define the cylinder geometry using the CG card option, and, the source and receiver geometries plus their electrical characteristics defined by the SG and RG card options in an input datafile to the code. To compute the Friis coupling, the user needs to supply the values for the total radiated power for the receiver (P_{rr}) and transmitter (P_{rt}) antennas. Option 3 in the PR card is then used to specifically request for Friis coupling results. The form of this formula is different than the one conventionally used, and reads:

$$C_{BSC} = \frac{1}{16}\frac{|I_r V_{oc}|^2}{P_{rt} P_{rr}}. \tag{2.3}$$

In (2.3) C_{BSC} is the Friis coupling gain as computed by the NECBSC2 code. I_R is the receiver antenna terminal current in amperes. If the user defines a magnetically excited receiver, (such as a slot), then this defined input magnetic current is in volts. NECBSC2 will however convert this current into amperes upon realizing the receiver type. V_{oc} is the *open circuit voltage* expressed in volts, and, depends on the type of

field reaching the receiver. The type of field will depend on the ray configuration that the code determines via its ray tracing algorithm.

The NECBSC2 code computes the fields according to the laws of ray-optics. The theoretical summary of the different formulations for the several ray fields can be found in the Ohio State University short course notes [15]. (For example, the curved surface GTD formulations can be found in the notes of Marhefka and Wang.) A more deeper understanding of the theoretical developments of the formulations, can be found in the works of Kouyoumjian and Pathak.

Antennas cannot be mounted on the curved part of the cylinder in the NECBSC2 code. This is due to theoretical limitations in the NECBSC2 code. (A detailed numerical analysis on this issue has been presented in a later chapter of this thesis.)

Comparing the algebraic forms, *i.e.*, (2.2 and 2.3) for the Friis coupling gain, one notices the differences in the structure of the formula used by both the codes. Due to this reason, the user defines the same input configuration differently for both the codes. The NECBSC2 will consider the vector nature of the scattered field, and, the radiated field of the receiver antenna. The AAPG code will define Friis coupling by the antenna gains, and, the scalar loss factors (defined by SF in (2.2)). Therefore, the NECBSC2 computation may be sophisticated, but, too intensive for use in EMC analysis programs like the AAPG code that are required to produce fast and accurate results.

It is also to be noted that though (2.2 and 2.3) are equivalent, results from both the codes will differ significantly for the same input configuration, if the formulation

for the scattered field (as used by the NECBSC2 code), and, the loss factors (as used by the AAPG code) are not the same. (This issue has been discussed in the following sections.)

2.3 Recent evaluation of AAPG code at RADC

To evaluate the prediction accuracies of a code, it is necessary to assess the numerical model against measured data. For applications to aircrafts with large cross-sections and high frequencies, it becomes necessary to evaluate the AAPG code predictions with increase in frequency.

Genello and Pesta began evaluating the AAPG code against actual measurements taken on a KC-135 aircraft. The authors found, that, for antennas completely shadowed from each other by the fuselage, AAPG code predicted more isolation than one obtained from measurements. Their results, digitized from [13], are shown in Fig. 2.1.

In Fig. 2.1, one can clearly see that at f= 2 GHz, the difference between the measured and computed data is 8 dB. At 18 GHz, this difference increases to 28 dB. Based on such observations, Genello and Pesta recommended that a thorough evaluation of the AAPG codes shading loss formulations be done before extending the use of the code in the SHF/ EHF band. As shown in Fig. 2.1, this investigation turned out be very important because their data show that AAPG could lead to false EMI predictions between fuselage mounted antennas at high-frequencies. Thus, the authors made strong recommendations in search of an advanced high-frequency

shading loss formulation than the one existing in the AAPG code, and, for its practical implementation in the AAPG code.

2.4 NECBSC2 and AAPG code comparisons by Harris Corporation.

Following the recommendations of Genello and Pesta, the Harris Corporation was commissioned by Rome Air Development Corporation (RADC) to carry out the task of comparing several formulations in search of a better surface shading loss formula, and, for its implementation in the AAPG code. Extensive code comparisons had been performed by Harris who also reported experimental results. The report contains data for several types of cylinders of varying cross sections. The canonical model of a circular cylinder has been treated in detail by Harris. To study the effects of polarization, Harris chose TE and TM polarizations - corresponding to axial and circumferential slots respectively.

In the process of code comparison, Harris modified the NECBSC2 code to include an isotropic source pattern - which was used in all the subsequent calculations. Since the NECBSC2 code requires source locations to be off the surface, Harris had located sources a '*quarter wavelength*' off the cylinder. The numerical results of Harris corresponded to both C vs. f and C vs. ϕ variations, but, the measured data can only be found for the C vs. f case. It is important to note that Harris did not present any details regarding the numerical data on which they based their

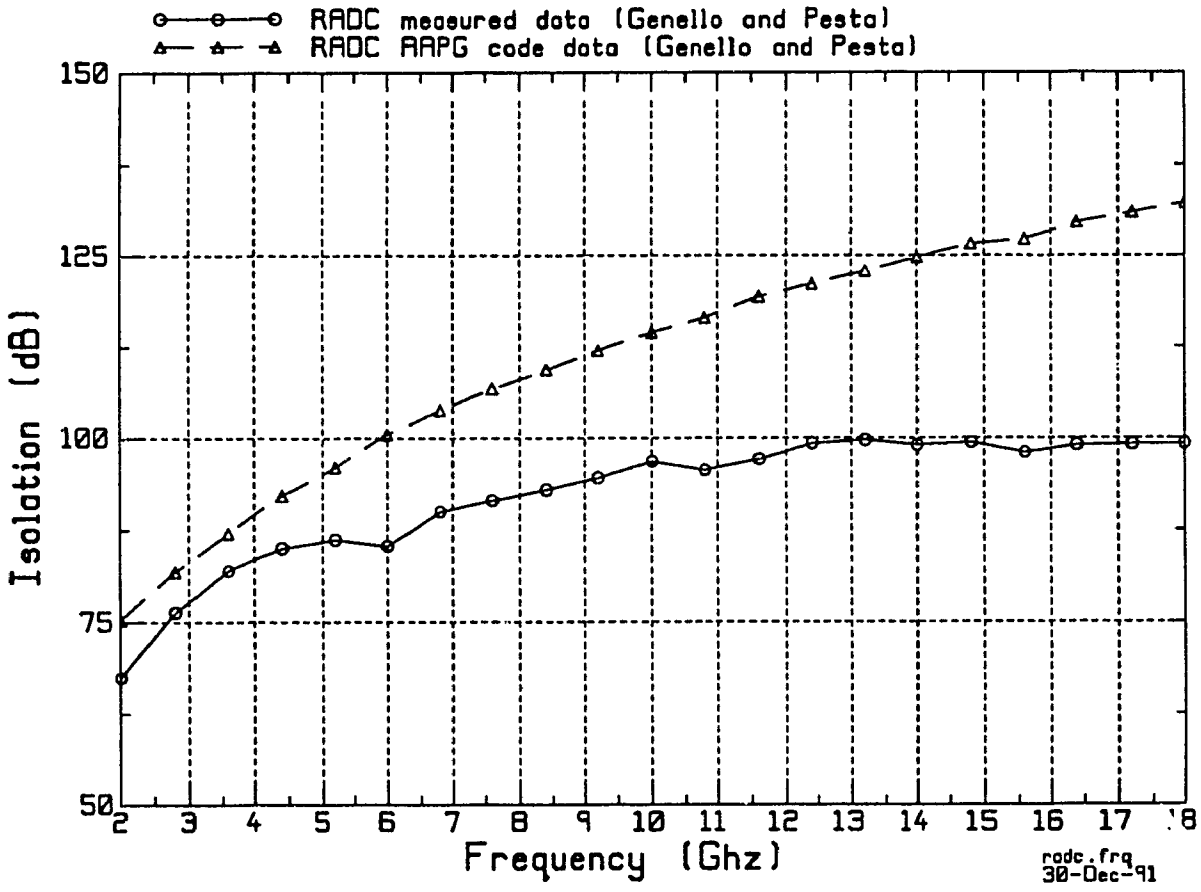

Fig. 2.1. Typical data from Genello and Petsa's paper [13]. The result generally indicates that AAPG code predicts *more* isolation than that would exist for antennas mounted on the fuselage. The data refers to KC-135 aircraft. The result shown, indicates that AAPG code's prediction degrades with increase in frequency. This result strongly suggested that the AAPG code could lead to false EMI predictions at high frequencies between a pair of fuselage-mounted antennas.

conclusions. It must be noted that Harris comparisons were for off (NECBSC'2) and on (AAPG) surface cases. (These issues are discussed in the later chapters.)

A typical result, (which was reported to be the worst case in Harris report), is shown in Fig. 2.2. This result shows that, with increase in frequency, AAPG code predicts less coupling than either TE, TM results from the NECBSC'2 code. As this data had similar implications like the result of Genello and Pesta, Harris concluded that AAPG codes shading loss formulation is indeed inaccurate at high frequencies. Harris data and conclusions led to further investigations, that have previously been described in [22] and [23], and, are described selectively in this thesis.

The motivation for further work began following the results shown in Figs. 2.1 and 2.2. Both Harris and Genello and Pesta's work showed that AAPG code could lead to false EMI predictions at high frequencies. As Harris had provided extensive computed and measured data for the basic circular cylinder model, it was decided to examine the validity of his results for this simple case. Furthermore, this validation would also lead to an understanding of any deficiencies in the version 07 of the AAPG code - that models the fuselage by a circular cylinder.

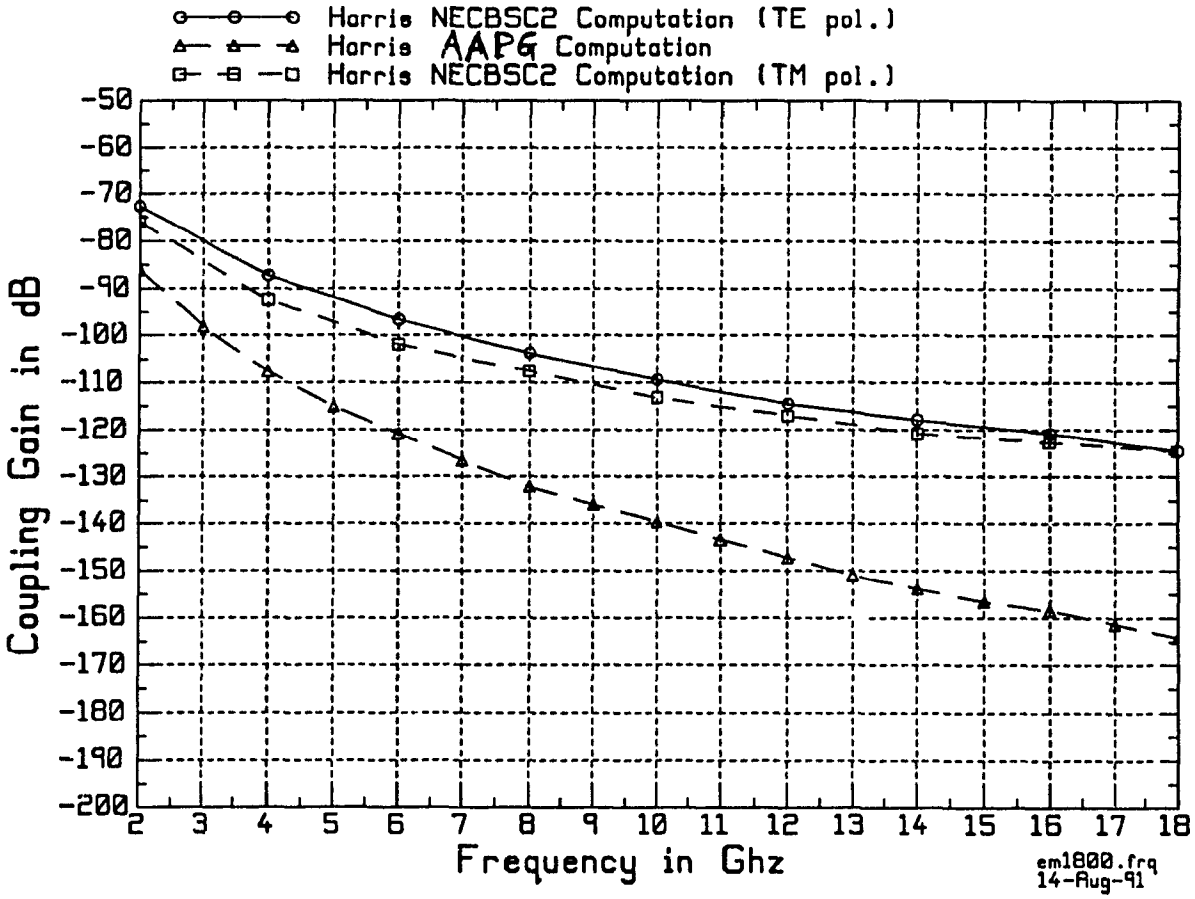

Fig. 2.2. Typical data from [10, p. 77] showing the *high-frequency, large ϕ angle* discrepancies between the AAPG and NECBSC2 code predictions for $\phi = 180^0$, $Z_{offset} = 0''$, R= 24" and TE, TM polarizations. The difference at 2 GHz between NECBSC2 (TE) and AAPG code is 10 dB; at 18 GHz it is 40 dB. The comparsion shows that AAPG code predicts less coupling than the NECBSC2 code as the frequency is increased.

Chapter 3

Antenna coupling on the cylinder surface

In this chapter, the U, V formulation is introduced in Sec. 3.1. In Sec. 3.2, the isotropic Friis coupling gain from Pathak and Wang theory is found to the lowest order term. In Section 3.3 numerical results from the U, V formulation, and, the one from AAPG code have been compared. The AAPG data has been directly obtained from Harris report.

3.1 U, V, or, the Pathak and Wang coupling formulation.

In this chapter, we examine a class of formulations that apply to those coupling situations where antennas are mounted on the curved part of the cylinder. For our

discussions one can refer to Fig. 1.2, where the antenna positions are S′ and R′. The mathematical details of these formulations are quite involved, and, they can be found in the references listed here. To this end, we begin by examining the well-known Pathak and Wang (U, V) formulation, which determines the surface, or, creeping wave field due to an infinitesimal magnetic or electric current source. The surface electric field due to a magnetic current element reads:

$$\vec{\mathbf{E}}_{\mathbf{m}}(R'/S') = -\frac{jke^{-jkt}}{2\pi t} d\vec{\mathbf{p}}_{\mathbf{m}}(S').\overline{\overline{\mathbf{\Gamma}}}_m. \tag{3.1}$$

Similarly, for a radial electric current source, the field will read:

$$\vec{\mathbf{E}}_{\mathbf{e}}(R'/S') = -\frac{jke^{-jkt}}{2\pi t} d\vec{\mathbf{p}}_{\mathbf{e}}(S').\overline{\overline{\mathbf{\Gamma}}}_e. \tag{3.2}$$

In (3.1,3.2), the *surface dyadics* $\overline{\overline{\mathbf{\Gamma}}}_{e,m}$ are given by:

$$\overline{\overline{\mathbf{\Gamma}}}_m = \hat{b}'\hat{n}\left(\left(1-\frac{j}{kt}\right)V_0(\xi) + T_0^2\left(\frac{j}{kt}\right)[U_0(\xi)-V_0(\xi)]\right) + \hat{t}'\hat{n}\left(T_0\left(\frac{j}{kt}\right)[U_0(\xi)-V_0(\xi)]\right) \tag{3.3},$$

and,

$$\overline{\overline{\mathbf{\Gamma}}}_e = \hat{n}'\hat{n}\left(V_0(\xi) - \frac{j}{kt}V_0(\xi) + \left(\frac{j}{kt}\right)^2 U_0(\xi) + T_0^2\frac{j}{kt}\left[U_0(\xi)-V_0(\xi)\right]\right). \tag{3.4}$$

In Eqns. (3.1 to 4), t is the geodesic path from S′ to R′ in (3.3,4). The superscripts (primes) on the unit vectors indicate evaluation at the source location S′. The primeless unit vectors are evaluated at the receiver R′. We can write for the Fock parameter ξ and geodesic length t as:

$$t = \frac{a\phi}{\sin\theta_g} \tag{3.5},$$

and,

$$\xi = \left(\frac{ka \sin\theta_g}{2}\right)^{\frac{1}{3}} \phi. \tag{3.6}$$

Figs. 3.1,3.2 and 3.3 describe the geodesic t, the Fock parameter ξ and the angle θ_g used in Eqns. (3.5) and (3.6).

The quantity $T_0 = \cot\theta_g$ in (3.3,4) is a measure of *torsion* on the geodesic path, and, depends on the axial separation Z_{offset} between the two antennas, and, the '*two-dimensional*' geodesic path $t_{xy} = a\phi$. It must be noted that Eqns.(3.1,3,4) all apply to any smooth, convex surface. (This allows modeling of antenna-to-antenna coupling for locations on general fuselage cross-sections.) However, for the discussions contained in this report, (3.5,6) refer only to circular cylinders. (More general formulas for t, ξ, T_0 have been provided by Pathak and Wang.)

The quantities $V_0(\xi)$,$U_0(\xi)$ are the '*zeroth-order*' hard and soft surface Fock functions, studied extensively by Logan, and, also by Pathak and Wang, and, Lee. These functions are used to find the attenuation effect(s) due to curvature of the geometry and the wavenumber k, or, frequency of propagation. It has been shown by Pathak and Wang that for the limiting case, when the radius of the curvature tends to become *infinite*, these hard and soft Fock functions tend to unity. This is physically expected because for extremely large radii, the propagation path is essentially the same as that on a ground plane, and hence no attenuation is expected.

The binormal, normal and tangent unit vectors at any point along the geodesic path between S' to R' are given by:

$$\hat{\mathbf{b}} = -\cos\theta_g \sin\phi\hat{\mathbf{x}} + \cos\theta_g \cos\phi\hat{\mathbf{y}} - \sin\theta_g\hat{\mathbf{z}} \tag{3.7}$$

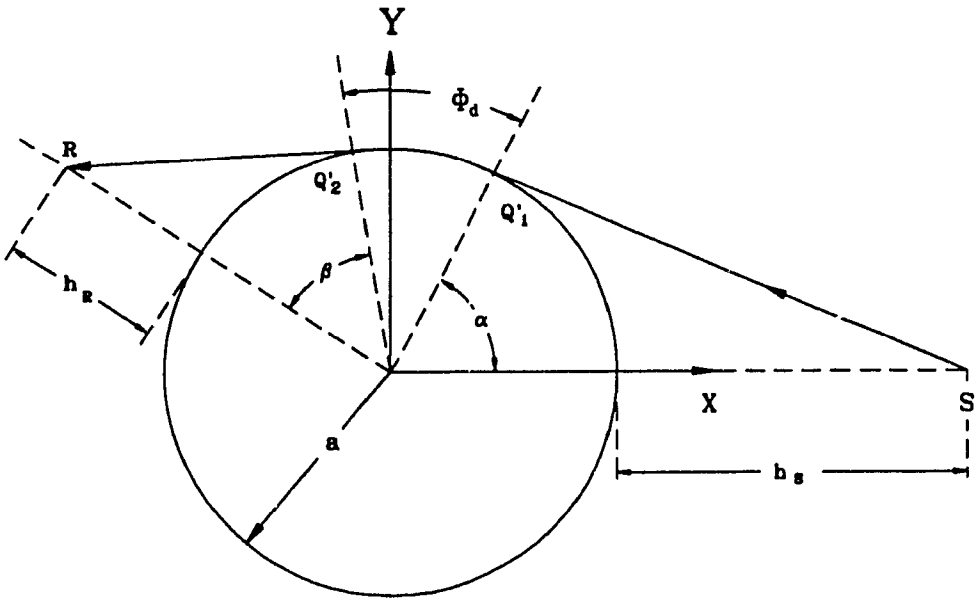

Fig. 3.1. Simplified 2-D view of Fig. 1.2. $h_{s,r}$ define the actual heights of antennas off the cylinder. $s_i = SQ'_1$, $s_d = Q'_2R$ and the geodesic length, $t = Q'_1Q'_1$. The angular location of the receiver w.r.t the source is: $\phi_R = \alpha + \phi_d + \beta$. The angles α, β can be computed from the geometry. The total distance between the antennas is $L = s_i + t + s_d$. The grazing angle is given by: $\phi_{grz} = \alpha + \beta$. For all locations given by $\phi_R > \phi_{grz}$, creeping waves exist. The Fock parameter ξ defined in Eqn. (3.6) is computed over the curved path $Q'_1Q'_2$.

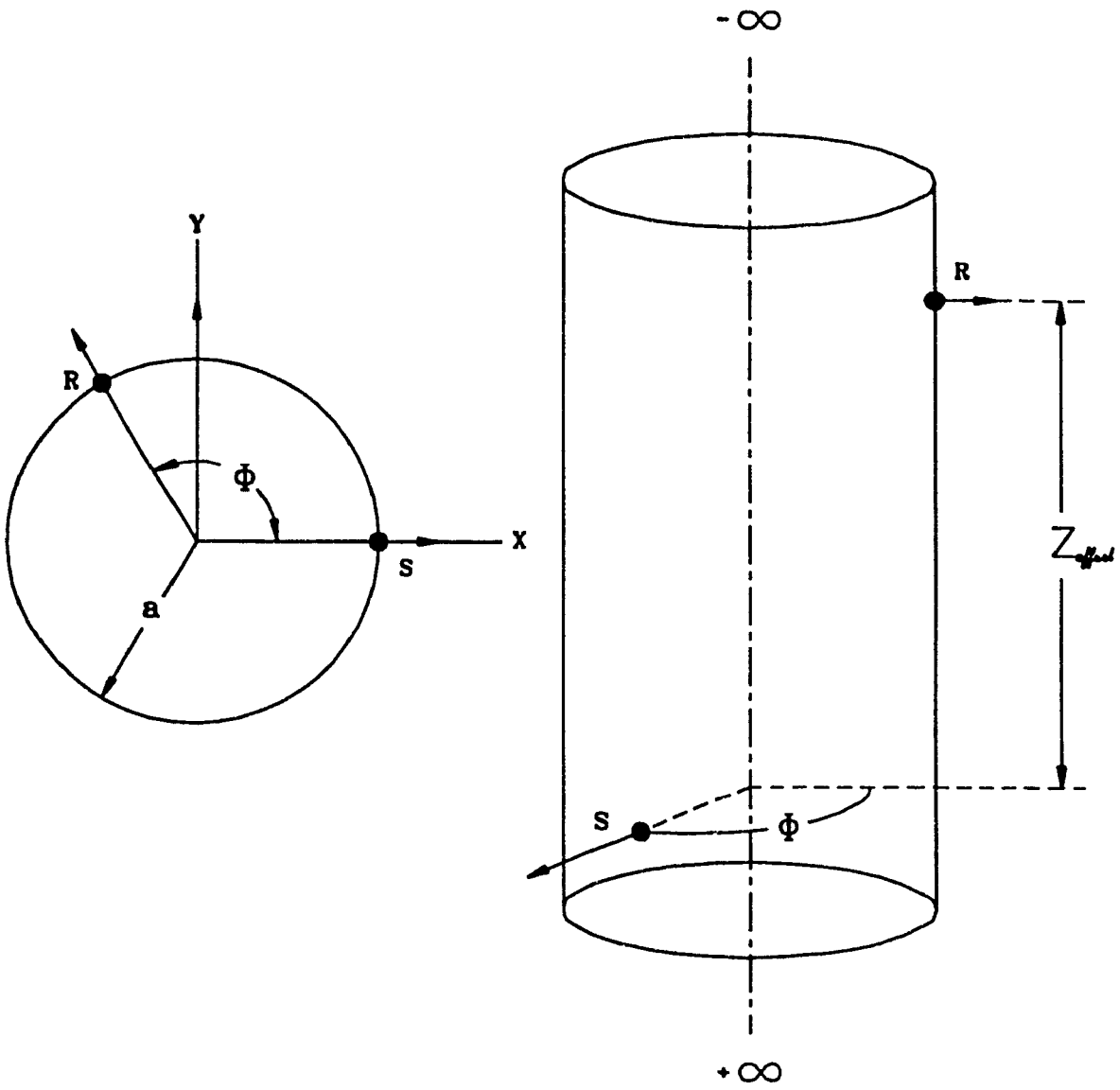

Fig. 3.2. Description of the geometry of the circular cylinder used to model the fuselage of an aircraft. ϕ is the azimuthal angle, Z_{offset} is the axial separation, a is the cylinder radius. The geometry is common to both U, V formulation and the AAPG code (version 7).

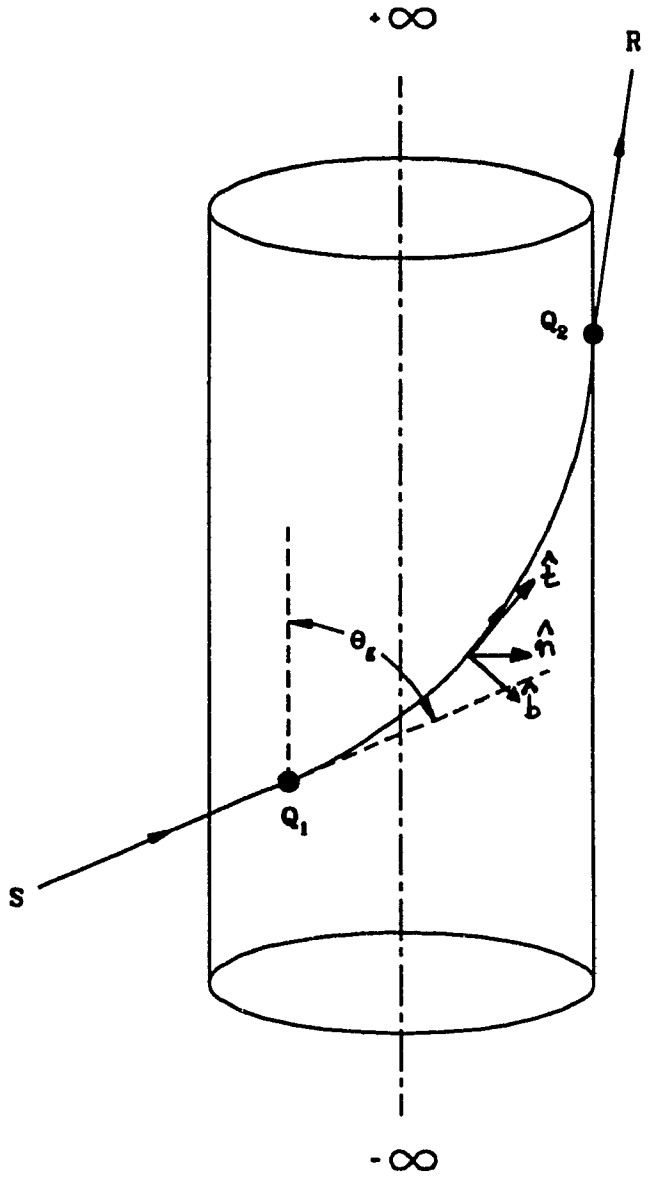

Fig. 3.3. *Geodesic* path between the two antennas S,R is shown. θ_g is the geodesic angle which appears in Eqns. (3.5,6) in Chapter 3. $Q_{1,2}$ are the *attachment* and *launch* points. Only one path is shown. The special case of $\theta_g = 90^0$ is a *torsionless* path. Other paths for which $\theta_g \neq 90^0$ are known as *torsional* paths. The unit normals, binormals, and, tangent vectors $\hat{\mathbf{n}}, \hat{\mathbf{b}}, \hat{\mathbf{t}}$ are shown here.

$$\hat{\mathbf{n}} = \cos\phi\hat{\mathbf{x}} + \sin\phi\hat{\mathbf{y}} \tag{3.8}$$

$$\hat{\mathbf{t}} = -\sin\theta_g \sin\phi\hat{\mathbf{x}} + \sin\theta_g \cos\phi\hat{\mathbf{y}} + \cos\theta_g\hat{\mathbf{z}}. \tag{3.9}$$

In (3.7,8,9), the triad $(\hat{x}, \hat{y}, \hat{z})$ form a right-handed system in the Cartesian coordinates. These are evaluated in (3.1 to 3.4) at *both* source S′ and receiver R′ locations. Fig. 3.3 also shows these unit normals at any arbitrary point on the geodesic path.

To discuss the formulations (3.1,2) more effectively, and, for future numerical comparisons with the results from the AAPG code, we may simplfy the formulas in Eqns. (3.1,3.2) to the lowest or $O(kt)$ term. One must note that there are two rays from S′ to R′ as shown in Fig. 1.2. Therefore, the total field at R′ is the vector sum of the quantities in (3.1,3.2) over the two paths. It is also to be understood that $d\vec{\mathbf{p}}_\mathbf{m} = \hat{\mathbf{u}}_t M_0$ and $d\vec{\mathbf{p}}_\mathbf{e} = \hat{\mathbf{u}}_t \eta_0 I_0$. $\eta_0 = 376.73\Omega$. For a radial electric element $\hat{\mathbf{u}}_t = \hat{\mathbf{n}}'$; for circumferential elements, $\hat{\mathbf{u}}_t = \hat{\phi}$. $\hat{\mathbf{z}}, \hat{\phi}$ are unit vectors in the standard cylindrical coordinate system. $\hat{u}_t$ represents the unit vector along the orientation of the current element. Retaining only to $O(kt)$ terms in Eqns. (3.2,4) for a radial electric element, we have,

$$\vec{\mathbf{E}}_t(R'/S') = \frac{jk\eta_0 I_0 \epsilon^{-jkt}}{2\pi t}\hat{\mathbf{n}}V_0(\xi) \tag{3.10}.$$

Eqn. (3.10) implies:

Field on a cylinder=Field on an infinite ground plane$\times V_0(\xi)$.

Here $V_0(\xi)$ is the correction factor for the curvature due to the curved part of the cylinder.

In the $\theta_g = 90^0$ ($Z_{offset} = 0''$) plane, the source-excited fields from axial magnetic and radial electric elements to be identical when the current moments are of the

same magnitude. However, in the same plane, the circumferential source does not produce any field to the $O(kt)$ term. (In the latter case, only the *higher order terms* in (3.1) contribute in the $\theta_g = 90^0$ plane.) Therefore on the torsionless path, for axial magnetic or radial electric sources, the surface fields are each individually stronger than the one due to a circumferential source.

The U, V formulation allows antennas to be located off the cylinder. This implies that a *height factor* can be incorporated. Since AAPG code can also compute the case for antennas off the surface, this aspect of the U, V formulation deserves some special attention. One can refer to Fig 3.1 for a general overview of the geometry involved.

The effect of this modification is to replace $V_0(\xi)$, $U_0(\xi)$ by the $F_{s,h}(\xi, y_s, y_r)$ functions. The function $F_{s,h}$ is such that for vanishingly small heights, the original formula (3.10) is recovered. Thus, including this height factor, the creeping wave field due to sources raised '*slightly*' above the cylinder is given by:

$$\vec{\mathbf{E}}_c = \frac{jk\eta_0 I_0 \epsilon^{-jkt}}{2\pi t} \hat{\mathbf{n}} F_h(\xi, y_s, y_r). \tag{3.11}$$

Lastly, the *reduced* heights $y_{s,r}$ are given by:

$$y_{s,r} = \frac{kh_{s,r}}{m(S', R')}. \tag{3.12}$$

In (3.12), we have the transition quantity $m(Q)$ given by:

$$m(Q) = \left(\frac{ka}{2\sin^2\theta_g}\right)^{\frac{1}{3}}. \tag{3.13}$$

In (3.13) Q is any point on the geodesic. $h_{s,r}$ are the actual heights of the source S' and receiver R' above the curved surface of a cylinder - as shown in Fig. 3.1.

3.2 Coupling gain from U, V formulation.

The free-space, direct source field reads for a electric current element as:

$$\vec{\mathbf{E}}_e = -\hat{\theta}\frac{jk\eta_0 I_0 e^{-jkt}}{4\pi t}\sin\theta \tag{3.14}$$

The short electric dipole has a current moment I_0 (in amperes), and, is along the Z-axis at the origin of a standard right-handed cartesian coordinate system. The observation point is in the Z-Y plane and on the Y-axis. $\eta_0 = 376.73\Omega$ is the free-space impedance. In (3.14) t is the distance between the antennas. θ is the elevation angle measured in the positive (anticlockwise) sense from the Z-axis. It is important to note that:

Field on a ground plane= 2×Field in free space given by (3.14)

When $\xi \rightarrow 0$, $V_0(\xi) \rightarrow 1$ in (3.10). In this situation, the field given by (3.10) is double in magnitude to the free-space field given by (3.14). Thus the Friis formula, that employs free-space fields, will be modified by the factor $V_0(\xi)$ to account for the curvature effects of the surface. This suggests writing the 'modified Friis formula', as used in the AAPG code, in the following form:

$$C = \frac{P^T_{rec}}{P^T_{in}} = \left(\frac{\lambda}{4\pi t}\right)^2 G_t G_r |V_0(\xi)|^2. \tag{3.15}$$

Here $P^T_{rec,in}$ are the <u>total</u> power received and input to the transmit and receive antennas. For sources slightly above a curved surface, one can replace $V_0(\xi) \rightarrow F_h(\xi, y_s, y_r)$ in (3.15). To obtain the total coupling at the receiver location, one needs to compute the coupling due to two creeping rays as shown in Fig. 1.2.

3.3 Numerical comparison of U, Vformulation and the AAPG code for antennas on surface

In this section, numerical results from (3.15) and the AAPG code results of are compared. The AAPG results were directly digitized from the Harris technical report. In this comparison, the antennas were located on the curved surface of the cylinder - implying $y_s = y_r = 0$ in the F_h function. The comparison shown here for the few selected cases from [23] refer to both C vs. f and C vs. ϕ cases.

To obtain results from (3.15), a computer program was written based on Eqns. (3.11) and (3.15). This program contains a shadowing algorithm that is an improved version from the one in Davidson's thesis. The algorithm basically checks if the receiving antenna is below the grazing line, or, is shadowed by the cylinder. Both the creeping ray paths are being determined and the field along the paths are also computed. The program runs on the VAX 6510 computer at the Concordia University and to compute for 501 datapoints, it takes about 0.71 secs of C.P.U time for the C vs. ϕ case. In this case we ran the code by selecting the input data corresponding to f= 8 GHz, $Z_{offset} = 360''$ and $a = 24''$. The antennas were located on the cylinder. If the antennas are located off the surface by say h= 0.0375 m and the starting angle (selected arbitraily) is 10^0, then the code begins all the coupling calculations from $\phi = 39.2^0$. (This is the grazing angle below which the creeping rays exist.) For 501 datapoints the code takes 0.61 secs of C.P.U time. The input data for the dimensions to the code are in inches, and, the code runs interactively

on the VAX computer.

The results from Eqn. (3.15) are compared against the digitized AAPG data from Harris report, and, are shown in Figs. 3.4 to 3.7. Results form the above computer program will be referred to as 'U, V' formulation results in the remainder of this thesis.

Fig. 3.4 shows the C vs. f result at $\phi = 60^0$. At this location, we see excellent agreement between the two results. This, as mentioned earlier, is due to the fact that at $\phi = 60^0$, the coupling is dominated by the field due to the shorter path; the attenuation on the larger path is extremely large and hence the contribution to the total coupling from the second path is negligible.

Fig. 3.5 shows the AAPG data is 6 dB lower than the two ray result from (3.15). At $\phi = 180^0$, the two rays are equal and the total coupling will be 6 dB more than that from a single ray. This explains the 6 dB difference between the one from (3.15) and that from the AAPG code.

Fig. 3.6 refers to the torsional geodesic path at $Z_{offset} = 360''$ and $\phi = 150^0$. One can clearly observe the effect of interference in the form of oscillations in our two ray result from (3.15). In this situation, as the frequency or wavenumber k changes, the phase term - given by kt in (3.11) changes over both the ray paths. Note that since the geometry remains fixed, t, does not change. When there is a phase addition (reinforcement), peaks occur; for phase cancellation from the two paths, nulls are seen in Fig. 3.6. The single ray AAPG data lies in-between the peaks and nulls.

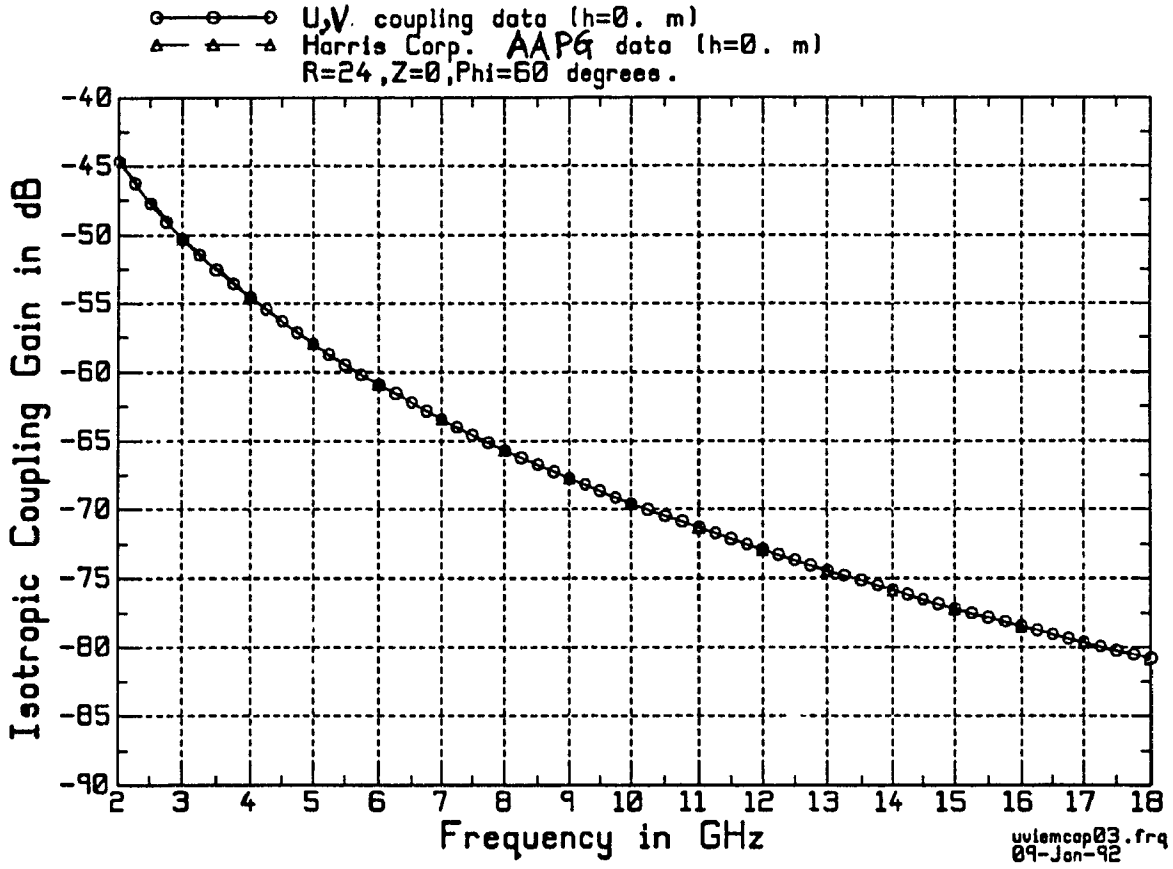

Fig. 3.4. Comparison between U, V and AAPG code results. The AAPG data refers to Harris report [10, p. 73]. The U, V data is for two creeping wave paths while the AAPG data is for a single, or dominant geodesic path.

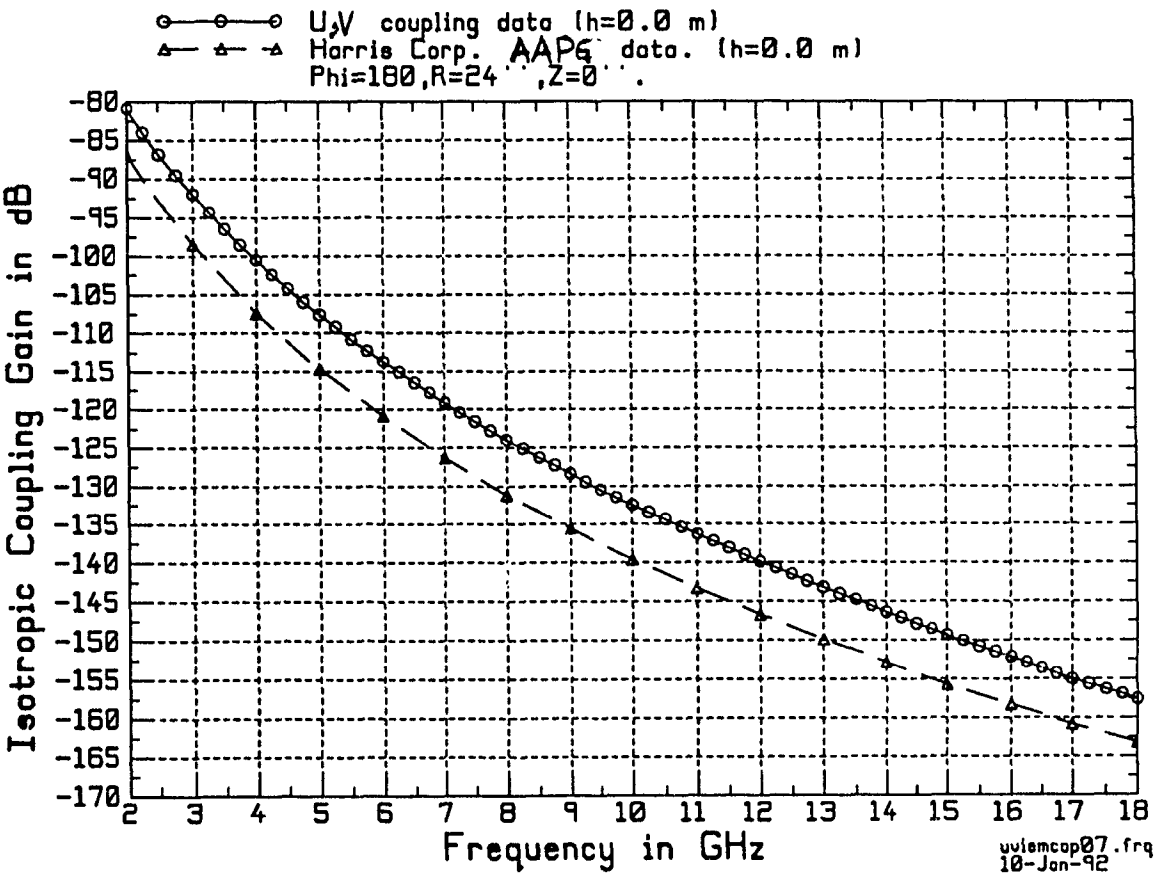

Fig. 3.5. Comparison between U, V and AAPG code results. The AAPG data refers to Harris report [10, p. 77]. The U, V data is for two creeping ray paths, while the AAPG data is for the single, or dominant geodesic path.

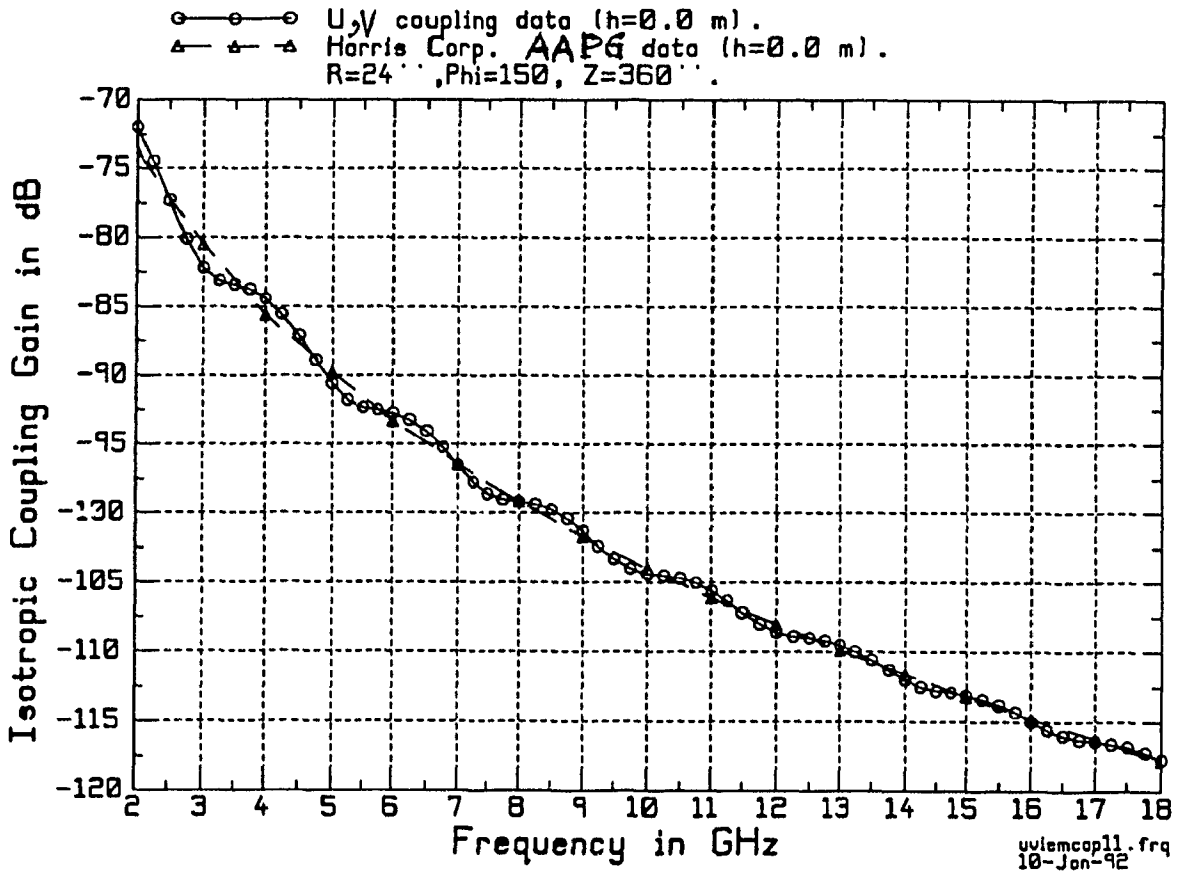

Fig. 3.6. Comparison between U, V and AAPG 'e results. The AAPG data refers to Harris report [10, p. 91]. The U, V data is for two creeping ray paths while the AAPG data is for the single, or dominant geodesic path.

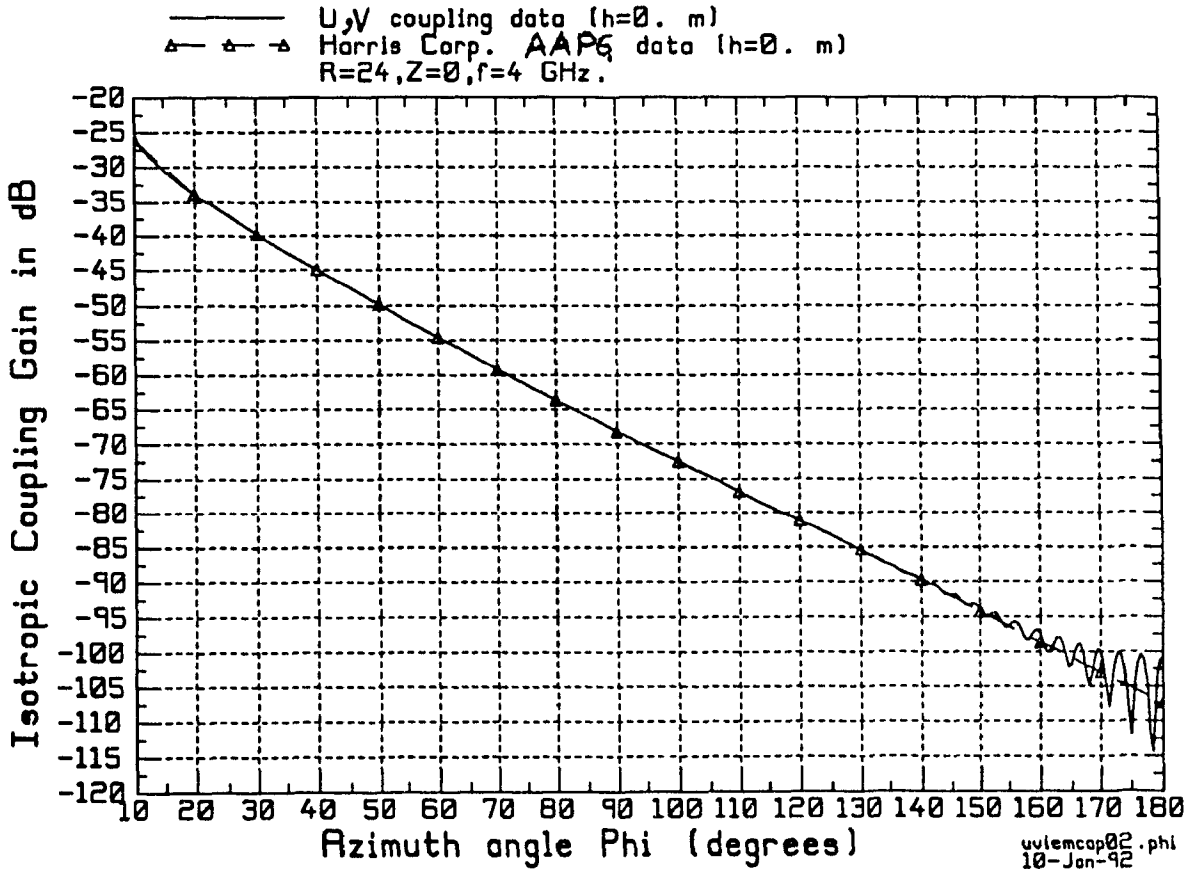

Fig. 3.7. Comparison between U, V and AAPG code results. The AAPG data refers to Harris report [10, p. 57]. The U, V data is for two creeping ray paths while the AAPG data is for the single, or dominant geodesic path.

Fig. 3.7 refers to the C vs. ϕ case at 4 GHz and $Z_{offset} = 0''$. We see that upto $\phi \simeq 40^0$, the AAPG results overlap with our two ray data. This indicates that the total coupling is dominated by a single ray upto 140^0. Beyond 140^0, the peaks and nulls occur in our data. The AAPG data, beyond $\phi \gtrsim 140^0$, lies in-between the peaks and nulls. At exactly $\phi = 180^0$ in Fig. 3.7, the AAPG data is exactly 6 dB less than the total coupling here. It is also interesting to note that for $170^0 \leq \phi \leq 180^0$, the peaks and nulls in our results are almost of the same magnitude. This indicates that over the two paths at this location, the attenuation are almost the same and the field magnitudes are almost equal. This small angular portion reminds one of the 'lossless' transmission line behavior of the creeping rays.

The results show that for on surface locations, the AAPG code is in excellent agreement with the data from the *U, V* formulation. Additional computations have been performed and lead to identical conclusions. These additional results can be found in [23].

In the next chapter, comparison between 'on' and 'off' surface coupling cases is discussed.

Chapter 4

Antenna coupling off the cylinder surface

In this chapter, the UTD scattering formulation for creeping waves is described briefly in Section 4.1. In Section 4.2 the method by which Harris data was replicated is summarized from an earlier report [22]. Section 4.3 compares the NECBSC2, U, V formulation, AAPG code and experimental data. Section 4.4 presents a critical review of Harris model comparisons.

4.1 Scattering by a smooth convex cylinder; UTD scattering formulations.

The creeping wave formulations in NECBSC2 code have been derived by Pathak. This expression reads:

$$\vec{\mathbf{E}}(\mathbf{P_s}) = \vec{\mathbf{E}}^{\mathbf{i}}.\overline{\overline{\mathbf{T}}} \times \sqrt{\frac{\rho^d}{s^d(s^d+\rho^d)}} e^{-jks^d}. \tag{4.1}$$

In Eqn. (4.1) the following terms are defined :

(i)$\vec{\mathbf{E}}^{\mathbf{i}}$ is the incident field at the attachment point Q_1 from a source located at a distance s^i, measured from the source location to the attachment point on cylinder surface. In NECBSC2 the sources are described by *free-space radiation* patterns.

(ii)$\rho^d = t + s^i$ is one of the radii of curvature of the diffracted wavefront.

(iii)s^d is the distance from the launching point Q_2 of the surface ray to the observation point P_s which is *off* the cylinder surface.

(iv)$\overline{\overline{\mathbf{T}}}$ is the known as the *generalized transfer dyadic* that transforms the incident field $\vec{\mathbf{E}}^{\mathbf{i}}$ to a creeping wave field denoted by $\vec{\mathbf{E}}(\mathbf{P_s})$ at the point P_s in the shadow.

(v)The quantity under the square root in (4.1) is known as the *divergence factor* and described as the spreading of a *tube of rays* due to surface curvature [2, p. 308].

Fig. 4.1 shows the diffraction by a general, smooth convex surface.

Eqn. (4.1) indicates that as $s^d \rightarrow 0$, or, observer point comes near to the cylinder surface, the field predicted by (4.1) becomes *infinite*. This is a *restriction* that must be borne in mind while applying (4.1), or, equivalently NECBSC2 code, as, the true

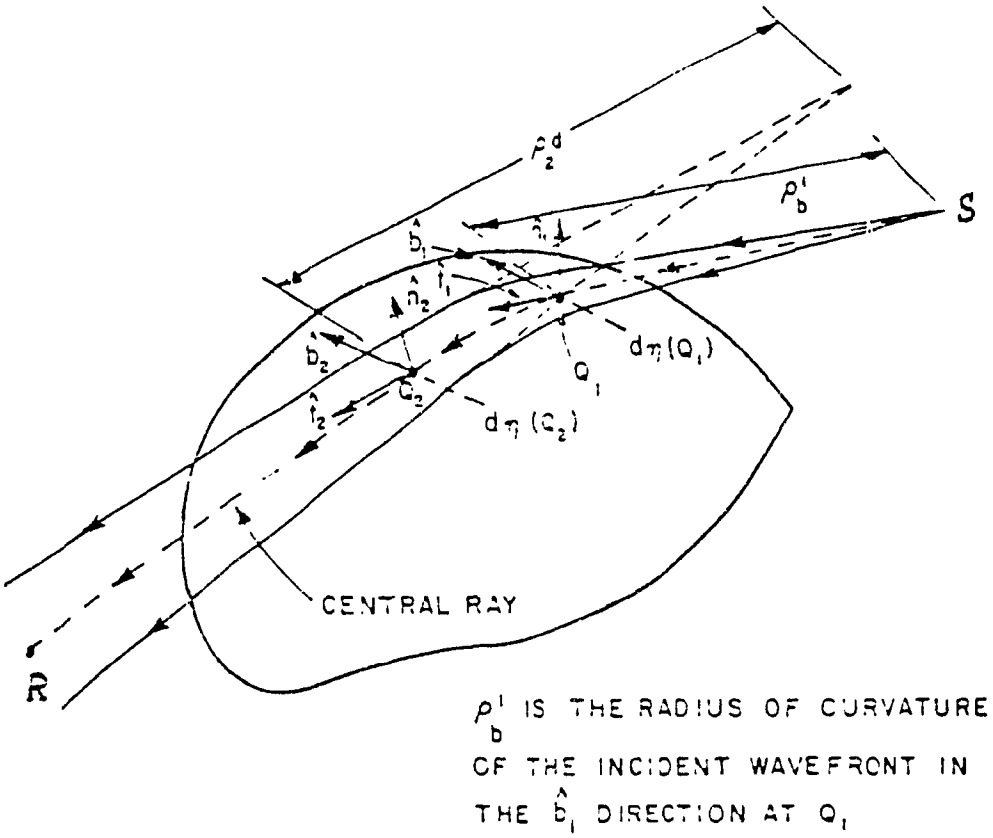

Widths $d\eta(Q_1)$ and $d\eta(Q_2)$ of the surface ray strip

Fig. 4.1. Diffraction by a convex surface, from [2, p. 314]. S and R are source receiver locations. Eqn. (4.1) refers to the field on the central ray. The distance from S to Q_1 is s^i, and, that from Q_2 to R is s^d. $\hat{\mathbf{b}}_{1,2}$ are the unit *binormals*, $\hat{\mathbf{n}}_{1,2}$ are the unit *normals*, and, $\hat{\mathbf{t}}_{1,2}$ are the unit tangents at $Q_{1,2}$ which are the *attachment* and *launch* points respectively. The *geodesic* length t is from $Q_{1,2}$, given by Eqn. (3.5).

field *cannot* be infinite close to the cylinder surface, from physical considerations.

It is not explicit in (4.1), but, from the source expressions used in NECBSC2, it can be seen that as $s^i \rightarrow 0$, then the incident illumination is infinite. (This is because the *free-space* radiation patterns for antenna models used in NECBSC2 code have a $\frac{1}{s^i}$ variation - which is used as incident field at the attachment point Q_1 on the cylinder's curved surface.)

As a rule of thumb, antennas are usually required to be 1λ away from the curved surface of the cylinder, while using NECBSC2 code [5]. (This is a serious limitation of the NECBSC2 code as applied to computations involving EMI coupling for antennas mounted on cylinders.) This fact implies that for fuselage-mounted antennas, modeling of EMI coupling, via NECBSC2 code cannot be done. Thus for such cases, use of NECBSC2 code warrants caution on the part of the user.

The transfer dyadic $\overline{\overline{\Gamma}}$ contains *Pekeris* functions $\hat{P}_{s,h}(\xi)$, and, the Fresnel integral $F(X^d)$. In the 'deep shadow' Pathak has shown that the contribution from the $F(X^d)$ vanishes. Thus, the creeping wave field in the deep shadow, $\phi = 150^0, 180^0$, given by (4.1), is primarily controlled by *Pekeris* function which in turn depend on ξ.

In the NECBSC2 code, coupling is computed from *two* creeping wave paths. (It is to be noted that AAPG uses only *one* ray in computing coupling.) At exactly $\phi = 180^0$, the two rays add in phase. For $\phi \neq 180^0$, this effect is seen in deep shadow regions as oscillations - due to inteference between two creeping wave paths.

4.2 Numerical results for replication of Harris NECBSC2 data

In this section, some selected results of the replication of Harris data are shown. This replication provides the basis on which Harris made the conclusions regarding the computational accuracies of the AAPG code in predicting EMI coupling between fuselage mounted antennas. It is shown that the replication was obtained by an alternate but equivalent proceedure to what Harris might have actually used. The details of this proceedure can be found in an earlier report [22]. Some of the selected results from that report are shown here. One cannot find in Harris report any details regarding the generation of the data. Therefore, it is necessary, to assess the validity of the Harris conclusions, to obtain the results as accurately as possible. The main steps involved in this process of replication are described briefly in the following paragraphs.

Execution of NECBSC2 code demands antennas to be located off the curved surface of the cylinder. This is due to the theoretical limitations contained in the formulations in the code. Consequently the exact numerical value at which the antennas were located off the cylinder in Harris calculations was necessary for replication of the data.

Harris had stated that to obtain isotropic coupling, an isotropic source was implemented into the NECBSC2 code because it does not contain any such source patterns. Therefore it is necessary to know exactly the modification Harris did to the

code to obtain the results shown in the report [10]. Since Harris did not provide any details regarding the modification, it became apparent that the technique should be such that NECBSC2 code remains *unchanged*, and, Harris NECBSC2 results could be replicated. This is a significant advantage, as modification to the code could lead to ambiguities in results.

As mentioned earlier, the NECBSC2 code computes Friis coupling. Since antenna gains must be contained within the Friis coupling data, so it became only necessary to subtract (in dB) the corresponding gain values taking into account the proper geodesic path trajectories between the source and receiver. Thus isotropic Friis coupling from the NECBSC2 code was obtained via the formula:

$$C_{iso} = C_{BSC} - G_t - G_r. \tag{4.2}$$

C_{BSC} is the output of the NECBSC2 code. $G_{t,r}$ are gain values along the path trajectories for the source/ receiver antenna patterns defined in the input datafile to the code. The details of this gain computation can be found in [22] and hence are not repeated here. To simplify the computations, $\frac{\lambda}{2}$ dipole sources were chosen. The gain computations become simple for these types of sources. For TE polarized coupling, which corresponds to axial slots on a cylinder, we chose axial magnetic dipoles. For TM polarized coupling, the dual, *i.e.*, electric sources were chosen. It must be noted that in the actual case, a TM polarized coupling occurs between circumferentially oriented slots on a cylinder. However, in the NECBSC2 code sources need to be located off the surface of the cylinder. Moreover since gains need to be removed, one can use any type of source corresponding to a particular

polarization, if the appropriate gain is subtracted. This allows us to use electric dipoles as being equivalent to circumferential slots from the polarization point of view; in the actual case, an electric source located tangentially *on* the surface of a perfectly conducting cylinder cannot radiate, since it is shorted. Use of axial sources also simplifies gain calculations, since the gains of axial electric or magnetic dipoles will then be numerically identical.

The height at which these sources were located were found by trial and error. It was found that h= 0.0375 m which is $\frac{\lambda}{4}$ at 2 GHz. This was the the distance that Harris had used for all the calculations. It must be noted that at higher frequencies, this distance is much larger than $\frac{\lambda}{4}$. All the results were replicated by this proceedure. Some of the selected data from [22] are shown here in Figs. 4.2 to 4.9.

The results shown in Figs. 4.2 to 4.9 for the EMC Lab computations were obtained via execution of the NECBSC2 code and use of Eqn. (4.2). In Eqn. (1.2), the antenna gains $G_{t,j}$ were computed in the manner that has been described in detail in [22, Appendix A.1].

It was necessary to format the output of the NECBSC2 code such that it can be used as input to the RPLOT (Rectangular PLOT) graphics program at the EMC laboratory. To this end, the BSCNFC (BSC Near Field and Coupling) program was written that can do this task. The BSCNFC is a user-friendly interactive program. The program requires the user to respond in accordance with the input datafile (GTDINP) to the NECBSC2 code. The output of the NECBSC2 code will then

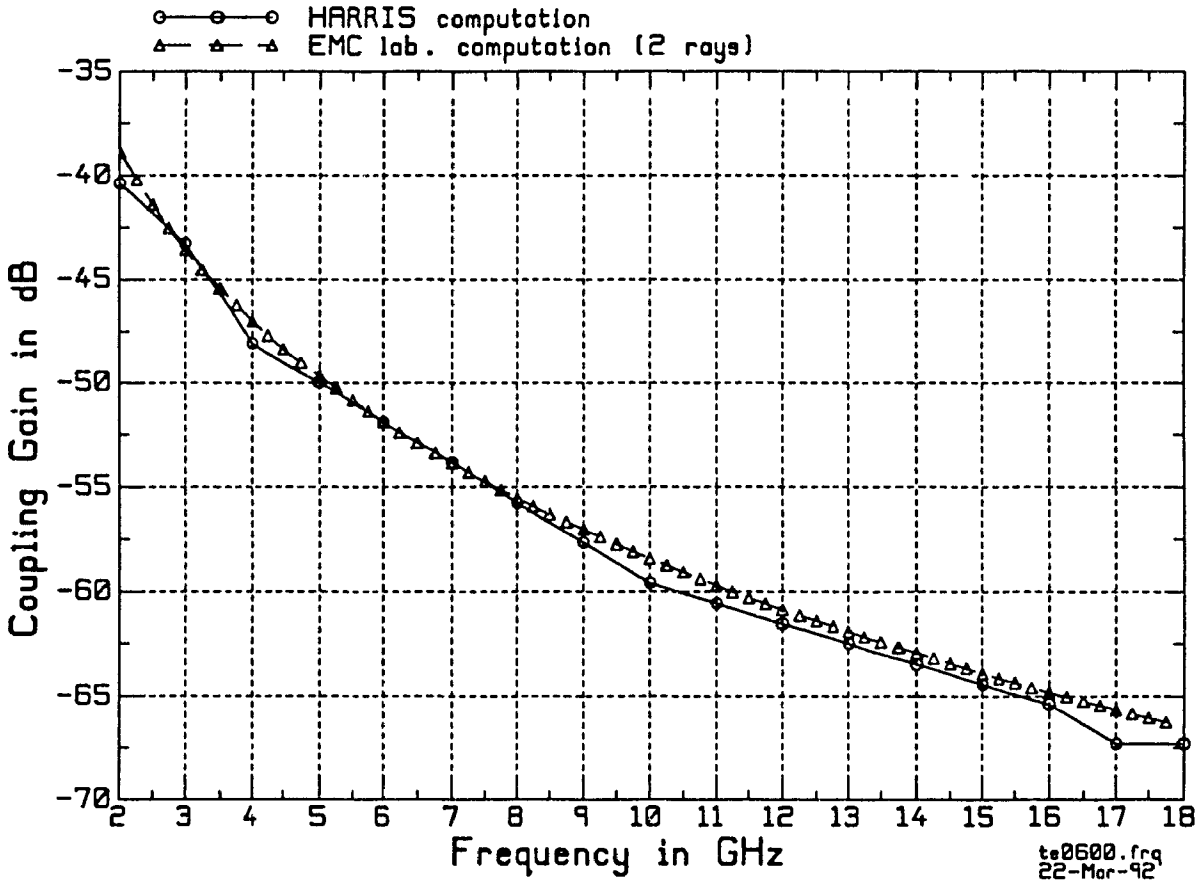

Fig. 4.2. Comparison of replication at $\phi = 60^0$,$Z_{offset} = 0''$,$a = 24''$,G_t =G_r = 2.15 dB, TE pol. h= 0.0375 m for EMC Lab results. Data refers to [10,p. 73].

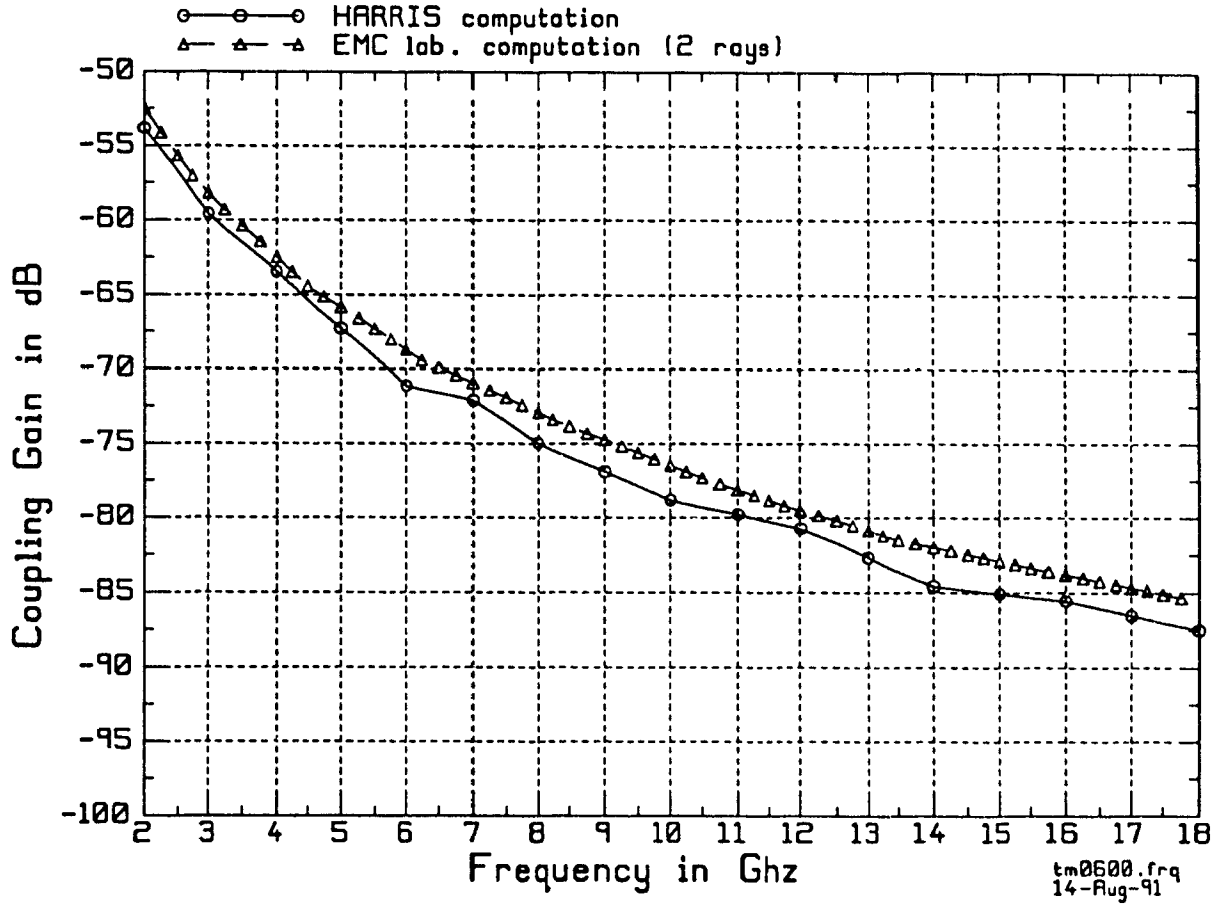

Fig. 4.3. Comparison of replication at $\phi = 60^0, Z_{offset} = 0''$, $a = 21''$, $G_t = G_r = 2.15$dB, TM pol. h= 0.0375 m for EMC Lab results. Data refers to [10,p. 73].

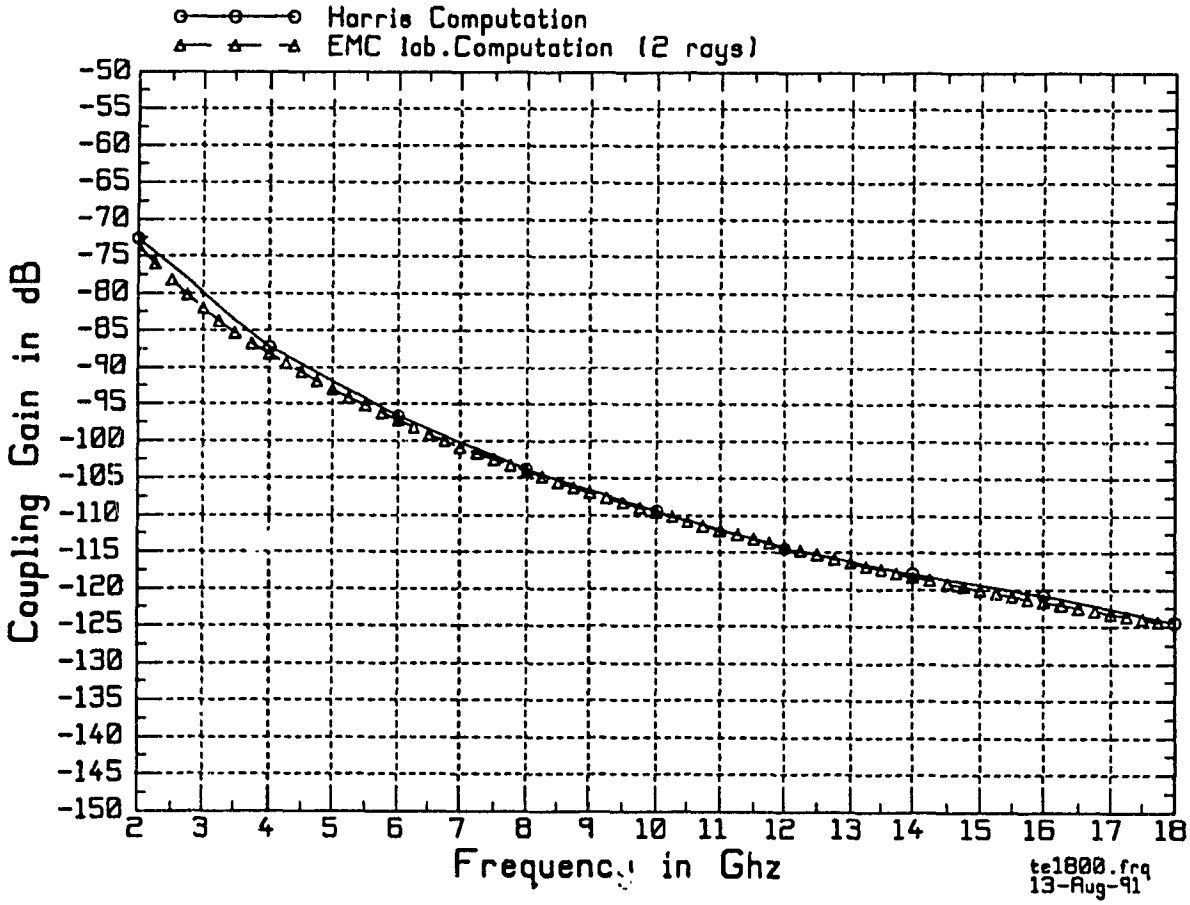

Fig. 4.4. Comparison of replication at $\phi = 180^0$,$Z_{offset} = 0''$,$a = 24''$,G_t =G_r = 2.15 dB, TE pol. h= 0.0375 m for EMC Lab results. Data refers to [10,p. 77].

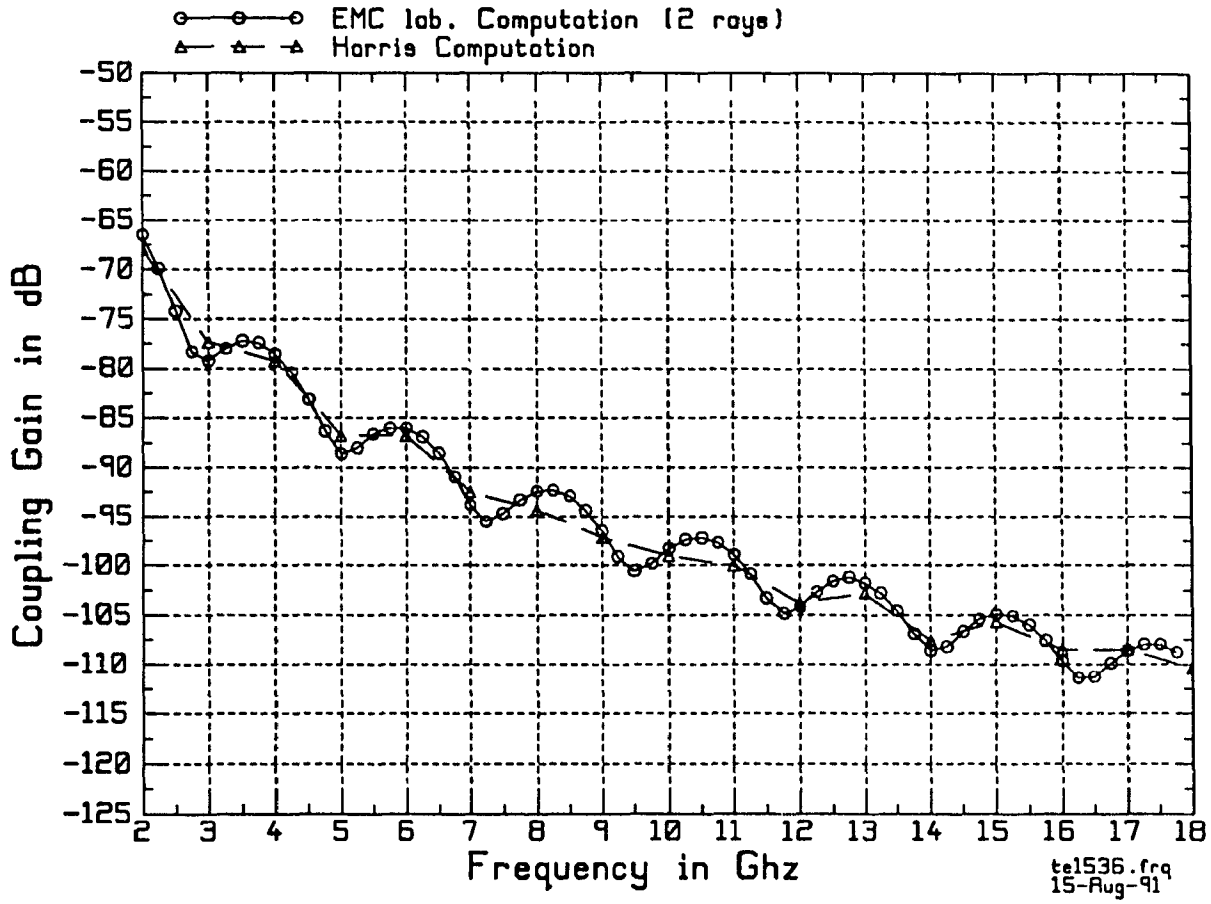

Fig. 4.5. Comparison of replication at $\phi = 150^0$,$Z_{offset} = 360''$,$a = 24''$,G_t =G_r = -15.09 dB, TE pol. h= 0.0375 m for EMC Lab results. Data refers to [10,p. 91].

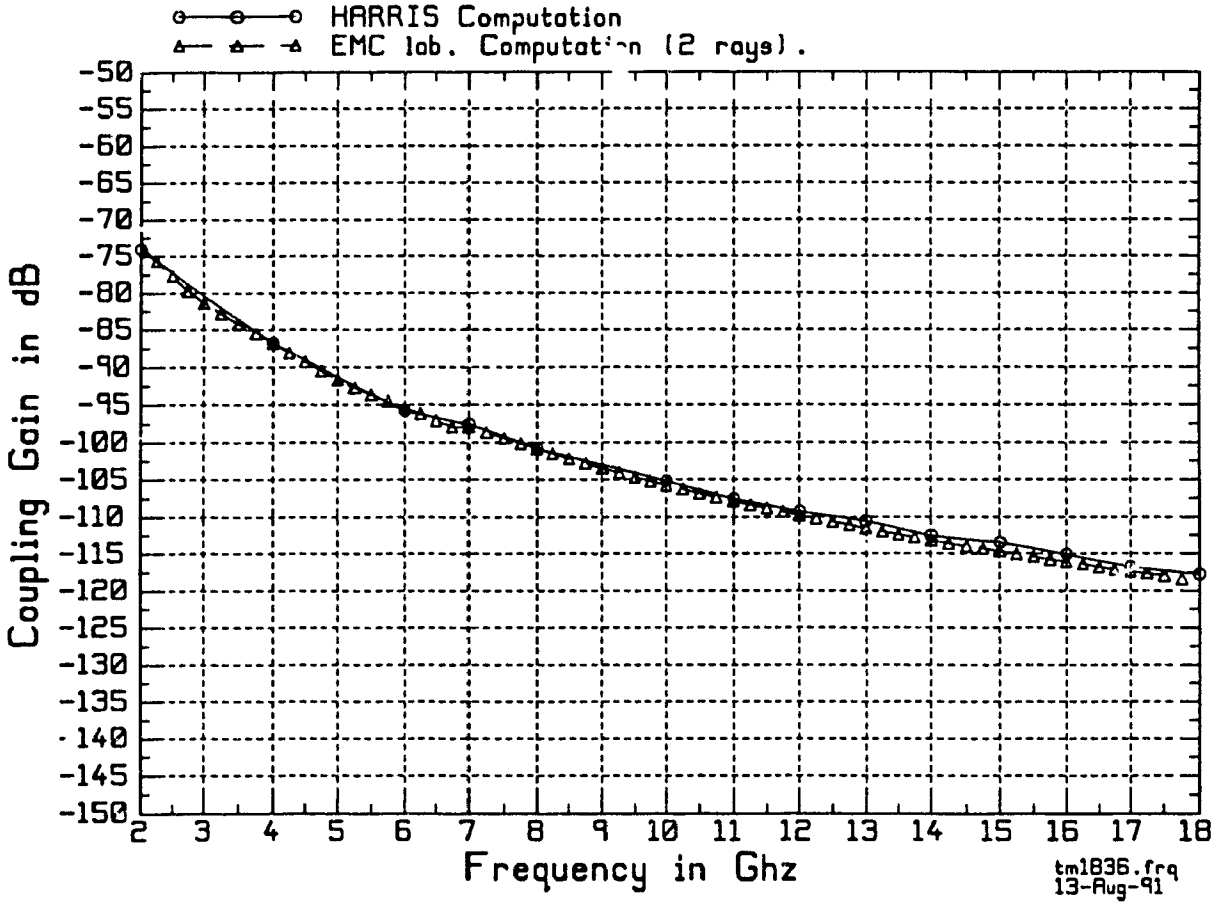

Fig. 4.6. Comparison of replication at $\phi = 180^0$,$Z_{offset} = 360''$,$a = 24''$,G_t =G_r = −13.55 dB, TM pol. h.= 0.0375 m for EMC Lab results. Data refers to [10,p. 92].

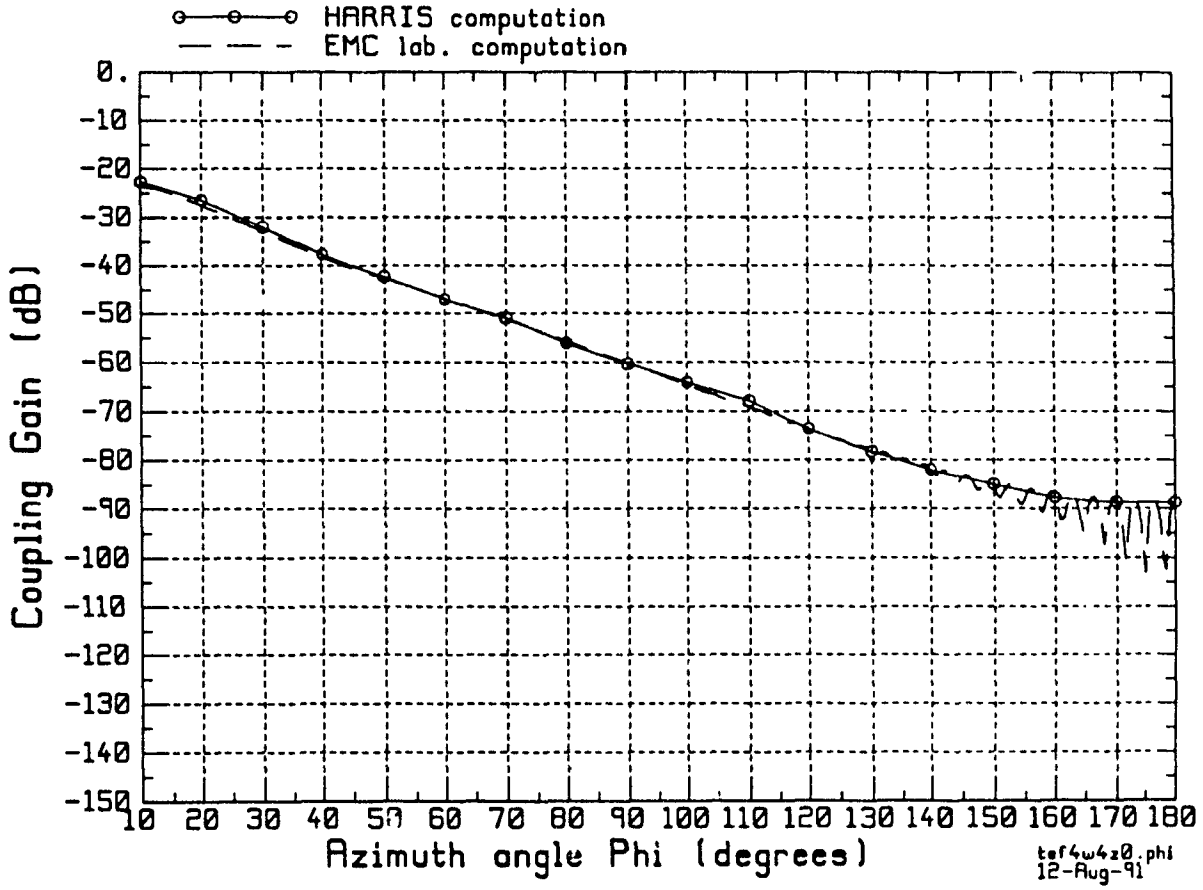

Fig. 4.7. Comparison of replication at f= 4 GHz, $Z_{offset} = 0''$, $a = 24''$, $G_t = G_r =$ 2.15 dB, TE pol. h= 0.0375 m for EMC Lab results. Data refers to [10,p. 57].

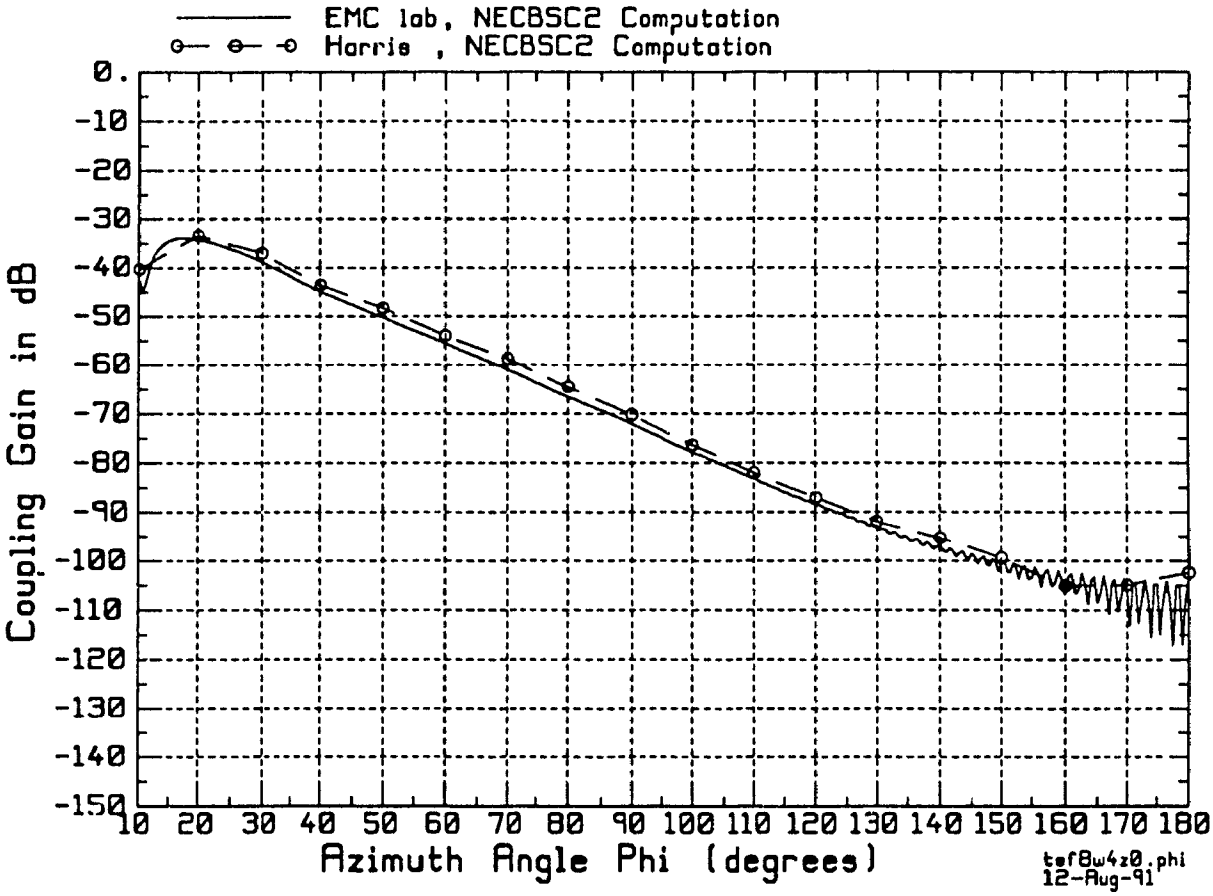

Fig. 4.8. Comparison of replication at f= 8 GHz,$Z_{offset} = 0''$, $a = 24''$, G_t =G_r = 2.15 dB, TE pol. h= 0.0375 m for EMC Lab results. Data refers to [10,p. 58].

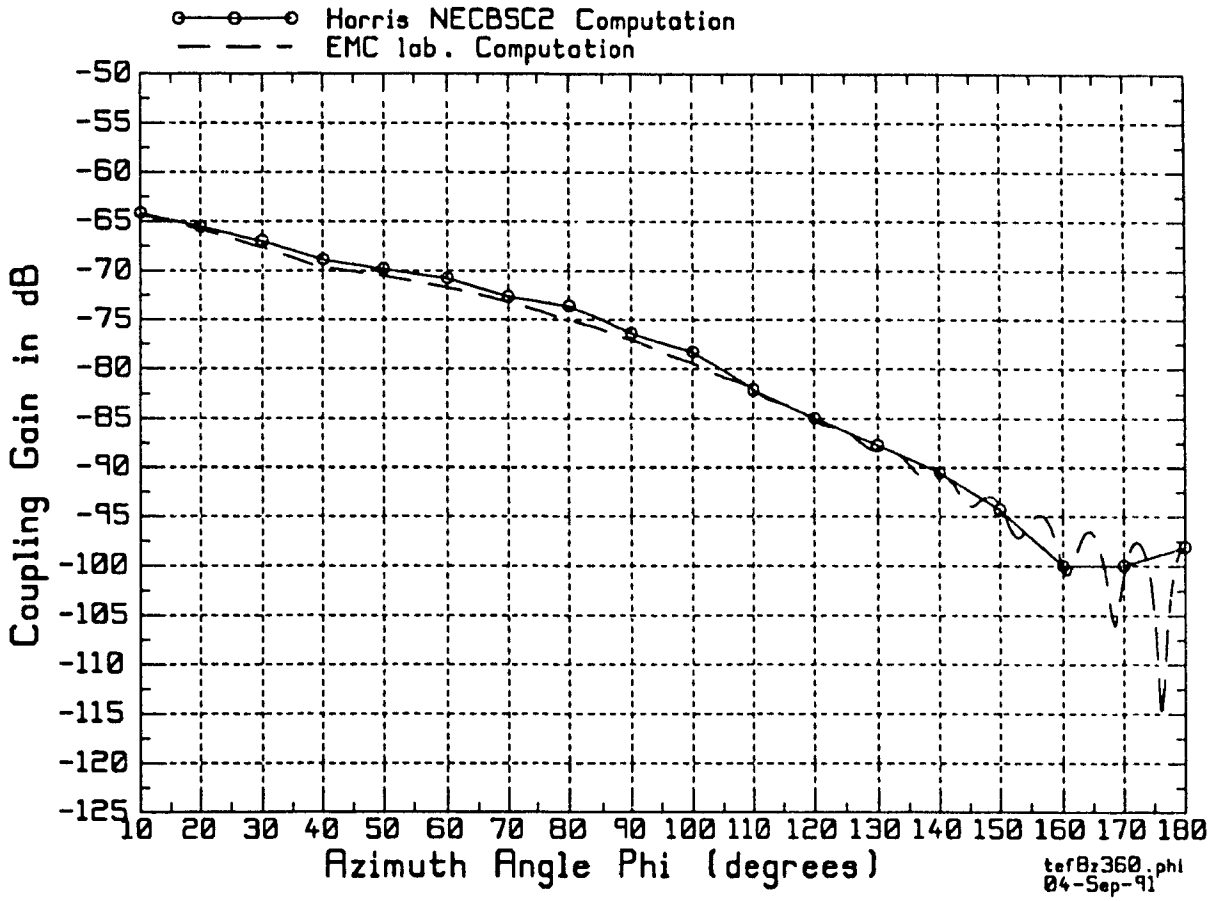

Fig. 4.9. Comparison of replication at f= 8GHz,Z_{offset} = 360″,a = 24″ and G_t =G_r = 2.14 dB, TE pol. h= 0.0375 m for EMC Lab results. For the EMC Lab runs, radial, $\frac{\lambda}{2}$ electric dipoles were used. Data refers to [10,p. 70]

be read by the BSCNFC program. Since there could be a wide variety of styles in preparing an input datafile, the BSCNFC requires the user to write an input datafile in a particular format. Thus, while responding interactively to the BSCNFC program, if the user has not followed the specific style, the code will will abort the execution asking the user to prepare the input to NECBSC2 code in the specific format. At present, the BSCNFC program prepares output datafiles for coupling and $20\times \mathrm{Log}_{10}|\vec{\mathbf{E}}_{total}|$ vs. frequency, or, any other coordinate (geometry) variable. Multiple data can also be handled by the BSCNFC program, if each typical data is separated from the other by the NX card.

Next, to use (4.2), the output of the BSCNFC program (which is C_{BSC}) needs to be modified by subtracting the gains. To accomplish this effectively, the program CONV was written - that asks the user to specify the gain values. It is important to note that only a single set of input data for gains can be entered. The CONV program will then read each line of the output from the BSCNFC code, and rewrite the same file by computing C_{iso} according to Eqn. (4.2).

Thus, by using BSCNFC and CONV, the isotropic coupling can readily be displayed against frequency or any relevant geometry variable. If the user wishes to display the exact output of the NECBSC2 code, then use of CONV is not necessary. The CONV is not a general purpose program. It was designed only for the purposes of replicating Harris data.

In Figs. 4.2 to 4.9, the source gains are shown. Harris data shown in here was digitized directly from the report [10]. This process was very laborious because

Harris results are on a 0 to -200 dB scale at an interval of 50 dB. To avoid any discrepancies, due to visual errors, each data had to be checked many times. All the digitized results are believed to be correct within 1 dB.

Fig. 4.2 shows isotropic TE coupling at $\varphi = 60^0$. One notices excellent agreement.

Fig. 4.3 shows isotropic TM coupling for the same data. There is a difference of 2 dB. This difference contains a digitization error of 1 dB. The remaining difference is numerically insigificant for all practical purposes and is not discussed further.

Fig. 4.4 shows replication at $\varphi = 180^0$. There is an excellent agreement. (The result of this figure is further discussed in conjunction with Fig. 4.6.)

Fig. 4.5 shows the result for $\varphi = 150^0$, $Z_{offset} = 360''$. One can observe oscillatory behavior in our (EMC Lab) data. This oscillatory nature is absent in Figs. 4.2,3,4. Harris data agrees with ours at specific data points. The figure also shows that our results have a much greater degree of smoothness - which implies that Harris computed at fewer number of datapoints.

It is somewhat surprising that the two results shown in Fig. 4.5 will agree very closely. For the EMC Lab data in Fig. 4.5, the NECBSC2 code was executed using axial, $\frac{\lambda}{2}$, magnetic dipoles corresponding to TE case. At $Z_{offset} = 360''$ and $\varphi = 150^0$, it has been shown in [22] that for axially oriented sources, antenna gains will be different for the clockwise and anticlockwise paths respectively. Harris had modified the NECBSC2 code - which means that for any position of the source and receiver the directive path gains will be unity (isotropic source). This difference in

path gains using axial sources was expected to show up in our results. Consequently one can conclude that our method is remarkably accurate - by judging the close agreement in the two results.

Comparing Figs. 4.2,3.4 and 4.5 one notices oscillatory behavior at $\phi = 150^0$, *i.e.*, Fig. 4.5. NECBSC2 code always considers two creeping rays for observer positions in the deep-shadow. In Figs. 4.2 and 4.3, for $\phi = 60^0$, the total coupling is dominated by field from the dominant path. The field on the other path is extremely small due to the exponential decay. This shows up as a monotonic decrease in coupling with frequency. In Fig. 4.4, at $\phi = 180^0$, the two creeping rays have the equal magnitudes and they meet in phase. This causes no interference, and, the decay in coupling is seen to be monotonic with frequency in Fig. 4.4. In Fig. 4.5, we notice strong oscillatory behavior in coupling gain. At this angle, *i.e.*, $\phi = 150^0$ and for axial offset of 360", the rays have *nearly equal* field strengths. When the frequency or wavenumber changes, the electrical length of the two paths change. Since these two paths are unequal in length at $\phi = 150^0$, the phase along the two paths change causing interference (nulls) and reinforcement (peaks) in the coupling gain variation. The approximate difference between the peaks and nulls shown in Fig. 4.5 is around 10 dB.

Fig. 4.6 shows the result at $\phi = 180^0$. In this case $Z_{offset} = 360"$ and TM polarized sources were used. For TM polarized sources the EMC Lab data was obtained using axial, $\frac{\lambda}{2}$, electric sources. It is clear from the data in Fig. 4.6 that both the results are in excellent agreement. Unlike the data in Fig.4.5, one notices

absence of oscillations because at this angle the two creeping rays are equal in length and the fields are equal in magnitude. As has been explained in connection with Fig. 4.4, these two rays always meet in phase and thus no nulls appear.

Figs. 4.7 to 4.9 show some selected data for the C vs. ϕ cases reported extensively in [22]. For the data in Figs. 4.7, 4.8 axial.$\frac{\lambda}{2}$, magnetic dipoles were used. For the result in Fig. 4.9, radial electric dipole sources were used. The EMC Lab data in Figs. 4.7 to 4.9 was computed at 311 datapoints. The cases are discussed below.

Since Figs. 4.7 and 4.8 are geometrically the same, except for a change in the frequency, the two are discussed together. In both these figures one notices oscillatory behavior in coupling begining around $\phi \simeq 130^0$. This oscillatory behavior is reminiscent of the phase interference between the two paths as the receiver moves with ϕ. At some angles there is cancellation, while at other values of ϕ there is reinforcement. One also notices that from $10^0 \leq \phi \leq 130^0$ the change in coupling is linear with ϕ. This is due to the fact that the coupling in these regions is dominated by the field on the shorter creeping ray path.

One also notices that in both these figures, in the deep shadow, *i. e.* where the oscillations are seen, Harris data is *top-of-the-envelope* of our data. This indicates that Harris computed at fewer datapoints. Our results have considerable degree of smoothness over Harris data. One can conclude from the very good agreement between the two results that our method is almost identical to what Harris might have actually used.

Fig. 4.9 shows the TE result at $Z_{offset} = 360''$. Again, very good agreement

is seen between the two results. To replicate Harris data we used radial sources, because as explained in [22], this gives equal gains over both the creeping ray paths as the observer moves in ϕ. We see that such a choice of sources gives very good agreement between the two results.

In all the Figs. 4.7 to 4.9, at $\phi = 180^0$ the total coupling is 6 dB more than that due to a single ray.

The selected results of this replication, as shown in Figs. 4.2 to 4.9, reveal that our method is remarkably accurate. The numerical value of the height, *i.e.* h= 0.0375 m, that Harris used in the NECBSC2 and AAPG code comparisons, is an important parameter that will be analysed in more detail in Chapter 6. For further assessment of the NECBSC2 code's coupling predictions, several coupling models are compared against the experimental data from Harris report, and, are shown in the next section.

4.3 Numerical results for comparison of different coupling models

In this section, comparison between numerical and experimental results are presented. The numerical data refers to NECBSC2, U, V formulation, and AAPG code results. The measured data was obtained from Harris report. The measured data in Harris report refers only to C vs. f cases. The results for this section are shown in Figs. 4.10 to 4.13.

The measured data refers to a cylinder of radius of 22.92". The angles are $\phi = 60^0, 150^0$ and $Z_{offset} = 0", 96"$. These two angles refer to small and large coupling paths, and, with and without torsion. Since these cases encompass the most general geometry of coupling paths on circular cylinders, our choice appears to be adequate for the purposes of comparisons. The measured and AAPG data were directly digitized from Harris report. The NECBSC2 results were obtained via the replication process described in Section 4.2. Digitization of measured data had to be done with much care because of the rapid degree of oscillations. Furthermore, NECBSC2 data refers to sources kept at h= 0.0375 m from the cylinder surface. The AAPG and U, V data refer to antenna locations on the cylinder surface (h= 0 m).

Fig. 4.10 show the comparison at $\phi = 60^0$. The agreement between AAPG, U, V formulation and measured data is very good. One can easily conclude that the measured data at this angle can adequately be approximated by the single ray coupling from AAPG code. The NECBSC2 code shows increased divergence with frequency when compared with the other three results.

Fig. 4.11 show similar results for $Z_{offset} = 96"$. All other parameters remain fixed as in Fig. 4.10. The measured data agrees reasonably well with the AAPG and U, V formulation results. The NECBSC2 results, as in Fig. 4.10, diverges from the other three model predictions.

Fig. 4.12 shows the comparison at $\phi = 150^0$ and for torsionless Z_{offset} paths. It is seen that AAPG and U, V coupling data agree very well; however the measured data

does not agree with these two models. This is most likely, because, the measurements in this case are most probably inaccurate as explained in [10, pp. 157 - 182]. The NECBSC'2 data diverges from the other two, *i.e.*, (AAPG and U, V formulation) computed data.

Fig. 4.13 depicts the comparisons at $\phi = 150^0$ and $Z_{offset} = 96''$. For this torsional coupling path, the AAPG and U, V data are seen to be in good agreement. The NECBSC'2 data diverges with the other three models.

In the next section, the summary of the results from this, and, Chapter 3 is presented, along with an evaluation of Harris model comparisons.

4.4 Analysis of the model comparisons made by Harris Corporation

Harris conclusions, based on comparisons of results from AAPG and NECBSC'2 codes can now be dismissed as inaccurate. Unfortunately, the results of Genello and Pesta could not be verified. Thus, their comments regarding cannot be evaluated.

Canonical model measurements and computations had been made by Harris. The replication of the results showed that, though the report was vague in nature, the numerical values of the results are correct. Upon comparing the AAPG and U, V formulation results, it was observed that there exists no modeling inaccuracies in the present AAPG code. In Sec. 4.3 the NECBSC'2, AAPG, U, V formulations and measured data have been compared. Reasonably good agreement between AAPG,

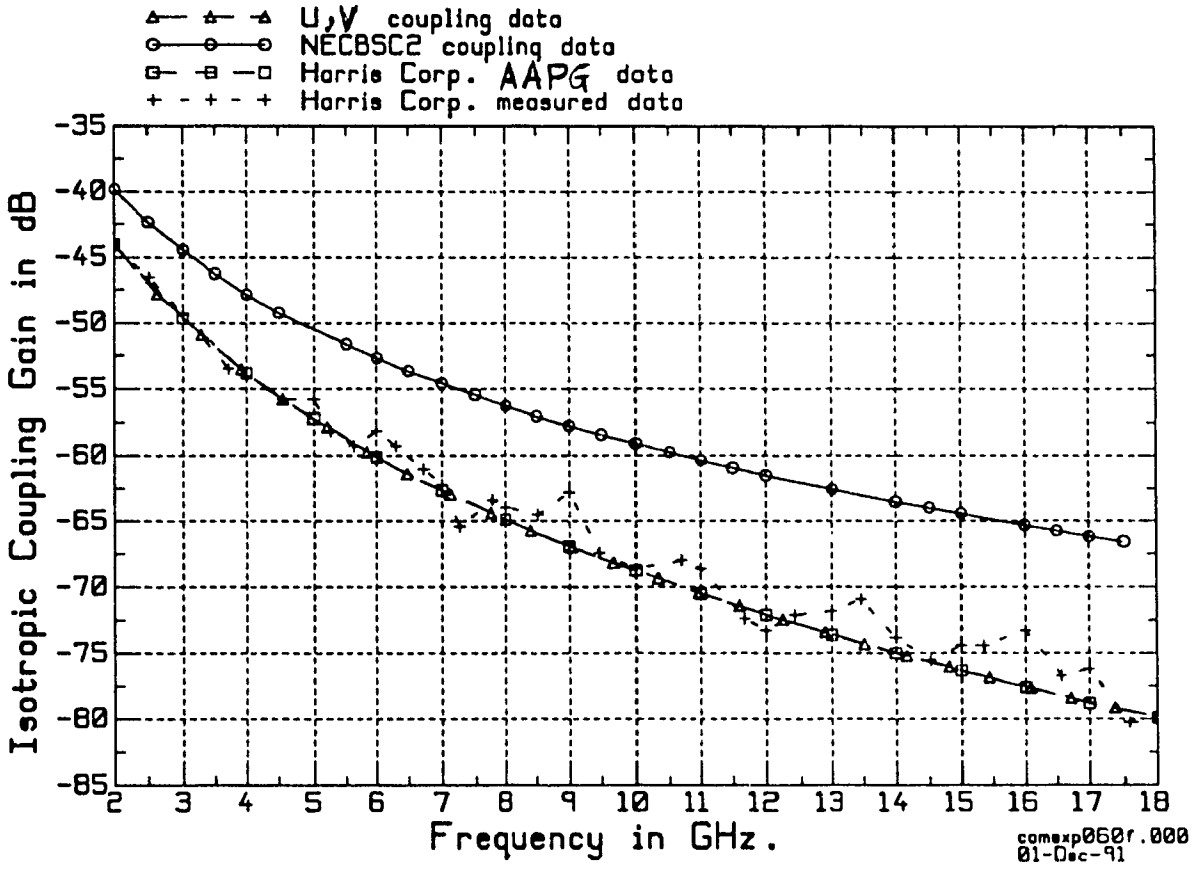

Fig. 4.10. Measured and computed results for: $a = 22.92'', \phi = 60^0, Z_{offset} = 0''$. The NECBSC2 data was obtained by keeping the sources at h= 0.0375 m. For the NECBSC2 runs, G_t =G_r = 4.38 dB was subtracted from the actual code output to get isotropic coupling. The experimental and AAPG data has been digitized from [10,p. 170 and 259] respectively. The U,V result shown here was obtained by keeping sources at h= 0 m on the cylinder surface.

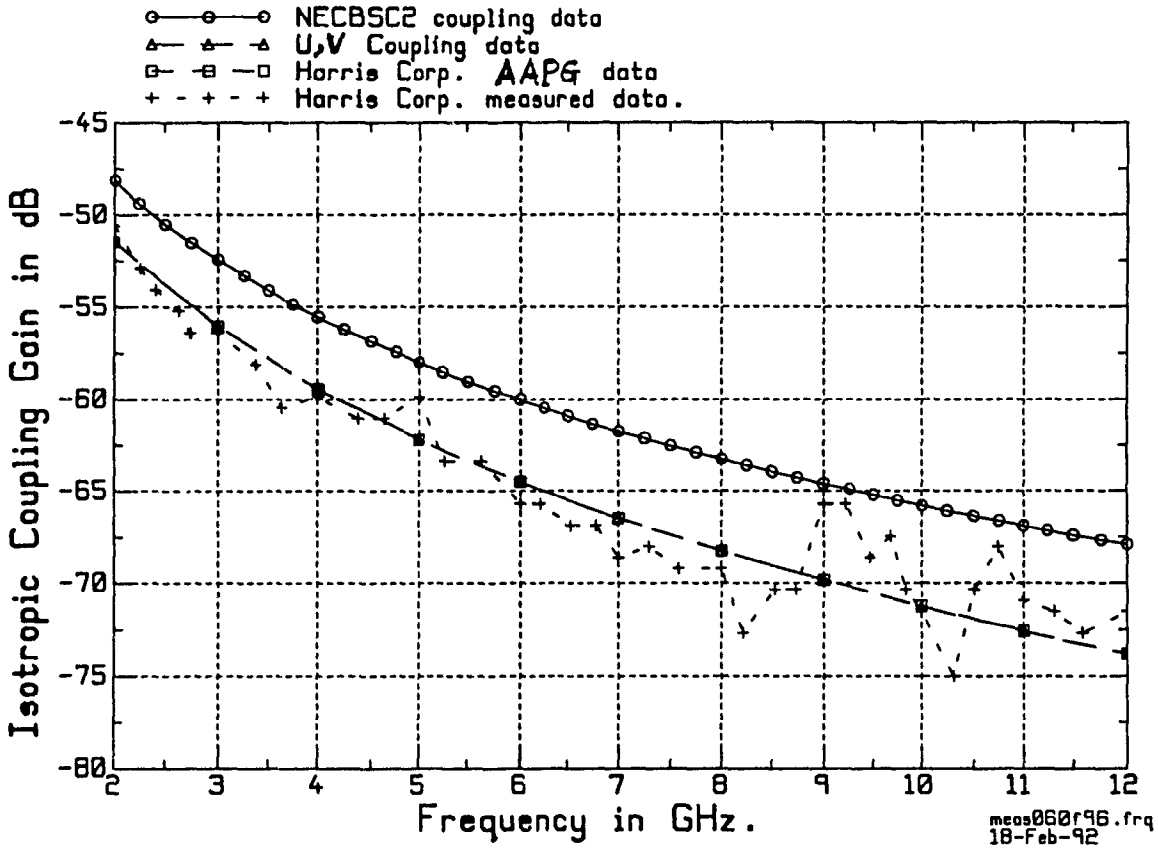

Fig. 4.11. Measured and computed results for: $a = 22.92'', \phi = 60^0, Z_{offset} = 96''$. The NECBSC2 data was obtained by keeping the sources at h= 0.0375 m. For the NECBSC2 runs, $G_t = G_r = 5.13$ dB was subtracted from the actual code output to get isotropic coupling. The experimental and AAPG data has been digitized from [10,p. 177 and 266] respectively. The U, V data was computed for h= 0 m. Experimental data in [10] for this case is not available beyond 12 GHz.

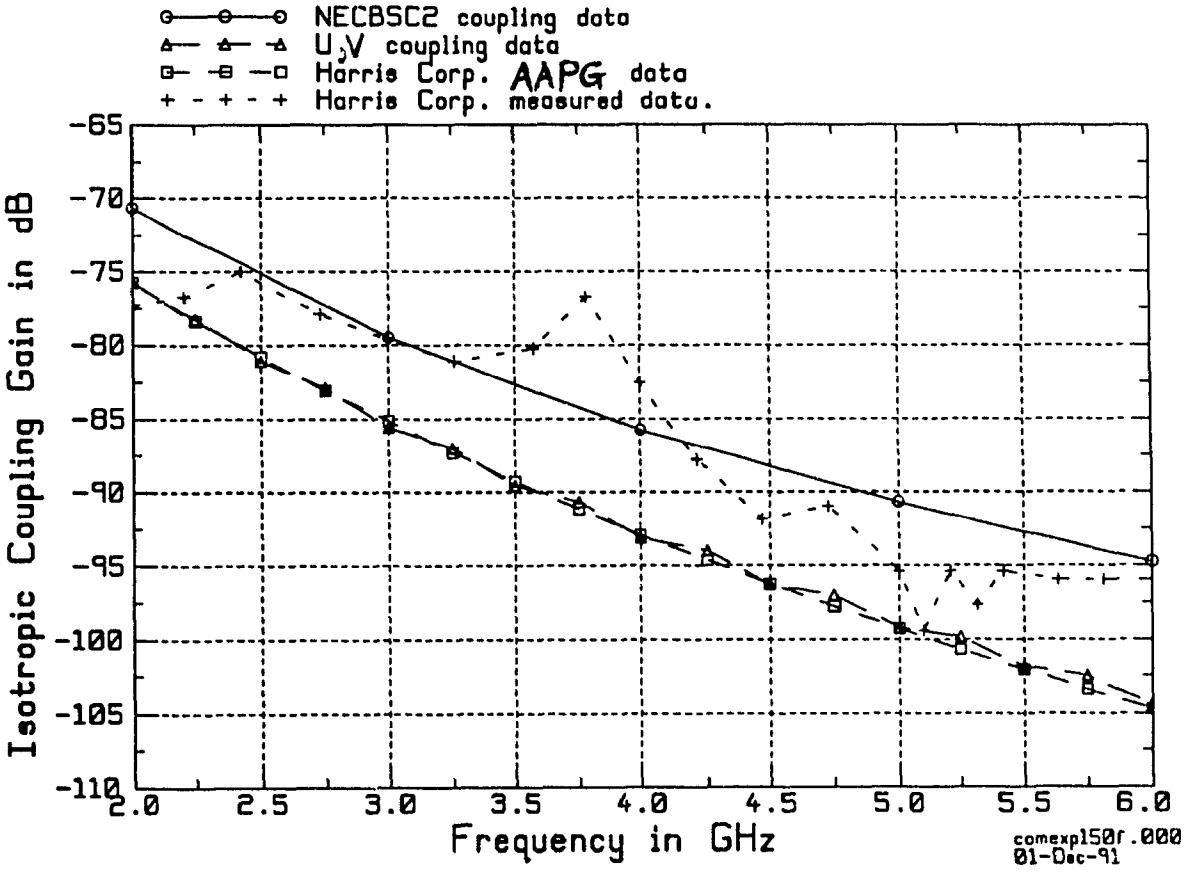

Fig. 4.12. Measured and computed results for: $a = 22.92''$, $\phi = 150^0$, $Z_{offset} = 0''$. The experimental and AAPG data has been digitized from [10, p. 173 and 262] respectively. The experimental data in [10] for this case is inaccurate beyond 6 GHz. $G_t = G_r = 4.38$ dB were the gains of the sources used here.

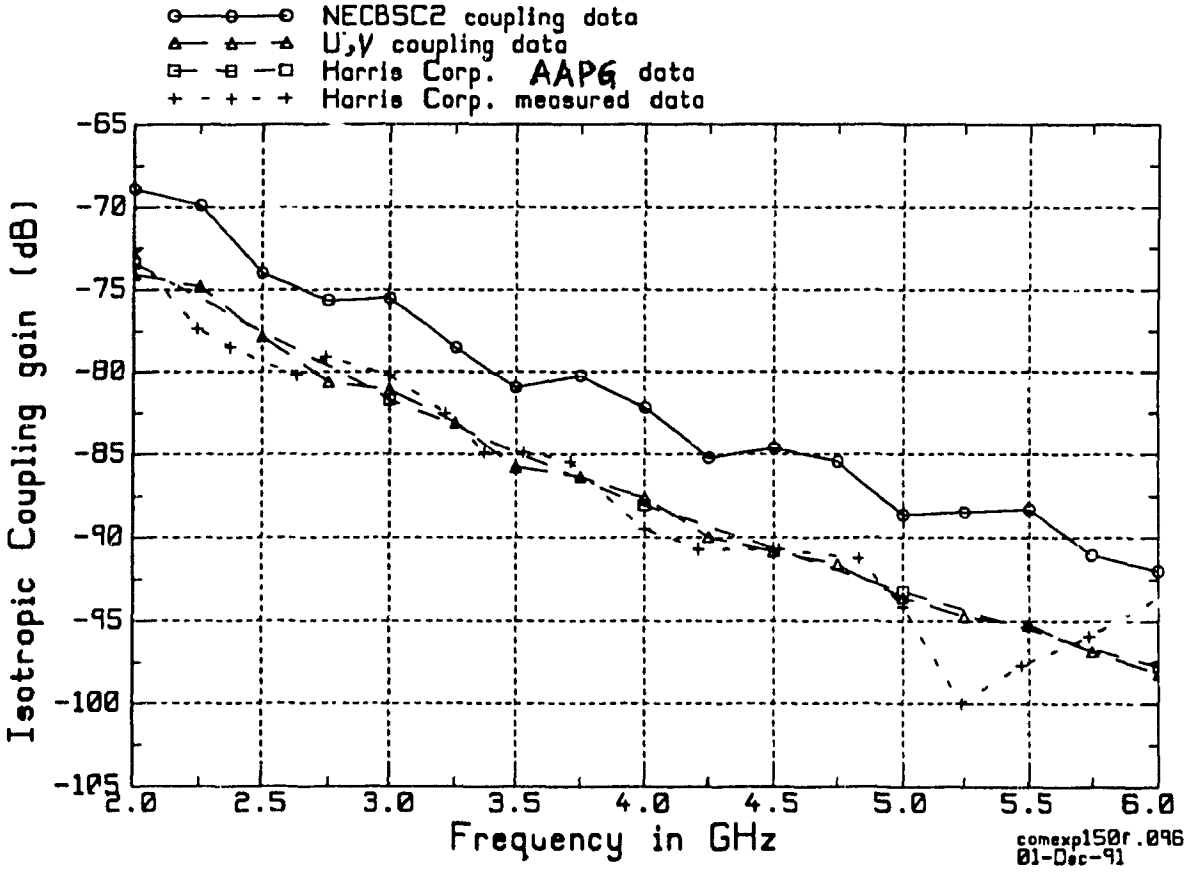

Fig. 4.13. Measured and computed results for: $a = 22.92''$, $\phi = 150^0$, $Z_{offset} = 96''$. The experimental and AAPG data has been digitized from [10, p. 180 and 269] respectively. The experimental data in [10] for this case is inaccurate beyond 6 GHz. $G_t = G_r = 4.95$ dB were the gains used.

U, V formulations and measurements revealed that AAPG code is indeed accurate for all the test cases considered by Harris. In these cases, it was found that NECBSC2 data did not agree with the other three model predictions. This allows one to conclude that NECBSC2 cannot model on-surface coupling. Therefore Harris conclusions are inappropriate because data from two *mutually exclusive* formulations was compared, and, thus *non-physical* conclusions were reached.

This mutual exclusivity is studied in detail in Chapters 5 and 6.

Chapter 5

Evaluation of the existing AAPG code surface shading loss formulation

In this chapter, the shading loss formulation, as used in the AAPG code is reviewed in detail in Section 5.1. Comparison of the shading loss with the $V_0(\xi)$ function is presented in Sec 5.2. In Sec. 5.3 the validity of the AAPG calculations for off-surface cases is analysed in detail. Section 5.4 summarizes the results of this chapter.

5.1 The Friis coupling formula and the shading loss in the AAPG code.

An alternative method in computing coupling gain between antennas mounted on cylinder is to use the formula as in the AAPG code. This is the coupling over a *single*, *dominant* path, and reads:

$$C_{dominant} = \left(\frac{\lambda}{4\pi L}\right)^2 G_t G_r L_{cs} \tag{5.1}$$

The expression for L_{cs} will be defined later. The above is a much more convenient way in computing coupling as compared to the NECBSC2 code. L_{cs} is the effect of a structure on which the antennas may be mounted or located in proximity. For example, when antennas are radiating in free-space there is no structure (scatterer) and hence, $L_{cs} = 1.0 = (0$ dB). However, when antennas are radiating in presence of a flat infinite ground plane, the transmitting antenna gain is increased by 6 dB, and, the coupling increases by 6 dB. (The receiver gain remains same as that of its free-space value.) In the antenna-to-antenna coupling calculations on a cylinder, the L_{cs} is an effect of the creeping wave attenuation depending on the geodesic radii of curvature. Of particular interest is the case where $ka \to \infty$ or the high frequency effect. This limiting case, can be realized by allowing the radius of the cylinder to become very large and hence the coupling on a cylinder will approach that on a large conducting ground plane - when the observer is not very far away, implying that curvature is small. Therefore, the maximum value of the L_{cs} in case of 'very large' cylinders is 6 dB. As the radius of the cylinder, or, the wavenumber k increases,

the creeping wave attenuation increases; consequently in case of extremely high attenuation, the limiting value is set to -200 dB. For fuselage-mounted antennas, the geometry that is considered by the AAPG code is shown in Fig. 5.1.

The importance of L_{cs} is because that it allows one to compute the effects of the structure in a simple and accurate fashion. The calculation of coupling gain for the same problem is not involved like the NECBSC2 code. For example, if one wishes to find the effects of antennas located before a ground plane, then L_{cs} may well represent the reflection effects from the ground plane. In case of large circular cylinders representing fuselages, L_{cs} is the attenuation of the creeping wave which is known as 'surface shading'. This is the creeping wave loss over the relevant geodesic path in question. In this case, *i.e.*, in a AAPG computation, antennas can be mounted both '*off*' or '*on*' the surface. Harris had reported for the 'on' case. This simple formula is the main advantage of the code in calculating EMI margins.

The L_{cs} in Eqn. (5.1) is given by [6]:

$$L_{cs} = \frac{-A}{\eta A + \mu}. \tag{5.2}$$

where,

$$\eta = \begin{cases} 0.005478, & \text{for } A < 26.0; \\ 0.003310, & \text{for } A \geq 26.0. \end{cases} \tag{5.3,4}$$

and,

$$\mu = \begin{cases} 0.5083, & \text{for } A < 26.0; \\ 0.5621, & \text{for } A \geq 26.0. \end{cases} \tag{5.5,6}$$

In (5.3 to 6), the quantity A is again expressed in terms of the Fock parameter ξ that reads:

$$A = \sqrt{2.0}\xi^{\frac{3}{2}} \tag{5.7}$$

with the Fock parameter ξ defined as in (3.6). Comparing Eqns. (3.15) and (5.1), one can immediately conclude that for on-surface locations $L_{cs}(\xi) = 20 \times \mathrm{Log}_{10}|V_0(\xi)|$. Therefore Eqns. (5.2) to (5.6) serve as an approximation to the Fock function $V_0(\xi)$. (This approximation has been thoroughly evaluated in the next section.)

Following the brief, qualitative description of the UTD scattering formulation of creeping waves as Ch. 4, and, the surface shading loss formula as in (5.2), one can observe that in *both* the cases, the Fock parameter ξ plays an important role. As shown in (3.6), this term contains all the *electrical*, and, *geometrical* information about the coupling path between a pair of fuselage mounted antennas. ξ *does not* yield *directly* the loss, or, coupling. However, the curved surface loss, in the two formulations depends on different functions, which in turn, depend *solely* on ξ. Hence ξ or equivalently the *frequency* and the *geometry of the coupling path* dictates the creeping wave loss between a pair of fuselage mounted antennas.

The AAPG code can also compute antenna to antenna coupling when the sources are located off the surface. The geometry for this is shown in Figs. 1.1 to 1.2 and also in Figs. 3.1, 3.2. The antenna locations are now S and R. The AAPG code computes the total distance R between S and R. This now *includes* the geodesic portion as shown by Q_1 and Q_2, and, the straight portions SQ_1 and Q_2R. (See Fig. 3.1). To find the curved surface loss, the Fock parameter ξ is computed over the path Q_1Q_2.

The AAPG code continues to compute coupling off the cylinder surface by using (5.1). Referring to Fig. 3.1, the total distance $L = SQ_1 + Q_1Q_2 + Q_2R = s_l + t + s_d$.

However, the L_{cs}, which is the $V_0(\xi)$ function, is now computed for the intercepted portion Q_1Q_2 shown in Fig. 3.1. The free- space spreading loss (TFS) is now computed over this distance L. As shown in Section 5.3, this method yields incorrect yet safe answers for off surface cases when compared to the NECBSC2 code.

5.2 Limitations of the AAPG code for on surface calculations

In this section numerical results, shown in Figs. 5.1 to 5.3, are presented to understand the limitations of the AAPG codes calculations when applied to the on surface coupling gain predictions. This validation is important, because, there is no documentation in published literature regarding the derivation of L_{cs} used in the current AAPG code. In fact, the well-known document of Widmer [6], does not show how this form, *i.e.*, Eqn. (5.3) came to be used. Rather than depending on results that could be incorrect, it is important to have a thorough evaluation of the AAPG code as far as applications to fuselage- mounted antennas are concerned. It is important to note that Eqn. (5.2) is also used in the latest version of the AAPG code, *i.e.*, [19]. There additional terms, that account for the generally non-circular cross-sections, are also computed and added to the term in Eqn. (5.2). For generally convex surfaces, the Fock parameter ξ is given by a more general form than the one in (3.6). So, it is important to have an idea regarding the accuracy of the L_{cs} term. To this end, since the dominant term approximation from the general Pathak and

Wang formulations was used, it is only necessary to compare the shading loss $L_{cs}(\xi)$ given in Eqn. (5.2) and $20\times\text{Log}_{10}|V_0(\xi)|$, the hard surface Fock function.

The results of Figs. 5.1, 5.2 show the deficiency of L_{cs}. It is apparent that beyond $\xi \geq 15.0$, L_{cs} is a *poor* approximation to the $V_0(\xi)$. Since ξ contains all the information about coupling paths on which surface rays propagate, the result in Fig 5.1 indicate that for some combination of geometrical and electrical parameters, the AAPG code will falsely predict *more* EMI than that would actually be present. In other words, the use of (5.2) beyond $\xi \geq 15.0$ predicts less creeping wave attenuation over the geodesic path. For smaller values of ξ, as seen in Fig. 5.2, one can see that the approximation is excellent. To illustrate the use of Figs. 5.1,5.2, the reader is referred to Fig. 5.3 which is a typical example for our case.

The result of Fig. 5.3 shows that beyond f= 17 GHz, the AAPG code predicts more coupling. The AAPG data in Fig. 5.3 was obtained from the computer program that was developed based on Eqns. (5.1) to (5.7). (The validation of the program against exact AAPG version 07 results is done in the next section.) The geometrical data for the AAPG results in Fig. 5.3 is the same as used by Harris to generate the AAPG results shown in Fig. 2.2. The only difference is that the frequency is switched upto 28 GHz begining from 12 GHz in Fig. 5.3. (The frequency switch in Fig. 2.2 is from 2 to 18 GHz.) One can easily find out via (3.6) that $\xi = 15.0$ at the frequency f= 17 GHz. The increased prediction from the AAPG code beyond 17 GHz is due to the differences in the L_{cs} and $V_0(\xi)$ that is shown in Fig. 5.1.

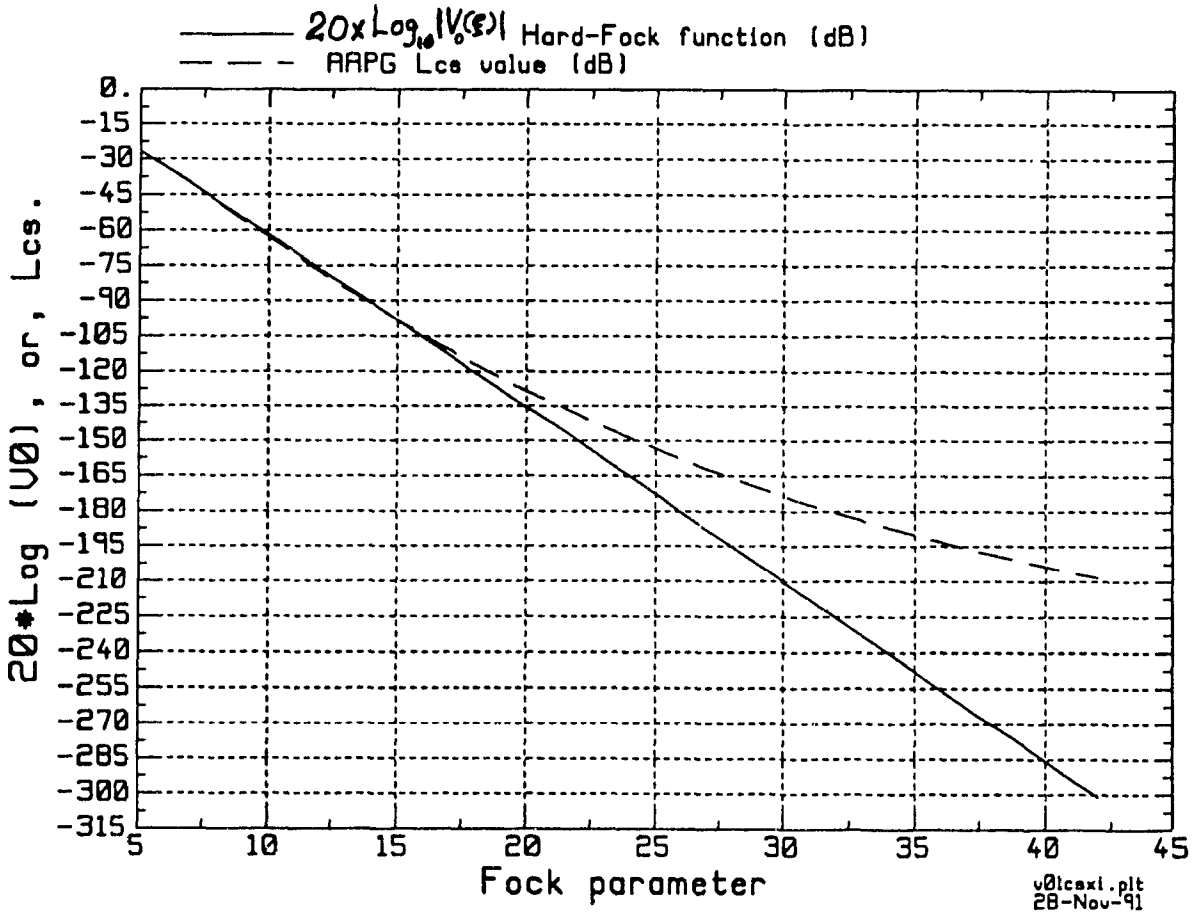

Fig. 5.1. Plot of $L_{cs}(\xi)$ and $20\times \mathrm{Log}_{10}|V_0(\xi)|$ vs the Fock parameter ξ. The result implies that upto $\xi = 15.0$ single ray data from U, V formulation to $O(kt)$ term, and, AAPG code is expected to give the same result. Beyond $\xi > 15.0$ the approximation to $V_0(\xi)$ surface Fock function is inaccurate in the AAPG code.

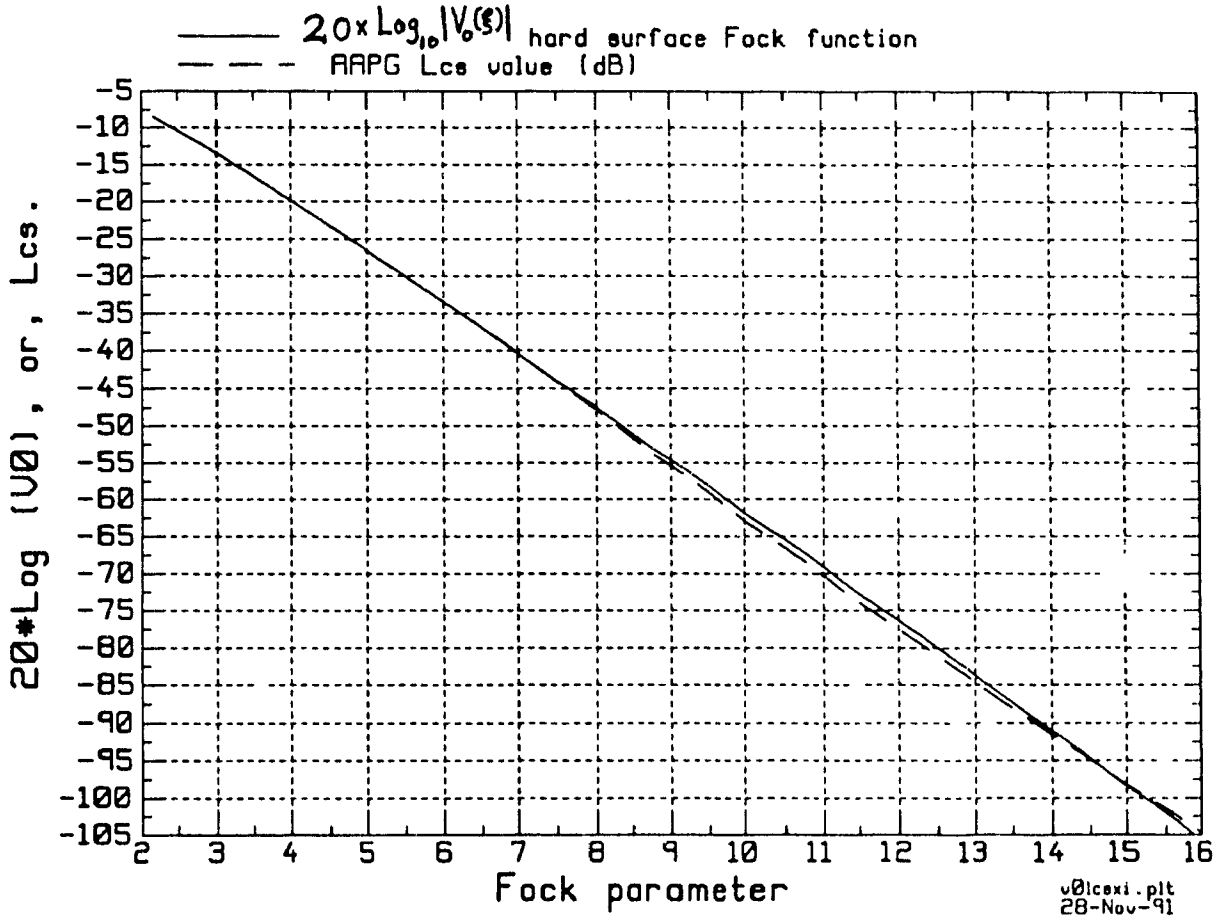

Fig. 5.2. Same as Fig. 5.2, except the range of agreement between L_{cs} and $20\times\mathrm{Log}_{10}|V_0(\xi)$ is shown in more detail. The agreement between the two is within $\frac{1}{2}$ of a dB.

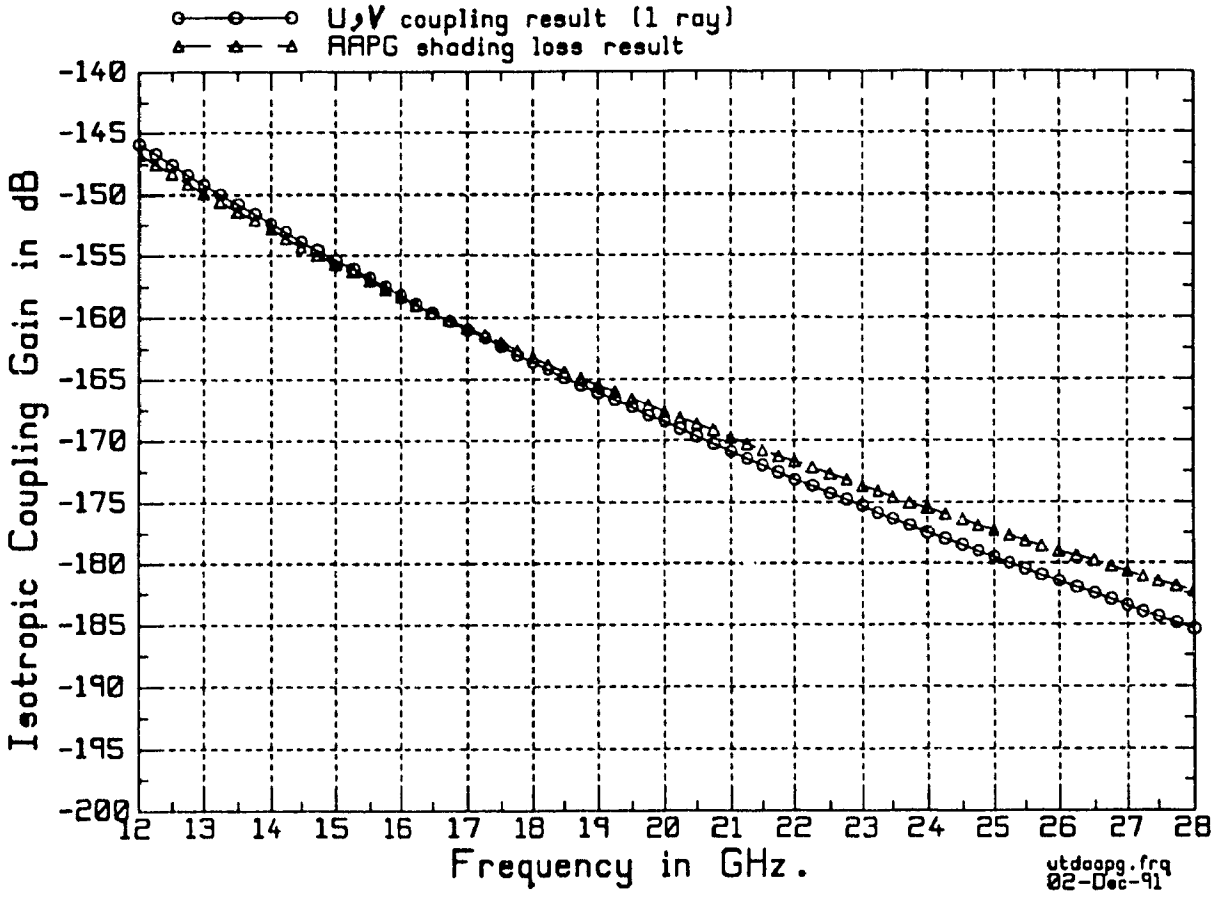

Fig. 5.3. Comparison between U, V formulation and AAPG code results for a single ray path. Here $a = 24''$, $\phi = 180^0$, $Z_{offset} = 0''$. One notes that AAPG predicts '*more*' coupling than the U, V result beyond 17 GHz - which corresponds to $\xi = 15.0$.

Thus, Figs. 5.1 and 5.2 show how the currently-used AAPG code can correctly be employed for applications to fuselage-mounted antennas. This can be inferred from the value $\xi \simeq 15.0$. This value of ξ sets an *upper limit* to the application of the AAPG code. The user can therefore judge the accuracy in AAPG model predictions by employing Eqn. (3.6) in Chapter 3 to determine the value of ξ for a particular path geometry and frequency, and, the plot as shown in Fig. 5.1 - which sets the cutoff value for ξ. It must however be noted that beyond $\xi \simeq 15.0$, the AAPG coupling results are safe from an EMC viewpoint, and hence do not lead to false predictions at high frequencies.

5.3 Evaluation of the AAPG code for off surface calculations

In this section the behavior of AAPG codes computation for off surface cases has been treated in detail. The validation of the AAPG code (version 07) calculation for the off-surface cases is shown in Fig. 5.1. The actual AAPG code was run at the EMC Lab, for h= $0\lambda, 5\lambda, 25\lambda, 50\lambda$, and, 500λ. The other data is shown in Fig. 5.1. The AAPG code outputs have been documented in Appendix A.3. The agreement between the results provides the necessary validation of the AAPG codes off-surface calculations.

Fig. 5.5 shows comparison between the U, V formulation, NECBSC2 and the AAPG code results when antennas are at $\phi = 180^0$. The result is shown as a

variation in $\frac{h}{\lambda}$, where $h = 0$ on the cylinder surface. The three results shown in Fig. 5.5 are now discussed separately below.

It is seen that NECBSC2 formulations near $h = 0\lambda$ are *non-physical*. This effect can be seen as a large change in coupling within a very small distance. For example within 0.2λ distance from the cylinder, the coupling changes by almost 30 dB ! The NECBSC2 actually predicts *infinite* coupling near the cylinder surface, and, because of this reason, one should not use the code for heights that are very small. This also points out the necessity in obtaining a value of the '*height*' where the NECBSC2 code can expected to give correct results. (This issue has been considered the following chapter.) The result in Fig. 5.5 is particularly important because the NECBSC2 code allows antennas to be located as close as 0.25λ to the curved surface of the cylinder. In Fig. 5.5 we also see that near $h \simeq 0.25\lambda$, the NECBSC2 code predicts a rather large difference of 25 dB between AAPG and U, V formulations. There is however almost no difference between the AAPG and U, V formulation data - indicating that near the cylinder surface, AAPG predictions are correct.

The U, V formulation results are inaccurate as the distances from the cylinder increase. This is because, again, the U, V coupling data predicts large increases in coupling as the height increases. This implies that the field from the cylinder surface increases monotonically with height. Such results are thus unacceptable, because, for the data at hand, *i.e.*, $\phi = 180^0$ in Fig. 5.5, there is no direct source ray, and hence the coupling cannot increase monotonically with height.

The U, V formulation and NECBSC2 results are seen to be *non-uniform* with

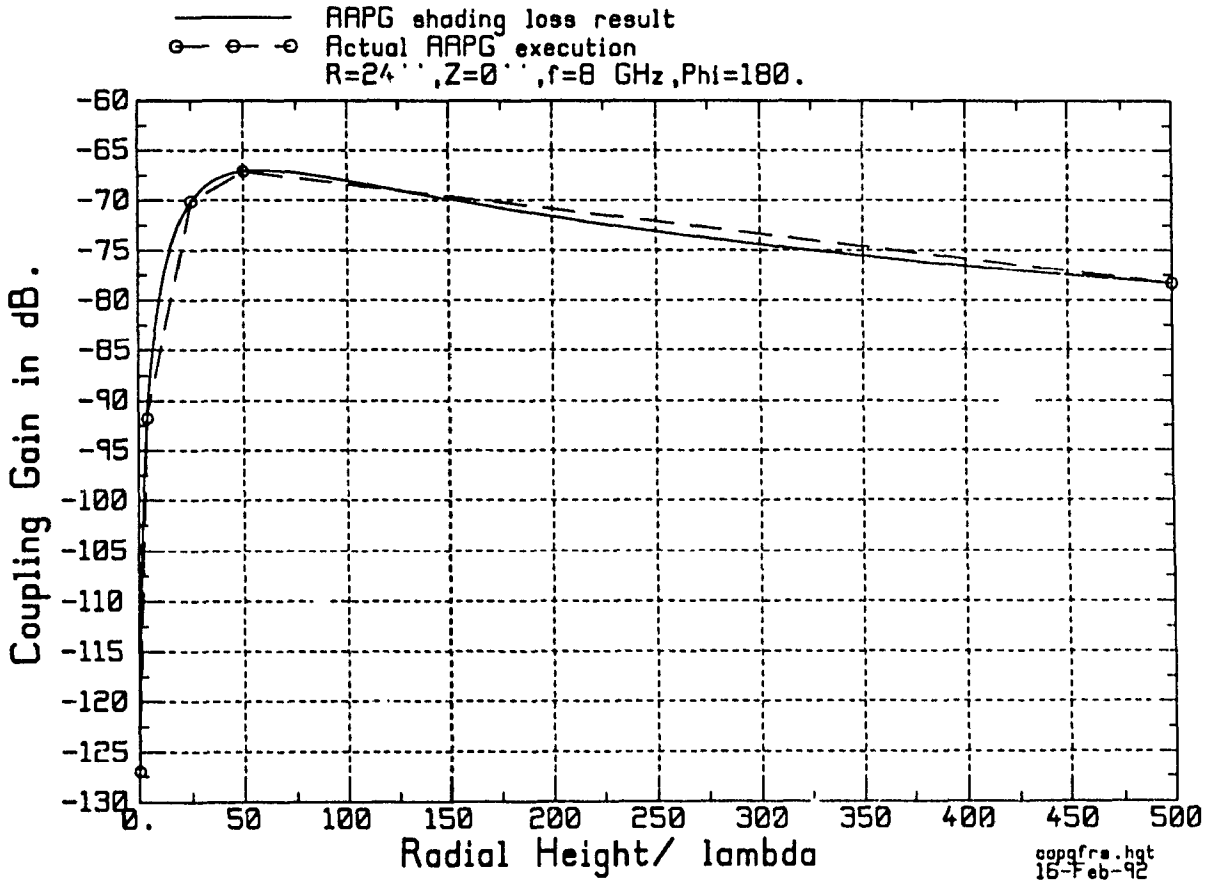

Fig. 5.4. Validation of the AAPG version 07 code's calculation for antennas off of the fuselage. The circles indicate actual AAPG code output executed at the EMC Lab From the AAPG code output (Appendix A.3), the Friis coupling was computed by adding 2.15 dB for both transmitter and receiver antennas to the surface shading and free-space spreading loss.

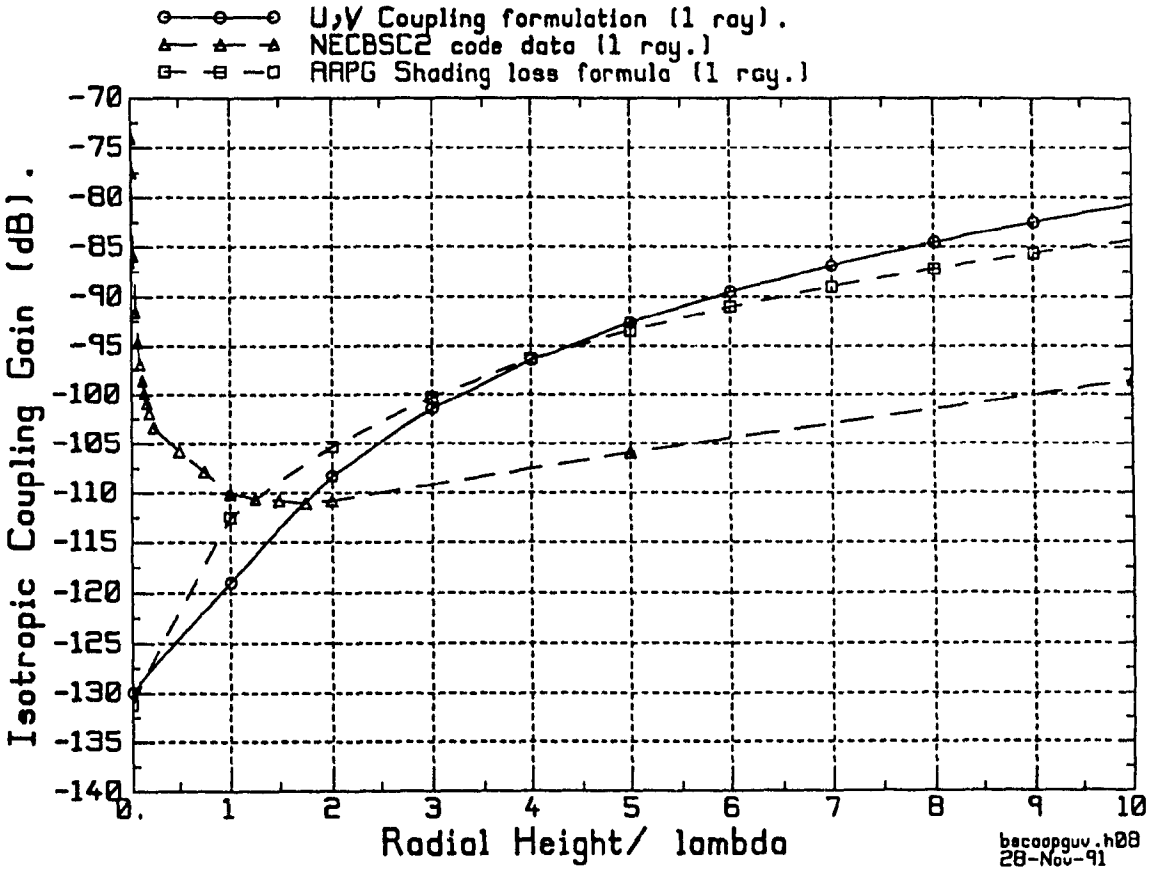

Fig. 5.5. Comparison between NECBSC2, U, V formulation and AAPG code data for antenna locations off the cylinder surface. $a = 24''$, $\phi = 180^0$, f= 8 GHz, $Z_{offset} = 0''$. Note that the NECBSC2 code predicts *infinite* coupling in the vicinity of the cylinder. At h= 9λ the AAPG code can be seen to predict 15 dB more coupling than the NECBSC2 code.

respect to height from the cylinder surface. It is because of this reason that the two formulations are *mutually exclusive* in nature. Mutual exclusivity is based upon the the fact that the two formulations are different mathematical approximations of two different physical situations. However, as one moves in $\frac{h}{\lambda}$, the electromagnetic field anywhere must be single valued and unique. Close to the cylinder surface, this field can be approximated via UTD coupling formulas (when $h \rightarrow 0$), and, far from the surface ($h \rightarrow \infty$) the approximation is accurate if the UTD scattering formulation is used. However, there exists no common region of overlap. This is effect of the nonuniformity in the two formulations. (The issue has been discussed in Chapter 6).

For antennas off the surface, the AAPG code *assumes* that the curved surface scattered field over the length L will be given by:

$$|\vec{\mathbf{E}}_{cs}^{AAPG}| \leq |\vec{\mathbf{E}}_{FRS}| \times |V_0(\xi)|. \tag{5.8}$$

In (5.8) $\vec{\mathbf{E}}_{FRS}$ is the free-space field of a magnetic dipole over the length L. The distance L has been defined in Fig. 3.1. Referring to Fig. 3.1, the general solution to the scattering problem has been obtained by Fock [12]. Following the discussions provided in Appendices A.1 and A.2, one can observe that when antennas are at extremely small heights the general result of Fock reduces to the $V_0(\xi)$ function, while at very large distances from the cylinder the same general solution can be adequately approximated by the Pekeris caret $\hat{P}_h(\xi)$ and the Fresnel integral. Therefore, it follows, that when antennas are at large distances, the form Eqn. (5.8) is not mathematically correct. Consequently, the AAPG result is incorrect for off-

surface locations, because it uses an incorrect mathematical approximation to the physical problem. The two different approximations, mentioned above, are radically different in character, and, hence the results from the AAPG and the NECBSC2 codes are different. It must however be noted, as in Fig. 5.5, that the AAPG code predicts safe results for off-surface locations even when it uses an inaccurate mathematical approximation to the scattered field.

5.4 Summary of results

In this chapter, the limitations of the AAPG code have been examined. It was found that for $\xi \geq 15.0$, the AAPG results are incorrect for the on-surface antenna locations. However, this problem can easily be remedied by implementing the actual form for $V_0(\xi)$ in the code. At present, the condition $\xi \geq 15.0$ for which AAPG code results are correct, can be used to determine the cutoff limits beyond which AAPG is expected to give incorrect results.

For off surface locations, the AAPG code uses an incorrect approximation to the curved surface scattered field. Nevertheless, the errors are always on the safe side. Therefore the code can continued to be used to model EMI coupling. At large distances away from the cylinder, the NECBSC2 gives correct results, however, it has been found that the NECBSC2 code is invalid close to the cylinder's surface.

The differences in the *U, V* formulations and the NECBSC2 results also suggest in determining an overlap height for use of the creeping wave formulations in the code in predicting coupling. This would serve as a switching criterion between the

two formulations.

Chapter 6

Limits of UTD scattering and coupling formulations

The results of the previous chapters clearly indicated the mutual exclusivity in coupling gain predictions from the NECBSC2 and AAPG codes - particularly when the antennas are in the deep-shadow, and, off the curved surface - as shown in Fig. 5.5. As discussed in Chapter 4, in connection with Harris results, the NECBSC2 code fails to model correctly the coupling near cylinders surface. It is particularly interesting to note that for a small height $h \simeq 0.06a$, (where $a = 24''$), the NECBSC2 results diverge from the actual on-surface coupling (AAPG or U, V formulation) data.

The results of Chapters 4 and 5 thus strongly suggest that within a very small distance, the NECBSC2 and AAPG creeping wave formulations exhibit nonuniformity. One might also suspect, based on physical grounds, that within a small height

the true coupling *cannot* be expected to change significantly from its on-surface ($h = 0$) value. This clearly indicates the need to investigate the limitations of the NECBSC2 code - that demands antennas to be $\frac{\lambda}{4}$ off the curved surface. Thus, one of the major aspects of this comparison was to investigate the limits of the two, *i.e.*, p, q (NECBSC2) and U, V (AAPG) creeping wave formulations.

Since, as discussed in Sec. 5.3, the AAPG cannot correctly predict the coupling for off-surface cases, the U, V formulation was employed in computing the the coupling for off-surface cases, because the formulation allows antennas to be located by a small height.

The NECBSC2 is invalid at small, while, U, V formulations is inaccurate at large heights. This was shown in Fig. 5.5. Therefore, one can expect, as the distance (height) is changed from $h = 0$, the NECBSC2 and U, V formulation data to overlap at some kh for a given value of ka. One can then use the result to find the regions of applicability: far from cylinder $kh \rightarrow \infty$, and NECBSC2 results are expected to be accurate, and, for $kh \rightarrow 0$, U, V formulations will give correct results. It is useful, from a practical viewpoint to have a 'rule-of-thumb' guideline regarding this overlap height. The search for such a empirical relation is the main focus of this chapter. The empirical relation has been obtained for ka= 10 and 102 for the present. Additionally, for $Z_{offset} = 0''$, an empirical relation for ka vs. kh with $Z_{offset} = 0''$ has also been obtained. The results are shown in this chapter.

In Sec. 6.1, the validation of the creeping wave formulations as in the NECBSC2 code is shown. In Sec. 6.2, the method by which this height was found, is described.

Results have been included to establish the validity of this proceedure. Section 6.3 summarizes the investigations of this chapter.

6.1 Validation of the NECBSC2 creeping wave formulations

It is important to investigate, if, at all the NECBSC2 results overlap with the UTD coupling data. This will indicate any peculiarities of the code. To this end it appeared judicious to compare the C vs. ϕ coupling, since, this gives more useful information than the C vs. f cases. To achieve our objective, the actual NECBSC2 code was executed and the results were compared with U, V formulation. A typical result of this overlap is shown in Fig. 6.1.

Fig. 6.1 shows that U, V formulation and the NECBSC2 code do not overlap if the two ray fields are considered. This suggested in comparing the UTD scattering formulation of creeping waves as in the NECBSC2 code to be used in determining the overlap height. A computer program based on the NECBSC2 creeping wave formulas was written and the results from the program is refered to as 'p, q' formulation results throughout the remainder of this thesis.

To simplify the investigations, it was decided to work with the single ray coupling. (This also seems appropriate in view of the AAPG codes' computation - which considers only the dominant ray.) To compute the isotropic gain, one has to subtract the gains from the NECBSC2 codes output, and, this increases the and

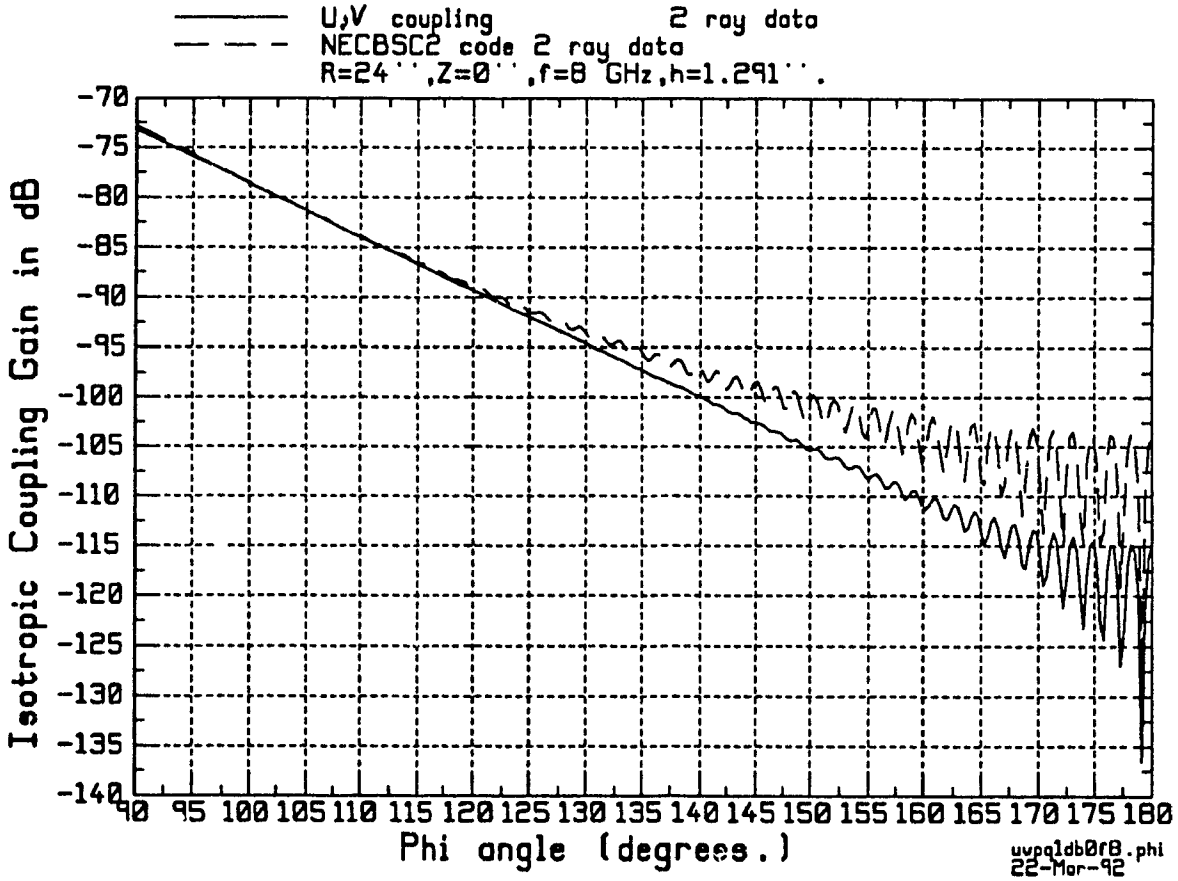

Fig. 6.1. Comparison of overlap of isotropic coupling from U, V formulation and the NECBSC2 code. Here $a = 24''$,$Z_{offset} = 0''$.f= 8 GHz, and h= 0.875λ.

labor involved in such typical computations. Thus it was necessary to develop an alternate proceedure that can perform the same task and still can be validated with the NECBSC2 codes output. The results from the UTD scattering formulation for creeping waves are referred to as p, q formulation in the remainder of this chapter.

Fig. 6.2 shows a direct comparison between U, V and p, q results for the single creeping ray path. The data is the same as in Fig. 6.1, and thus is not repeated here. One can clearly observe the peculiar nature of the p, q formulation in the deep-shadow, *i.e.*, beyond $\phi \simeq 130^0$. In the same figure, the U, V formulation shows a linear decay in coupling with ϕ.

To verify this peculiar nature, the p, q result was compared against the NECBSC2 code - that is shown in Fig. 6.3. Here a= 24", f= 8 GHz, and h= 0.875λ and $Z_{offset} = 0"$. The result in Fig. 6.3 indeed confirms the fact that the peculiar nature is a manifest of the p, q creeping wave formulation, and, is independent of the two ray one ray issue. Thus, it also became clear that the overlap height can be determined by simply comparing directly the p, q and U, V results independently of any code. (Similar validation results have been obtained for $Z_{offset} \neq 0"$, but, are omitted here for brevity.)

6.2 Numerical determination of the overlap height

It was found that NECBSC2 code and U, V formulation did overlap for the C vs. ϕ case for an arbitrary geometry. To avoid the tedium of determining isotropic coupling directly from the NECBSC2 code - every time a set of results were required,

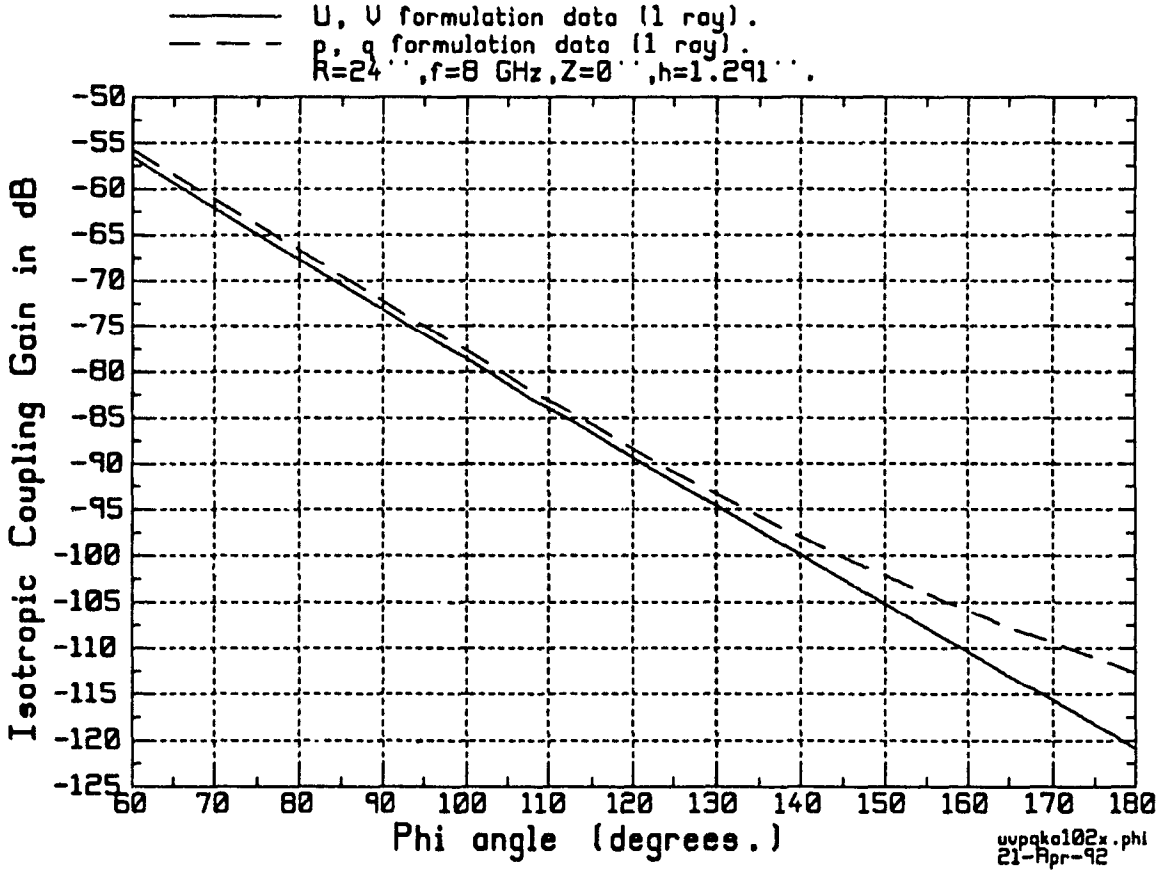

Fig. 6.2. Comparison between single ray data from U, V and p, q formulations. Here ka= 102 and kh= 5.5. Other data is also shown here.

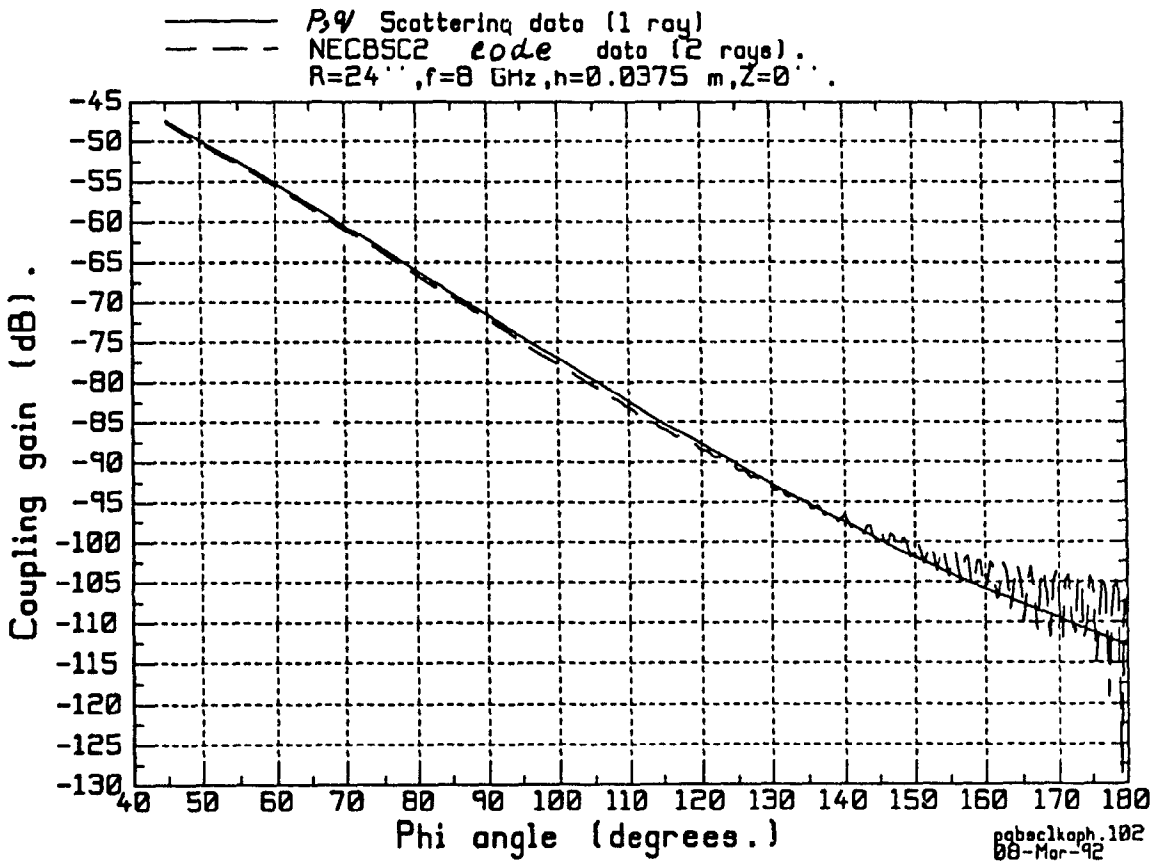

Fig. 6.3. Comparison between the single ray isotropic coupling from the p,q formulation and the NECBSC2 code. One can observe the overlap for this single ray case upto $\phi \simeq 140^0$. Here $ka = 102$. The result validates the p, q formulation in the NECBSC2 code. The data was taken from Harris report [10. p. 58], and, is the same in Fig. 6.2.

the p, q formulations were validated against the NECBSC2 code. Thus, the two single ray creeping wave formulations could be used more effectively for comparison of the overlap of coupling data. This section is is concerned in finding the overlap height which allows the user/ designer to estimate, as a rule-of-thumb, the limits of the accuracy of U, V and the p, q formulations. This in turn, shows the limitations in the practical applications of the NECBSC2 code.

It may perhaps have been desirable to obtain an analytical formula for height. However, as shown in Appendices A.1 and A.2, the mathematical forms underlying the formulations are, at present, inadequate to provide us with an analytical expression - suitable for practical computations. Therefore, the determination of this height was done rather empirically. This approach, although somewhat heuristic, yields useful answers for practical engineering applications. The merit of this approach is that it *does not* involve mathematical complications. The disadvantage of the approach is that it is numerically involved and one is not sure regarding the individual accuracies of the two formulations at an overlap height. The method is described below.

The method consists of computing the isotropic coupling (C vs. ϕ) from the p, q and U, V formulations, till a reasonably good agreement (within 1 dB) was obtained. This proceedure is repeated for two values of ka. A smooth curve was found for the two values of ka, and, finally the results from the curve were further validated to ensure accuracy in predictions from the approximate curve. It was also found that the overlap height kh was a function for the axial separation kZ_{offset}.

This functional form was obtained by assuming a parabolic relation between points for fixed values of ka. The total number of datapoints was between 4 and 5 for every set of ka = 10 and 102. For ka = 102, which corresponded to $a = 24''$ and f= 8 GHz, the overlap was found by comparing the U, V and NECBSC2 single ray results. (This was done for all the overlap data at ka = 102.) For ka= 10, the overlap height was found by directly comparing the U, V and p, q formulas. To examine the dependencies of overlap height on the cylinder radius or size, empirical relations have also been obtained for $Z_{offset} = 0''$.

To obtain accurate results, it became necessary to proceed as precisely as possible, since the NECBSC2 results, as shown in Fig. 5.5, could change abruptly in the close vicinity of the cylinder. By starting at $\frac{\lambda}{4}$, the height was changed till the U, V results exceeded the p, q or NECBSC2 data. Next the height was reduced from this value till the U, V results were lower, and, then within a few iterations between the above two limits, the best overlap height within 1 dB was found. This process was repeated for several Z_{offset} values for a given ka. Figs.6.4, 6.5 show the results for $ka = 102$.

In Fig. 6.4, the NECBSC2 and U, V formulation data is shown for C vs. ϕ variation for $a = 24''$, f= 8 GHz, and $Z_{offset} = 305.5''$. For the NECBSC2 runs, radial, $\frac{\lambda}{2}$, electric dipoles were chosen because the gains along both the paths are same (2.13 dB). The isotropic coupling from the U, V and NECBSC2 codes agree within 1 dB - which decreases all the way upto 120^0. Beyond 120^0, the NECBSC2 data is dominated by 2 rays.

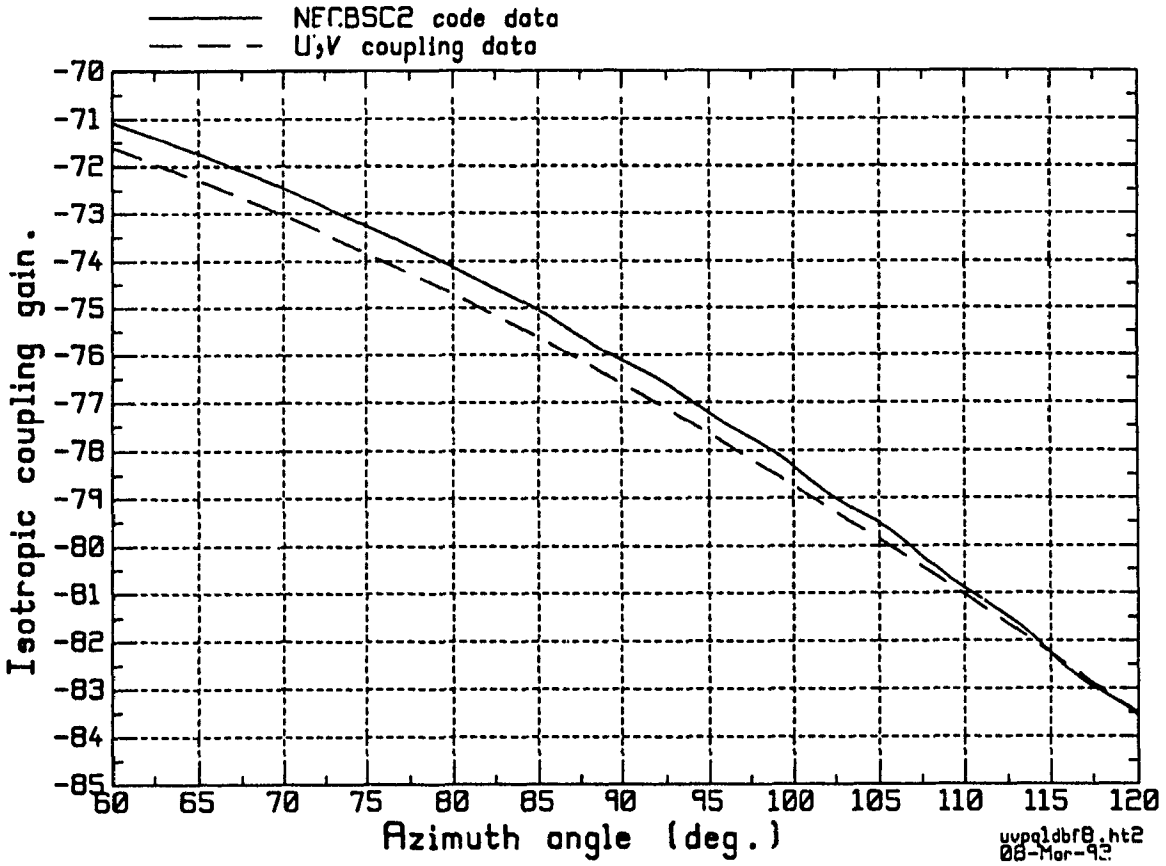

Fig. 6.4. Comparison between NECBSC2 code single ray and U, V results. Here $a = 24''$, f= 8 GHz, Z= 305.5″ and h= 0.0865 m. The difference is within 1 dB at $\phi = 60^0$. At $ka = 102$, the overlap height is h= 2.3λ, and Z= 207λ.

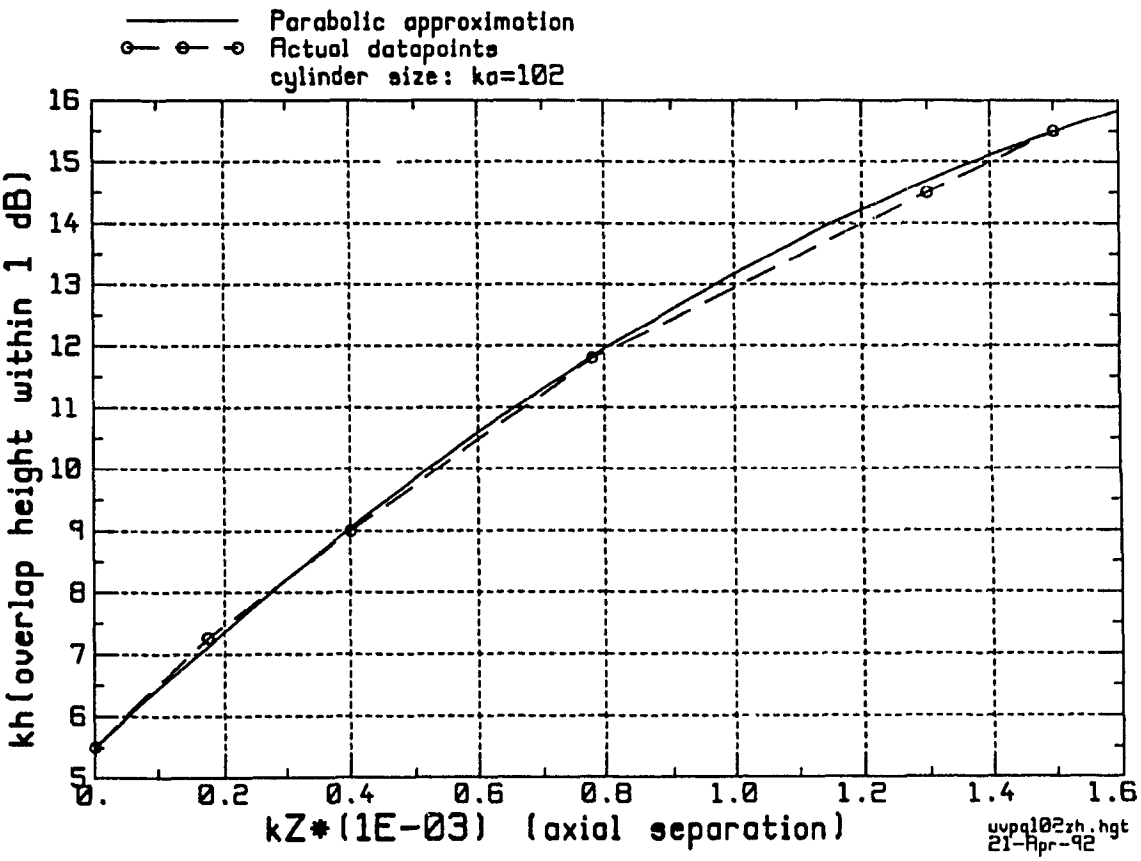

Fig. 6.5. Single ray overlap height for $ka = 102$. The discrete points were found by comparing the U, V formulation and NECBSC2 results in the single ray regions for $ka = 102$. The '*smooth*' curve passing through the points can be approximated by a parabola. If $x = kZ \times 10^{-3}$ and $kh = S(x)$, then the curve (solid line) has the equation: $S(x) = 5.49 + 9.7153x - 2.0306x^2$.

In a similar manner, for $ka = 102$ with f= 8 GHz, and $a = 24''$, other axial offsets were tried and agreement within 1 dB was obtained between the NECBSC2 and *U, V* code results in the single ray regions. These corresponded to axial offsets: $Z_{offset} = 0'', 36'', 180''$ and $360''$. The overlap heights were obtained at h= $0.875\lambda, 1.15\lambda, 1.875\lambda$, and, 2.5λ respectively. The $kZ \times 10^{-3}$ and kh values were plotted, and, the results for $ka = 102$ can be seen in Fig. 6.5.

In Fig. 6.5, a smooth curve approximation was found, and, it reads:

$$S(x) = 5.49 + 9.7153x - 2.0306x^2. \tag{6.1}$$

This result is valid *only* for $ka = 102$. In Eqn.(6.1), we have $kh = S(x)$ and $x = kZ \times 10^{-3}$.

The above results and discussions established a confidence in the technique. Next, the proceedure was applied to $ka = 10$. For this value, $a = 24''$ and f= 0.785 GHz. To avoid labor in computing the isotropic coupling, *p, q* formulation was used in place of the NECBSC2 code. Fig. 6.6 shows the approximation for the case of ka= 10.

In Fig. 6.6 the empirical relation for $ka = 10$ is given by:

$$S(x) = 2.36 + 20.57x - 10.638x^2. \tag{6.2}$$

As before, *i.e.*, in (6.1), $S(x) = kh$ and $kZ \times 10^{-3} = x$. The validity of this equation was checked by choosing $a = 15''$ and f= 1.25 GHz. At $Z_{offset} = 0''$ the height h= 0.09015 m via Eqn. (6.2). The results are shown in Fig. 6.7

In Fig. 6.7 ($Z_{offset} = 0''$) a difference of about 2 dB is seen. The computations start from the grazing angle. It is interesting to note that the maximum difference

is exactly at the grazing angle. The p, q formulations for creeping waves are valid below the grazing line; for the U, V case, no such geometrical boundaries exist. Therefore, this difference is attributed due to the differences in the U, V and p, q formulations at the grazing, or, line of sight locations.

Fig. 6.8 shows the dependencies on the cylinder radius and kh. It was found that an empirical relation could be obtained, which reads:

$$S(x) = 2.13 + 3.75 \times 10^{-2}x - 4.35 \times 10^{-5}x^2 \tag{6.3}$$

In Eqn. (6.3), $x = ka$ and $kh = S(x)$. The results in Figs. 6.5,6.6 and 6.8 allow us to conclude that the overlap height is a function of:

(1) the cylinder radius ka, and,

(2) the axial separation kZ_{offset}.

In the next section the deep shadow region discrepancies of the U, V and p, q formulations are studied.

6.3 Differences in the U, V and p, q formulations in deep shadow (large ϕ) regions.

It is well known that an exponential decay $e^{-j\nu_n\phi}$ can be associated with a creeping wave field amplitude. Here ϕ is the azimuth angle and the quantity ν_n is the complex attenuation constant. One can show that this implies a linear decay in ϕ on a logarithimic (dB) scale. The reader is suggested to refer to Figs. 6.2 and 6.9 for the discussions in this section.

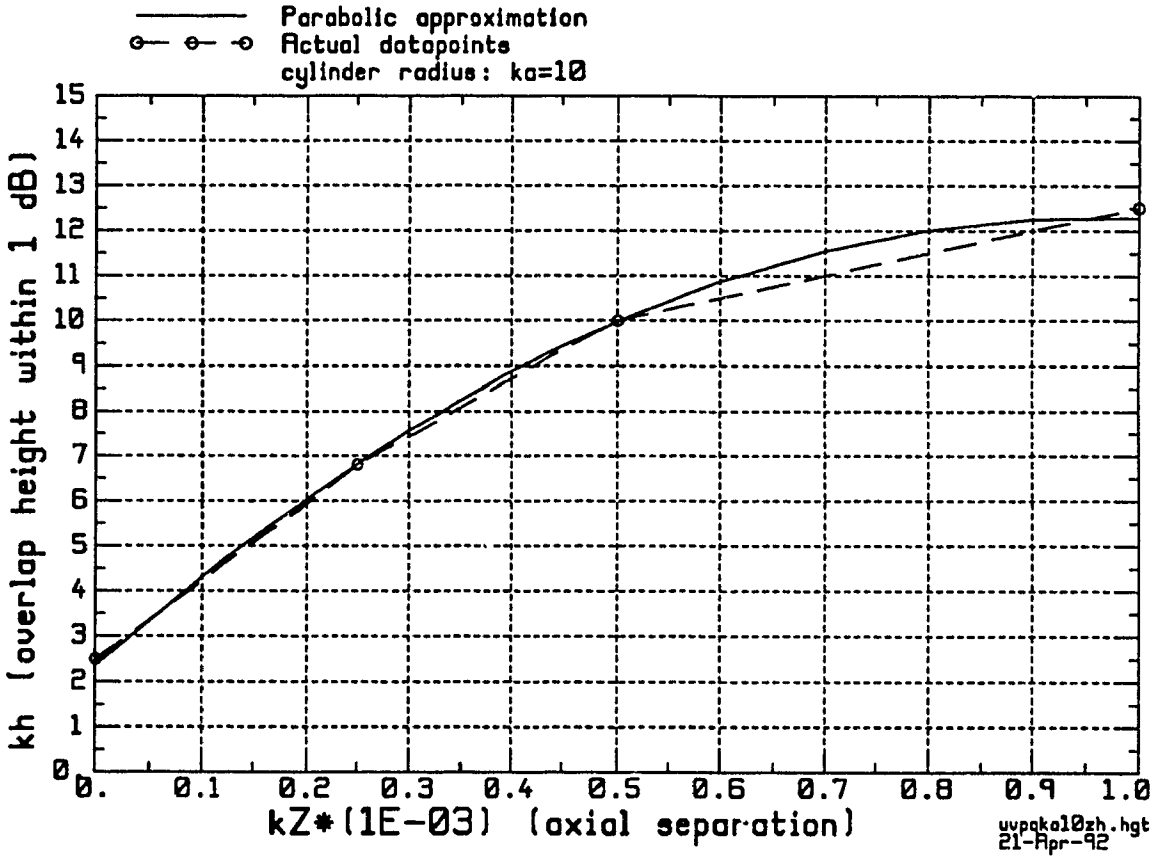

Fig. 6.6. Single ray overlap height for $ka = 10$. The discrete points were found by comparing the U, V and p,q formulations results in the single ray region for $ka = 10$. The '*smooth*' curve passing through the points could be approximated by a parabola. If $x = kZ \times 0.001$ and $kh = S(x)$, then the curve (solid line) has the equation: $S(x) = 2.36 + 20.57x - 10.638x^2$.

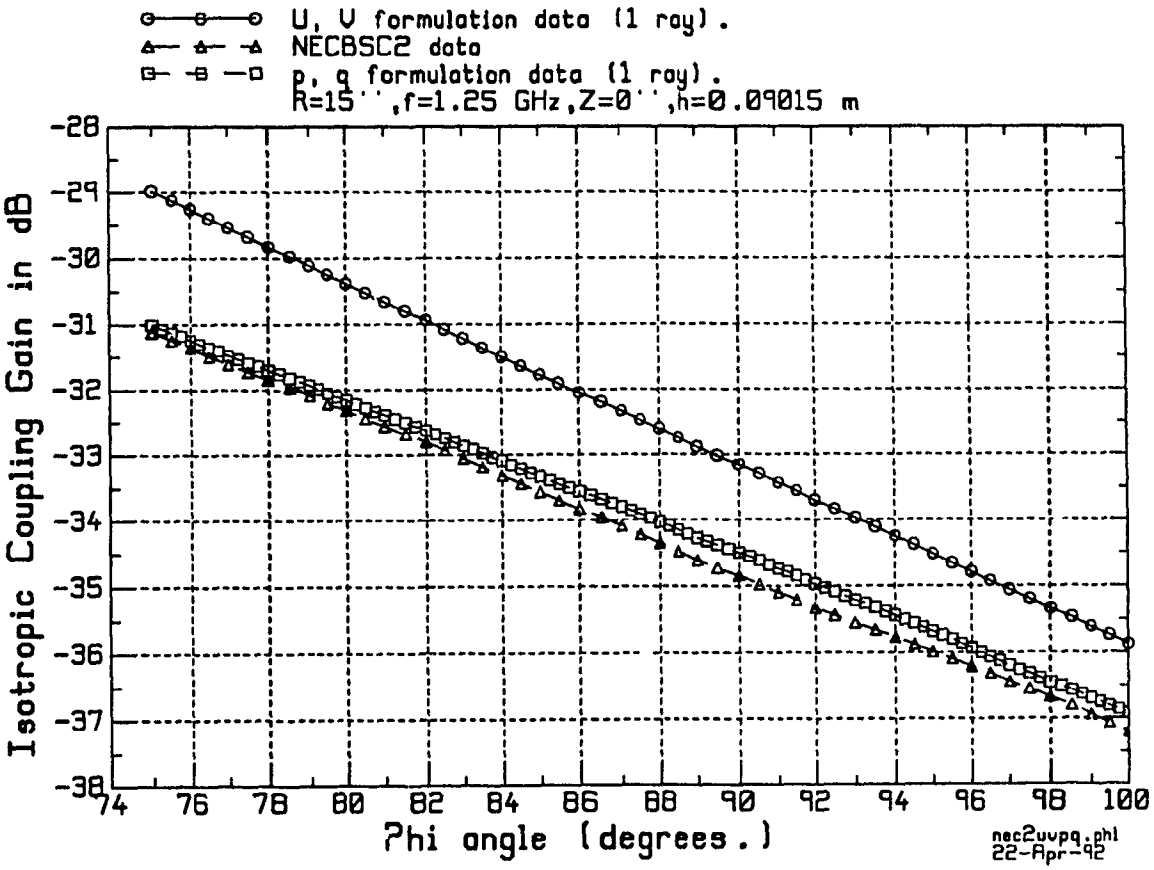

Fig. 6.7. Validation of single ray data from U, V, p, q and NECBSC2 codes for $ka = 10$. The cylinder radius $a = 15''$ and f= 1.25 GHz; $Z_{offset} = 0''$ was selected for $kZ \times 10^{-3} = 0$. From the empirical equation of the curve in Fig. 6.6, $h = 0.09015$ m was calculated. The difference between the NECBSC2 and p,q results is less than 0.5 dB.

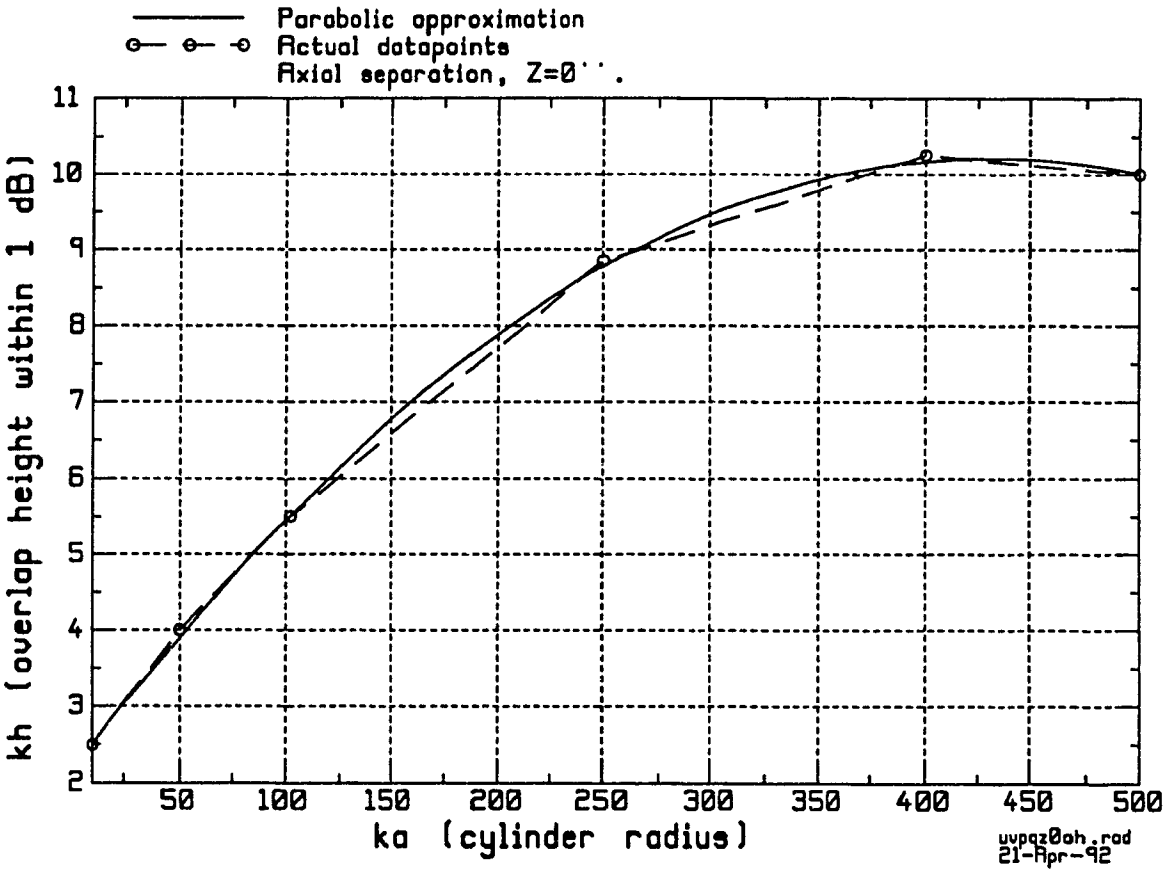

Fig. 6.8. Empirical relation for the overlap height as a function of the cylinder radius. If $x = ka$, and, $kh = S(x)$, then the curve (solid line) has the equation $kh = S(x) = 2.13 + 3.75 \times 10^{-2}x - 4.35 \times 10^{-5}x^2$. The result is valid for $Z_{offset} = 0''$.

The result in Figs. 6.2 and 6.9 show an interesting behavior in the present p, q formulations. The data shown in those figures refer to $ka = 102$ and 1000 respectively. One can see that beyond $\phi \simeq 140^0$ (Figs. 6.2 and 6.9), the linear decay is absent in the p, q formulations. As shown in Figs. 6.2,9, the U, V formulations exhibit a linear behavior.

The results in Figs. 6.2 and 6.9 show that there is a problem in the p,q formulation as the one ray field does not show the linear type of behavior. This improper behavior has been recently studied by Hussar and Albus [21]. It turns out that the p, q formulation does not properly reduce to Keller's deep shadow creeping wave modes when the observation point is fairly close to the surface and the cylinder is very large. Hence, it can be misleading to conclude that the p, q formulation or the NECBSC2 code becomes increasinly accurate with large ka. The work of Hussar and Albus specifically shows that this is not the case.

The investigation presented in this chapter, points out similar problems with the UTD scattering or p, q formulation as was observed by Hussar and Albus in [21]. The peculiar behavior of the p, q formulations - as shown in the Figs. 6.2 and 6.9 was not observed for smaller size cylinders, *i.e.*, for ka= 10. This strongly suggests that the p, q formulations in the NECBSC2 code are inaccurate in the deep-shadow (large ϕ) when $ka \rightarrow \infty$ (large cylinders). (In Figs. 6.2 and 6.9 ka= 102 and 1000 respectively.) The reason, as pointed out by Hussar and Albus, is due to the fact that the Fresnél integral (transition function), $F(X^d)$, dominates over the Pekeris carets, $\hat{P}_{s,h}(\xi)$, in the deep-shadow, and, hence the proper expression for the creeping

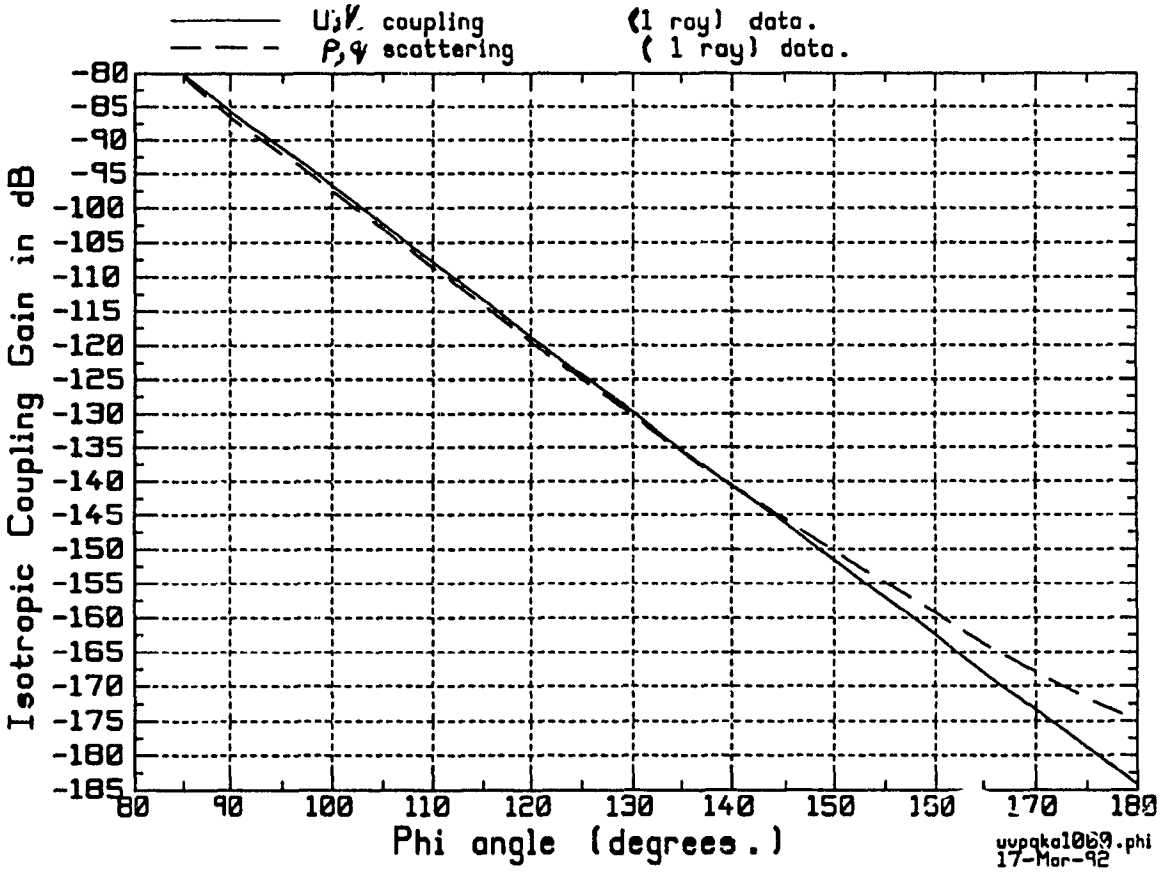

Fig. 6.9. Single ray overlap between U, V and p, q formulations. Here $a = 37.6''$ (ka= 1000), f= 50 GHz, $Z_{offset} = 0''$. The overlap height is kh= 314.16. The p, q data shows a departure from the linear behavior beyond $\phi = 145^0$.

wave fields in the deep-shadow, given by Levy-Keller theory, is not obtained from the UTD theory of Pathak *et al.* [7]. This occurs for large cylinders ($k \to \infty$ and hence $ka \to \infty$) and for observation points in the deep-shadow. Thus, in the light of Hussar and Albus's work, the p, q results in Figs. 6.2 and 6.9 can be considered to be inaccurate in the deep shadow. Coincidentally, the deep shadow region is seen to occur whenever the two rays in the p, q formulation become almost equally dominant.

Chapter 7

Conclusions

In this thesis, numerical comparisons between the U, V formulation and the previously published AAPG code results of Harris have been reported. The comparisons show perfect agreement between the two results, and, hence indicates that the AAPG code can correctly predict the on-surface (h= 0) coupling.

Harris NECBSC2 results have also been replicated to an excellent degree of accuracy by an alternate technique that requires *no* modification to the NECBSC2 code. By not modifying the code, this leaves the user free of any any ambiguities that could have otherwise resulted if the code were modified. The antennas were kept at h= 0.0375 m for both the ϕ and frequency variations. The excellent agreement between Harris and our NECBSC2 results establishes confidence in the alternate technique that was used in replicating Harris results.

Additionally, the NECBSC2, AAPG codes, U, V formulation, and, measured data obtained from the Harris report have been compared. As the NECBSC2 data

diverged from the *U, V* and AAPG code and measured data, it was demonstrated that the NECBSC2 code, or, equivalently the *p, q* formulation cannot model the on-surface coupling cases. Hence, it was concluded that Harris had made erroneous comments regarding the inadequacies of the AAPG code.

The evaluation of the shading loss, $L_{cs}(\xi)$, and the hard surface Fock function $V_0(\xi)$ against the Fock parameter ξ showed that beyond $\xi \geq 15.0$ the AAPG code uses an incorrect approximation to the creeping wave loss. Thus, for some arbitrary combination of electrical and geometrical parameters, whenever $\xi \geq 15.0$, the AAPG code results are inaccurate. This inaccuracy is *safe* from the viewpoint of EMC applications, as AAPG code predicts more coupling beyond $\xi \geq 15.0$. For off surface locations the AAPG code continues to predict increased coupling levels, which being theoretically incorrect, are nevertheless safe from an EMC viewpoint. It was also found that in the vicinity of a cylinder surface the NECBSC2 code predicts infinite coupling as the *p, q* formulations for creeping waves become invalid. The results thus established that the *U, V* and *p, q* formulations are *mutually exclusive* in nature, and, one cannot be a substitute for the other.

The above results led to detailed investigations regarding the overlap between *U, V* and *p, q* formulations for varying values of *ka*. It was then numerically found that an overlap within a maximum of 1 dB of variation between *U, V* and *p, q* formulations could be obtained. This empirical relation for the overlap height has been obtained for ka= 10 and 102 as a function of Z_{offset}. It has also been shown that for heights that are much larger than the computed overlap height, the NECBSC2

code results can expected to be accurate.

Additionally, empirical relations between overlap height and cylinder radius has also been obtained for $Z_{offset} = 0''$. These curves indicate the optimum switchover point for a cylinder of abritrary radius ka.

References

[1] R.E.Collin, *Antennas and Radiowave Propagation*, New York: Mc-Graw Hill, 1985.

[2] R.G.Kouyoumjian and P.H.Pathak,"A Uniform GTD Approach to EM Scattering and Radiation",ch. 3 in *Low and High Frequency Asymptotics*. V.K.Varadan and V.V.Varadan (eds.). New York: North-Holland, U.S.A, 1986.

[3] P.H.Pathak and N.N.Wang,"An Analysis of the Mutual Coupling between antennas on Smooth Convex Surface", Final Report 724583-7, prepared for the Department of Navy, Naval Air Development Center, Warminster, PA, October 1978. (see also:"Ray Analysis of Mutual Coupling between Antennas on a Smooth Convex Surface",*IEEE Transactions on Antennas and Propagation*,vol. AP-29, pp. 911-922, November 1981.)

[4] G.Hasserjian and A.Ishimaru,"Excitation of a Conducting Cylindrical Surface of large radii of curvature",*IRE Transactions on Antennas and Propagation* ,vol.

AP-10, pp. 264-272, May 1962.

[5] R.J.Marhefka and W.D.Burnside,"Numerical Electromagnetics Code - Basic Scattering Code", NEC-BSC (version 2), Part 1: User's Manual, The Ohio State University, ElectroScience Laboratory, Columbus, Ohio, Technical Rep 712242-14, Department of Navy, Long Beach, CA 90822, U.S.A, December 1982.

[6] H.P.Widmer,"A technical description of the AAPG program", ECAC-CR-83-048 DoD Electromagnetic Compatibility Analysis Center, North Severn, MD, USA, 1983.

[7] P.H.Pathak, W.D.Burnside, and R.J.Marhefka,"A Uniform G.T.D Analysis of the Scattering of Electromagnetic Waves by Smooth Convex Surfaces", Electro-Science Lab Tech. Report, ESL-784583-4, 1980. (see also : *IEEE Transactions on Antennas and Propagation*, vol AP-28, pp. 631-642, September 1980.)

[8] P.H.Pathak,"An Asymptotic Analysis of Scattering of Plane Waves by a smooth convex cylinder",*Radio Science*, vol 14, no 3, pp. 419-435, 1979.

[9] B.R.Levy and J.B.Keller,"Diffraction by a Smooth Object", *Communications in Pure and Applied Mathematics*,vol 12, pp. 159-209, 1959.

[10] T.E.Durham,"SHF/EHF Antenna-to-Antenna EMI Coupling", Harris Corp., (vols 1 and 2), Contract No F30602-85-C-0114, Rome Air Development Center, Air Force Systems Command, Griffis Air Force Base, N.Y. 13441, August 1987, U.S.A. (see also : T.E.Durham,"Analysis and Measurement of EMI Coupling for Aircraft-Antennas at SHF/ EHF,"*IEEE EMC Conference Proceedings*, August 1987.)

[11] S.J.Kubina,"Numerical Modeling Methods for Predicting Antenna Perfor-

mance on an Aircraft", *AGARD Lecture series paper no 131*, 1983.

[12] V.A.Fock,'*Electromagnetic Diffraction and Propagation Problems*', New- York: Pergamon Press, 1965

[13] G.Genello and A.Pesta,"Aircraft Coupling Model Evaluations at SHF/EHF", *IEEE EMC Symposium Conference Proceedings*, pp. 72-74, 1985

[14] N.A.Logan,"General Research in Diffraction Theory", LMSD 288087,Lockheed Missiles and Space Division, Lockheed Aircraft Company, Sunnyvale, California, December 1959.(vol 1.). See also LMSD 288088, vol. 2.

[15] R.J.Marhefka and N.Wang,"GTD Curved Surface Applications",in 'The Modern Geometrical Theory of Diffraction",vol 2.,ElectroScience Laboratory, The Ohio State University, Columbus OH, 1980

[16] S.A.Davidson and G.A.Theile,"A Hybrid Method of Moments-GTD Technique for Computing Electomagnetic Coupling between two Monopole antennas on a large cylindrical surface",*IEEE Transactions on Electromagnetic Compatibility*, vol. EMC-26, no. 2, pp. 90 - 97, May 1984.(see also: S.A.Davidson,"A Hybrid Method of Moments Technique for Computing Electromagnetic Coupling between two Monopole Antennas on a large Cylindrical surface".M.S.E.E thesis, The Ohio State University, Dayton, Ohio, U.S.A, Winter 1980.)

[17] S.W.Lee,"A Review of GTD calculation of Mutual Admittance of Slot Conformal Array", *Electromagnetics Journal*, vol. 2, 1982, pp. 85-127

[18] J.Shapira, L.B.Felsen and A.Hessel,"Surface Ray Analysis of Mutually Coupled Arrays on Variable Curvature Cylindrical Surfaces",*Proceedings of the IEEE*,

vol. 62, Nov. 1974, pp. 1482 - 1492.

[19] W.Klocko, P.Masters, P.Hussar and B.Campbell,'A Technical Description of the Aircraft Inter-Antenna Propagation with Graphics (AAPG) Computer Program', ECAC-HDBK-90-083. DoD Electromagnetic Compatibility Analysis Center, North Severn, Annapolis, MD, April 1990.

[20] R.F.Harrington,*Time Harmonic Electromagnetic Fields*, McGraw-Hill Book Company, New York, 1961

[21] P.Hussar and R.Albus,"On the Asymptotic Frequency Behavior of Uniform GTD in the Shadow Region of a Smooth Convex Surface",*IEEE Transactions on Antennas and Propagation*, vol. 39, no. 12, Dec. 1991, pp. 1672 - 1680.

[22] D.Chatterjee, S.J.Kubina and R.Paknys,"An Apparisal of Creeping Wave Formulations in the NEC-Basic Scattering (NECBSC2) Code for AAPG code applicability",technical report # TN-EMC-81-08, EMC Laboratory, Dept. of Electrical and Computer Engineering, Concordia University, Montreal, Québec, CANADA, August 1991.(see also: D.Chatterjee,S.J.Kubina and R.Paknys,"Coupling Gain Computations between antennas on large circular cylinders at SHF,EHF", presented at *Third Canadian Conference on Electrical and Computer Engineering, Ottawa, Sept 1990*,vol II, pp. 46.4.1 to 46.4.3)

[23] D.Chatterjee, R.J.Paknys and S.J.Kubina,"Numerical Comparison of Creeping Wave Formulations in the NEC-Basic Scattering Code (NECBSC2)and AAPG codes with applications to EMI Coupling prediction",technical report # TN-EMC-91-12, EMC lab., Concordia University, Montreál, Quebéc, Canada, December 1991.

Appendix A

A.1 Approximation to the generalized hard Fock integral when both antennas are at small heights off the cylinder

The generalized hard-Fock integral [3, Eqn. (45)], specialized for a circular cylinder, reads:

$$F_h(\xi, y_s, y_r) = \frac{e^{-j\frac{\pi}{4}}\xi^{\frac{1}{2}}}{4\pi^{\frac{1}{2}}} \int_\Gamma e^{-j\tau\xi} d\tau W_2(\tau - y_s) \left[W_1(\tau - y_i) - \frac{W_1'(\tau)}{W_2'(\tau)} W_2(\tau - y_i) \right]. \tag{A1.1}$$

Our objective is to obtain the result stated in [3, Eqn. (49)]. Eqn. (A1.1) applies to antennas *on*, or, *off* the cylinders surface and the heights are arbitrary in this equation. This effort may apparently seem redundant at a first glance, but, its derivation - in the technical report of Pathak and Wang [3] - for small heights is not available. Since modeling of EMI coupling between two finite, cylinder-mounted, radial monopoles requires one to account for those portions of the monopole length

that are not exactly on the cylinder surface but '*close*' to it, it is worth investigating this derivation - to fully understand the major limitations when subjected to such applications.

One begins by approximating the Fock-type Airy functions in (A1.1) by their Taylor series forms for small heights. This means $y_{s,r} \simeq 0$. We have:

$$W_j(\tau - h) \simeq W_j(\tau) - hW_j'(\tau) + \left(\frac{\tau h^2}{2}\right) W_j(\tau). \qquad (A1.2)$$

In (A1.2), $j = 1,2$ designate the two categories (complex conjugates) of Fock- type Airy functions used in (A1.1). $h = y_{s,r}$ are the 'heights' above the curved surface of the cylinder. The higher order terms in the Taylor series have been neglected, because the main assumption is that h, or, equivalently $y_{s,r}$ is small. Therefore, we can simplify the term $\left[...\right]$, in (A1.1), as follows:

$$\left[...\right] \simeq \Omega_w \left[1 + \frac{\tau {y_r}^2}{2}\right] \frac{1}{W_2'(\tau)}. \qquad (A1.3)$$

The quantity $\Omega_w = W_2'(\tau)W_1(\tau) - W_1'(\tau)W_2(\tau) = -2j$ is the wronskian relation for Fock-type Airy functions, as can be found in Logan's report [14, vol. 1]. Consequently one can simplify (A1.1) as:

$$\int_\Gamma (....) d\tau = -2j \int_\Gamma e^{-j\xi\tau} \left(1 + \frac{\tau y_r^2}{2}\right) \frac{W_2'(\tau - y_s)}{W_2'(\tau)}. \qquad (A1.4)$$

The R.H.S of (A1.4) can be further simplified via (A1.2) to expand $W_2(\tau - y_s)$ and ignoring all terms involving $y_s y_r^2$, $y_s^2 y_r^2$ e.t.c. Moreover, upon incorporating these simplifications, one will still be left with the integral $2jy_s \int_\Gamma e^{-j\xi\tau} d\tau$. However, this integral vanishes for *all* $\xi \neq 0$. Thus, specializing in the deep-shadow $\xi >> 0$, we note that,

R.H.S of (A1.4)

$$= -2j\int_{\Gamma} e^{-j\xi\tau}\left[\frac{W_1(\tau)}{W_2'(\tau)}\right]d\tau - j(y_r^2+y_s^2)\int_{\Gamma} e^{-j\xi\tau}\left[\frac{\tau W_2(\tau)}{W_2'(\tau)}\right]d\tau. \qquad (A1.5)$$

Finally, we use the standard formulas for $V_0(\xi)$ and $V_1(\xi)$ as can be found in [3, Eqns. (12)&(51)]. These relations can be used to simplify the R.H.S of (A1.5), and, substituted back into (A1.5). The result of this is the Taylor series approximation to $F_h(\xi, y_s, y_r)$, which reads,

$$F_h(\xi, y_s, y_r) \simeq V_0(\xi) - \frac{j}{4\xi}(y_s^2+y_r^2)V_1(\xi). \qquad (A1.6)$$

The residue series form for the zeroth order hard surface Fock function reads:

$$V_0(\xi) = e^{-j\frac{\pi}{4}}\sqrt{\pi\xi}\sum_{n=1}^{\infty}\frac{e^{-j\xi\tau_n}}{\tau_n} \qquad (A1.7)$$

The first order hard surface Fock function can be similarly expressed as:

$$V_1(\xi) = e^{j\frac{\pi}{4}}2\sqrt{\pi}\xi^{\frac{3}{2}}\sum_{n=1}^{\infty}e^{-j\xi\tau_n} \qquad (A1.8)$$

In (A1.7,1.8) the Fock parameter ξ is given by (3.6). The residue series is applicable whenever $\xi \geq 0.6$. The general forms for $V_0(\xi)$ and $V_1(\xi)$ are available in the reports and papers of Logan [14], Pathak and Wang [3] or Lee [17]. τ_n is 'nth' root of the Airy function in (A1.7,8)

The $y_{s,r}$ are dependent on the source and receiver heights $h_{s,r}$. They have been defined in (3.12), Chapter 3 of this thesis.

A.2 Approximation to the generalized hard Fock integral when both antennas are at large heights off the cylinder.

In this Appendix, the generalized hard Fock integral is approximated for large values of source/ observer distances from the cylinders curved surface. It is shown that this approximation yields the well-known Fresnel integral and the hard Pekeris caret function. It is also important to note that the final result, as obtained here, can be found in vol. 1 of Logan's report [14, p. 7-4]. Logan apparently seems to have presented the various forms of this important special case from the various publications of the Soviet researchers in the mid-1940's. This derivation clearly points out the major limitations of the UTD curved surface scattering formulations as is present in the NECBSC2 code. To follow the derivations, we have referred to some special (advanced) references that are useful only for this Appendix. As indicated later in the appendix, there is a minor difference in the final expressions obtained here and the one by Pathak. However, this difference does not detract us from analysing the limitations in the UTD scattering formulations. (This difference could have been due to several reasons. We have examined only the special form of the hard Fock integral, whereas Pathak's derivation is entirely different. However, at the present time, the analysis presented here is sufficient for our purposes.)

In this development, we confine ourselves to the form of the hard Fock integral only. The conversion of the scattered field by an axial magnetic current element to

the present form of the Fock integral is not discussed here. This derivation can be found in the textbooks on advanced electromagnetic theory and scattering. Without presenting the analytical details, we summarize the steps involved in obtaining the hard Fock integral.

The form of the generalized hard Fock integral is:

$$F_h(\xi, y_s, y_r) = \frac{e^{-j\frac{\pi}{4}}\xi^{\frac{1}{2}}}{2\pi^{\frac{1}{2}}} \int_{-\infty}^{+\infty} e^{-j\tau\xi} d\tau W_2(\tau - y_s) \left[W_1(\tau - y_r) - \frac{W_1'(\tau)}{W_2'(\tau)} W_2(\tau - y_r) \right]. \tag{A2.1}$$

Our approximation refers to the situation $y_{s,r} \rightarrow \infty$. From Bowman, *et. al.* [2A, p. 62, Eqns. (I.265)], we have the following form for the Fock type Airy function,

$$W_{1,2}(z) = 2\sqrt{\pi} e^{\mp\frac{5\pi j}{6}} Ai(z e^{\pm\frac{2\pi j}{3}}). \tag{A2.2}$$

The Miller type Airy functions can be represented in the contour integral form from Bleistien and Handelsman's book [2A, p. 52, Eqns. (2.5.10)] as:

$$Ai(s) = \frac{1}{2\pi j} \int_{\Gamma} e^{st - \frac{t^3}{3}} dt. \tag{A2.3}$$

The contour Γ starts from $\infty e^{\frac{-2\pi j}{3}}$ and ends at $\infty e^{\frac{+2\pi j}{3}}$. Here $s = \rho e^{j\theta}$. The asymptotic form of Airy function for complex argument can be found in volume 1 of Logan's report [14, p. 8-8, Eqn. (8.10)] or from Bleistien and Handelsman [2A, p. 285, Eqn. (7.3.16)], that reads,

$$Ai(\rho e^{j\theta}) \rightarrow \frac{e^{\frac{-j\theta}{4}}}{2\sqrt{\pi}\rho^{\frac{1}{4}}} exp\left[-\frac{2}{3}\rho^{\frac{3}{2}} e^{\frac{j3\theta}{2}} \right]. \tag{A2.4}$$

Eqn.(A2.4) is valid only when $\rho \rightarrow \infty$, and, $|arg(\theta)| < \pi$.

The steepest descent method in obtaining (A2.4) has been discussed in detail in Bleistien and Handelsman's book, and, hence is not repeated here. The Fock

type Airy functions can now be expanded via Eqns. (A2.2) and (A2.4) for $|z| \rightarrow \infty$. These forms are then subsequently substituted in (A2.1). After some lengthy algebraic manipulations, the following simplified form for the integrand in (A2.1) is obtained:

$$\Psi_h(\xi, y_s, y_r) \simeq -2j\frac{1}{(y_s y_r)^{\frac{1}{4}}} exp(-\frac{2j}{3}[(y_s-\tau)^{\frac{3}{2}} + (y_r-\tau)^{\frac{3}{2}}])\left[1 + \frac{jV'(\tau)}{W_2'(\tau)}\right]. \quad (A2.5)$$

In (A2.5), $2jV(\tau) = W_1(\tau) - W_2(\tau)$. One substitutes the form for Ψ_h from (A2.6) into (A2.1). The compact form for (A2.1) reads:

$$F_h(\xi, y_s, y_r) \simeq \frac{e^{-j\frac{\pi}{4}}\xi^{\frac{1}{2}}}{2\pi^{\frac{1}{2}}} \int_{-\infty}^{+\infty} e^{-j\tau\xi} d\tau \Psi_h(\xi, y_s, y_r). \quad (A2.6)$$

In (A2.6), $\Psi_h(\xi, y_s, y_r)$ is given as in (A2.5). Next we expand the exponential term in (A2.6) in two different forms. This turns out to be necessary because it is important to evaluate the integral numerically and thus justified approximations are admissable. These approximations are within the framework, $y_{s,r} \rightarrow \infty$. Retaining only three terms, we have,

$$(y_s-\tau)^{\frac{3}{2}} + (y_r-\tau)^{\frac{3}{2}} \simeq (y_s^{\frac{3}{2}} + y_r^{\frac{3}{2}}) + \frac{3}{2}\left[-\tau(y_s^{\frac{1}{2}} + y_r^{\frac{1}{2}}) + \frac{\tau^2}{4}(y_s^{-\frac{1}{2}} + y_r^{-\frac{1}{2}})\right]. \quad (A2.7)$$

This form is substituted in (A2.6) only for the *first* term in Eqn.(A2.5) - designated within $\left[...\right]$. For the second term, one uses the two term approximation (terms including τ only) in (A2.7). (This is necessary because it will be found that higher order approximations in (A2.7) result in a complicated integral involving $V'(\tau)$ and $W_2'(\tau)$, that cannot be evaluated by approximate methods.) However, the first term in the integral can readily be evaluted. This evaluation will be shown a bit later in

this Appendix. Before that, the reduced form for $F_h(\xi, y_s, y_r)$ reads:

$$F_h(\xi, y_s, y_r) \simeq \frac{\xi^2}{(y_s y_r)^{\frac{1}{4}}} \frac{e^{-j\frac{\pi}{4}}}{2\sqrt{\pi}} exp[\frac{-2j}{3}(y_s^{\frac{3}{2}} + y_r^{\frac{3}{2}})] \left[-2j \int_{-\infty}^{+\infty} e^{-j\beta(\tau^2 + \frac{4}{3}\tau)} d\tau + 2 \int_{-\infty}^{+\infty} e^{-j\mu\tau} \frac{V'(\tau)}{W_2'(\tau)} d\tau \right] \tag{A2.8}$$

One can further substitute for the hard Pekeris caret function in Eqn. (A2.8) as:

$$\hat{P}_h(\mu) = \frac{e^{\frac{-j\pi}{4}}}{\sqrt{\pi}} \int_{-\infty}^{+\infty} e^{-j\mu\tau} \frac{V'(\tau)}{W_2'(\tau)} d\tau. \tag{A2.9}$$

In Eqns. (A2.8,2.9) the substitutions $\mu = \xi - (\sqrt{y_s} + \sqrt{y_r})$, and,

$$\beta = \frac{\sqrt{y_s} + \sqrt{y_r}}{\sqrt{y_s}\sqrt{y_r}}$$

have been used. Eqn. (A2.8) is <u>not</u> of the same form containing the 'wedge transition function', introduced by Pathak in [8, Eqn. (16c)]. To obtain Pathak's form, one needs to obtain a more general form for (A2.5) than the one presented here. This proceedure is quite complicated, and, has been presented by Fock in [12, Ch. 7, pp. 138-140]. Fock shows that by retaining the form for $\Psi_h(\xi, y_s, y_r)$ in the '*pole close to a saddle point*' case, the standard form for the Fresnel integral

$$\int_{-\infty}^{+\infty} \frac{e^{-\mu\tau^2}}{\tau^2 + jb^2} d\tau = 2\sqrt{\pi} F(b\sqrt{\mu})$$

can be obtained. (The details can be found in Clemmow's book [3A, Sec. 3.3.1, pp. 51-53].) This results in the <u>large argument</u> form for $F_h(\xi, y_s, y_r)$ that reads:

$$F_h(\xi, y_s, y_r) \simeq \frac{\xi^2}{(y_s y_r)^{\frac{1}{4}}} exp[-\frac{2j}{3}(y_s^{\frac{3}{2}} + y_r^{\frac{3}{2}})] \left[e^{-j\frac{\pi}{4}} \frac{(1 - F(X))}{2\mu\sqrt{\pi}} + \hat{P}_h(\mu) \right]. \tag{A2.10}$$

The present derivation shows that for large distances, $y_{s,r} \rightarrow \infty$, Pathak's original formulation for scattering of waves by a cylinder can be recovered. The difference

arises in the U, V and p, q formulation for creeping waves in the appearences of the $\hat{P}_h(x)$ and $V_0(x)$ functions in describing the creeping wave attenuation over the geodesic paths.

Eqn. (A2.10) also shows that as $y_{s,r} \rightarrow 0$, the relation breaks down near the curved surface of the cylinder, as, it becomes infinite. This is the basic reason why the NECBSC2 code predicted '*infinite*' coupling near the curved surface of the cylinder in Fig. 5.5, Chapter 5.

In summary, by carefully analysing the mathematical details of the two different approximations to the hard Fock integral, the mutually exclusive nature of the U, V and p, q formulations can be understood now. The analytical forms in Appendices A.1 and A.2 point out that one form cannot be a substitute for the other. Thus, the mutual exclusivity arises in terms of the distances involved in the two approximations.

References for Appendix A.3

[1A] N.Bleistien and R.Handelsman,'*Asymptotic Expansions of Integrals*', Dover Publications Inc., New York, 1986.

[2A] J.J.Bowman, T.B.A Senior, and, P.L.E Uslenghi (eds.),'*Electromagnetic and Acoustic Scattering by simple shapes*', North-Holland, Amsterdam, 1969.

[3A] P.C.Clemmow,'*The Plane Wave Spectrum Representation of Electromagnetic Fields*', Pergamon Press, New York, 1966.

A.3 Typical AAPG code outputs for off-surface Coupling Gain calculations.

In this Appendix, the AAPG code outputs are shown. These results were being obtained by actually running the version 07 of the AAPG code at the EMC Lab of Concordia University. This was done in order to obtain validation of the computer program written, based on Eqns. (5.1 to 5.7) for easy generation of data. The computer program can calculate for arbiratry antenna locations on or off the cylinder surface.

The data shown in Figs. A.1 to A.5 refer to a cylinder of radius $a = 24''$, f= 8 GHz, $Z_{offset} = 0''$ and $\phi = 180^0$. The antennas were moved by equal amounts off the cylinder for both source and receiver. Thus:

$$C_{AAPG} = TFS + SF + G_t + G_r. \tag{A3.1}$$

In (A5.1), TFS and SF are the transmission and surface shading loss that can bee seen in the AAPG outputs in Figs. A.1 to A.5. The final result is then shown in Fig. 5.5 of the thesis. The user may note that the AAPG coupling paths are shown by dashed lines in these figures.

The version 07 refers to the technical report by Widmer [6].

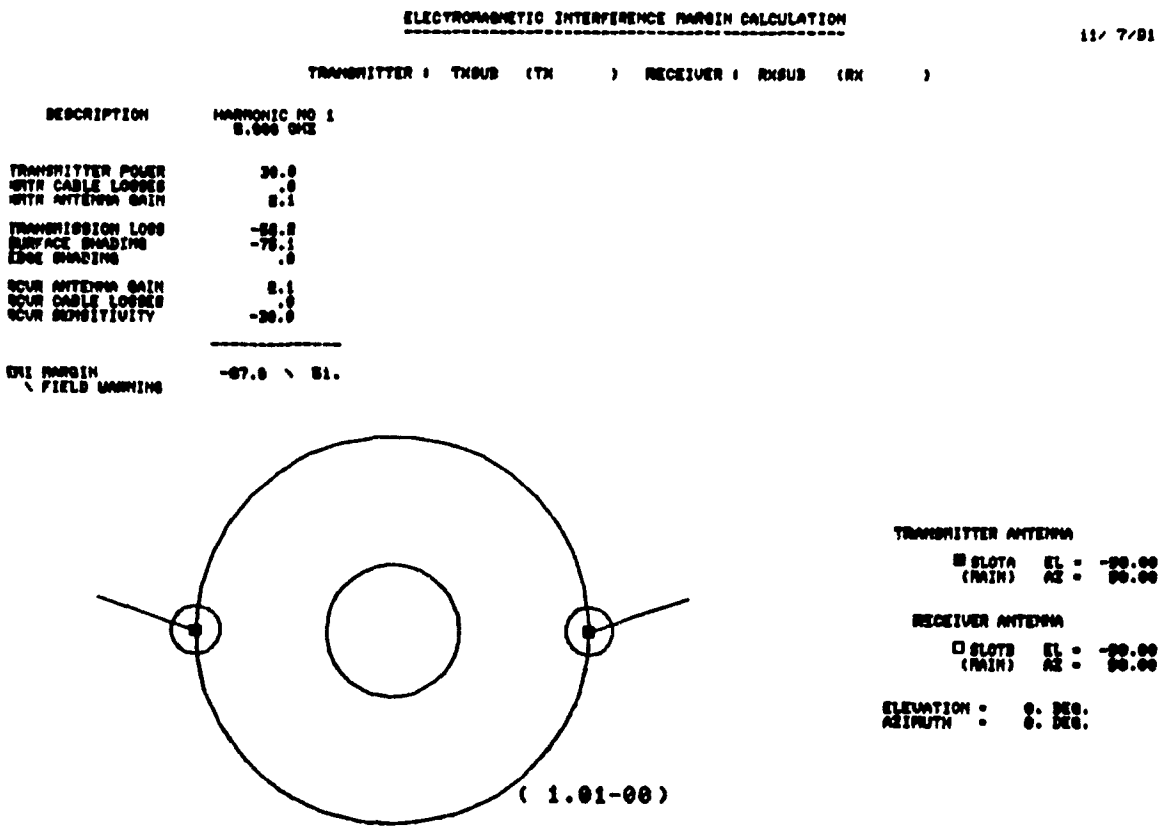

Fig. A.1. AAPG output for antennas at $h = 0\lambda$. The surface shading and the transmission loss are shown here. To these values an antenna gain of 2.15 dB was added for the transmitter and receiver, to obtain the total coupling gain that is plotted in Fig. 5.4. The situation here is a special case of Fig. 3.1 with $h_s = h_r = 0$ therein.

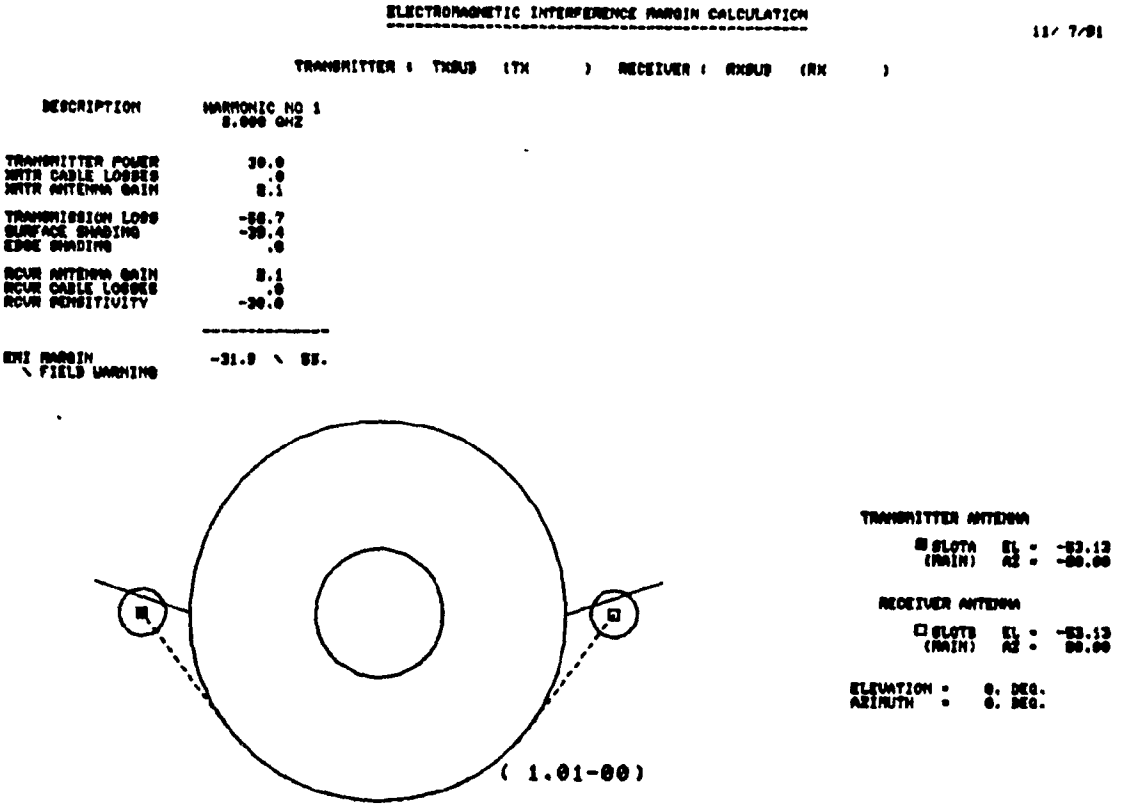

Fig. A.2. AAPG output for antennas at $h = 4\lambda$. The surface shading and the transmission loss are shown here. To these values an antenna gain of 2.15 dB was added for the transmitter and receiver, to obtain the total coupling gain that is plotted in Fig. 5.4. The total distance between the antennas in this situation is shown by the dotted line in the AAPG output display. The free-space wave spreading loss is computed over this length; the shading loss is computed over the intercepted portion of the geodesic. The situation is similar to Fig. 3.1 of the report.

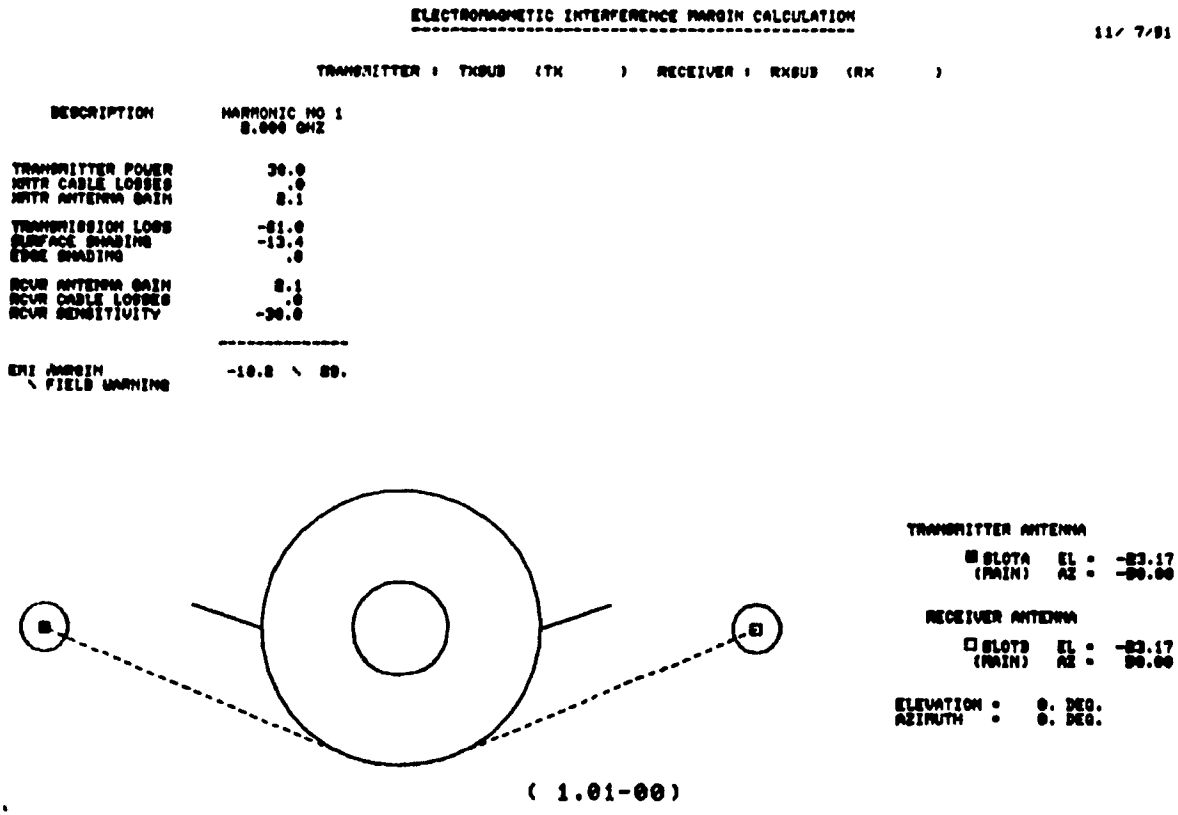

Fig. A.3. AAPG output for antennas at $h = 25\lambda$. The surface shading and the transmission loss are shown here. To these values an antenna gain of 2.15 dB was added fo the transmitter and receiver, to obtain the total coupling gain that is plotted in Fig. 5.4. The total distance between the antennas in this situation is shown by the dotted line in the AAPG output display. The free-space wave spreading loss is computed over this length; the shading loss is computed over the intercepted portion of the geodesic. The situation is similar to Fig. 3.1 of the report.

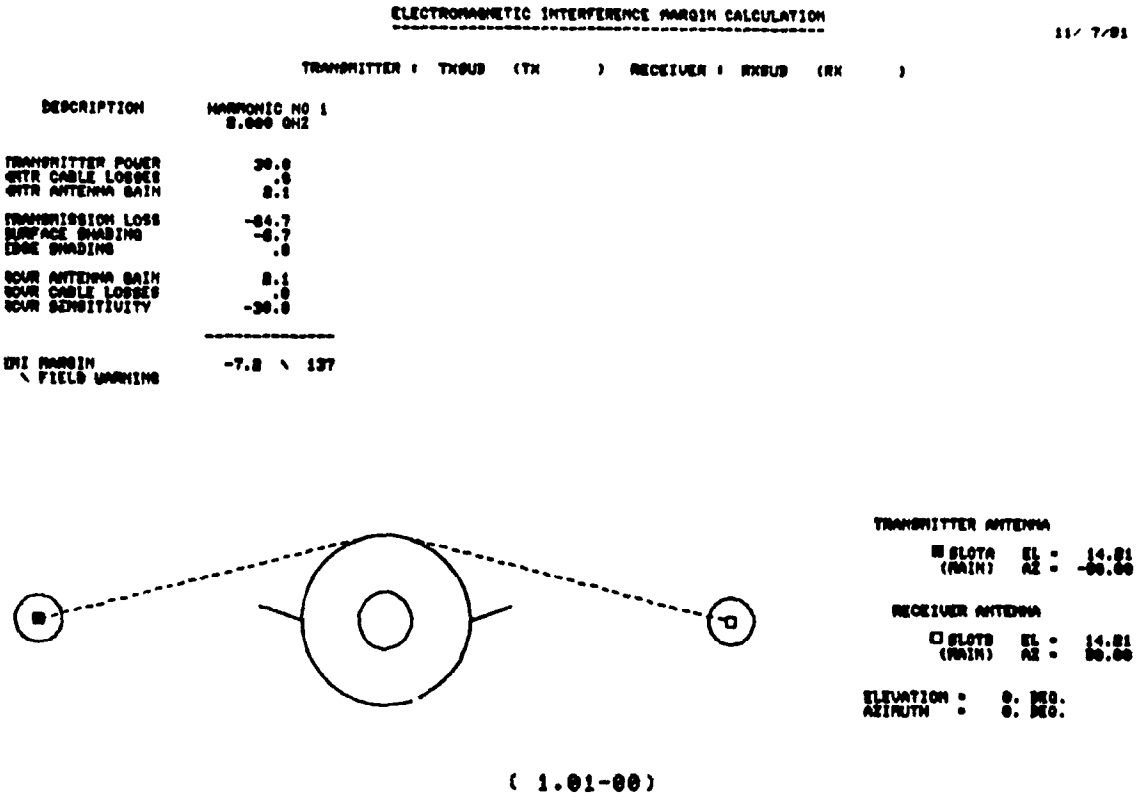

Fig. A.4. AAPG output for antennas at $h = 50\lambda$. The surface shading and the transmission loss are shown here. To these values an antenna gain of 2.15 dB was added for the transmitter and receiver, to obtain the total coupling gain that is plotted in Fig. 5.4. The total distance between the antennas in this situation is shown by the dotted line in the AAPG output display. The free-space wave spreading loss is computed over this length; the shading loss is computed over the intercepted portion of the geodesic. The situation is similar to Fig. 3.1 of the report.

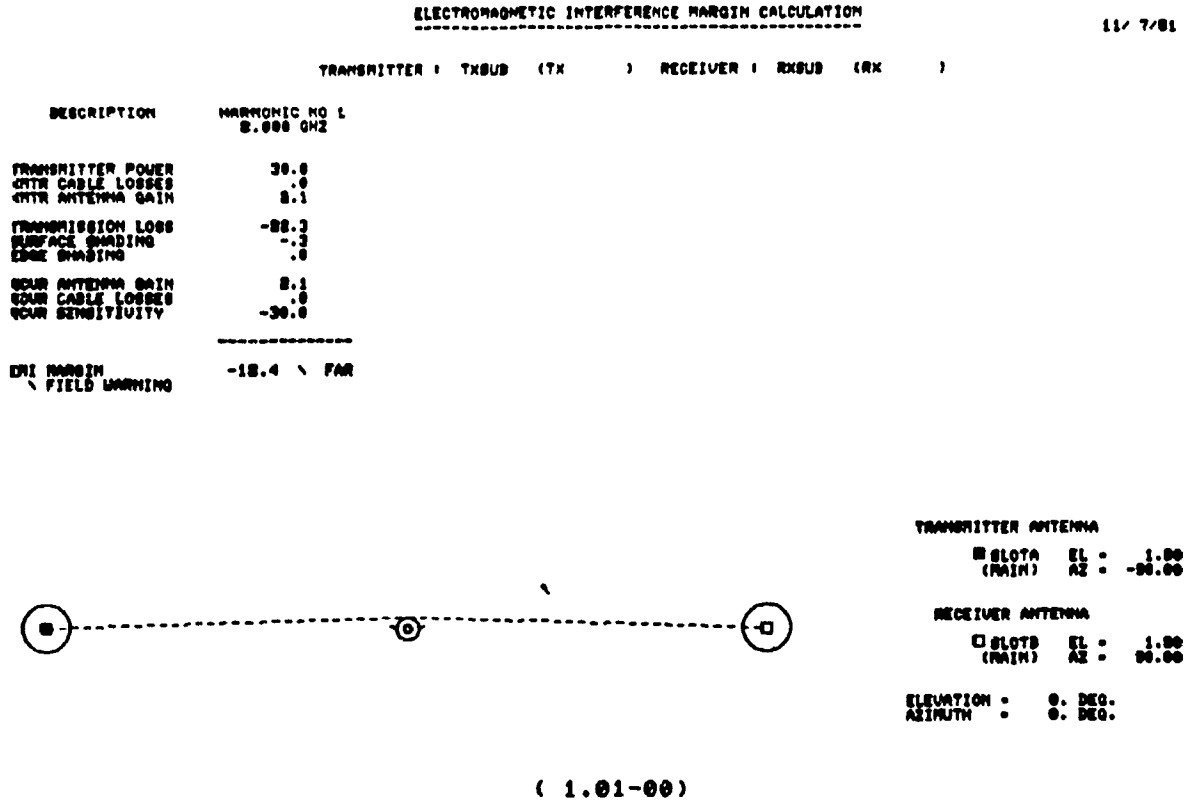

Fig. A.5. AAPG output for antennas at $h = 500\lambda$. The surface shading and the transmission loss are shown here. To these values an antenna gain of 2.15 dB was added for the transmitter and receiver, to obtain the total coupling gain that is plotted in Fig. 5.4. The total distance between the antennas in this situation is shown by the dotted line in the AAPG output display. The free-space wave spreading loss is computed over this length; the shading loss is computed over the intercepted portion of the geodesic. The situation is similar to Fig. 3.1 of the report.